INSTITUTE OF SPACE AND ASTRONAUTICAL SCIENCE
YOSHINODAI, CHUO, SAGAMIHARA, KANAGAWA 252-5210

ISAS RESEARCH NOTE

ISAS RN 877

Study of the time and spatial variabilities of the soft X-ray diffuse background

Hiroshi Yoshitake

February 2013

Institute of Space and Astronautical Science,
Japan Aerospace Exploration Agency

Study of the time and spatial variabilities of the soft X-ray diffuse background

Hiroshi Yoshitake

Reproduced from the thesis submitted to
the Department of Physics,
Graduate School of Science, University of Tokyo
December, 2011

Study of the time and spatial variabilities of the soft X-ray diffuse background

Hiroshi Yoshitake

Department of Physics, University of Tokyo.

Institute of Space and Astronautical Science,
Japan Aerospace Exploration Agency.

(ISAS/JAXA)

December, 2011

Abstract

The soft X-ray diffuse background (SXDB) under 1 keV is significantly influenced by the emission lines from highly ionized heavy elements in the hot interstellar medium with temperature of $\sim 10^6$ K. However, origins of the highly ionized medium have been found to be complicated since the first discovery of the solar-wind charge exchange (SWCX) induced emission. SWCX with the interstellar neutrals in the heliosphere (H-SWCX) is considered to induce X-ray emission in any direction, which shows both time and spatial variabilities. It is difficult to identify the X-ray emission from H-SWCX itself. In this thesis, we have investigated the time and spatial variabilities of SXDB, especially focusing on the OVII (0.57 keV) emission. Suzaku achieves high sensitivity for spatially extended emission under 1 keV and OVII emissions are clearly detected. In the data reduction, we carefully removed the contributions of the SWCX induced X-ray emission from the Earth's geocorona (G-SWCX).

First, we identified the time variability of H-SWCX induced emission. The 11-yr Solar Cycle passed its minimum phase at early 2009. Long-term time variabilities of OVII emission toward same field of view are studied by annual observations toward Lockman Hole from 2006 to 2011. Intensities of OVII emissions from 2006 to 2009 are 2.55 ± 0.74 (2006), 3.68 ± 0.72 (2007), 3.03 ± 0.77 (2008), 2.69 ± 0.80 (2009) LU (Line Unit = photons $s^{-1}cm^{-2}sr^{-1}$), which are consistent within 90% statistical errors. However, OVII emission in 2010 and 2011 are 6.06 ± 1.07 and 5.28 ± 1.60 LU, respectively. They are 2–3 LU larger than the values from earlier observations. Statistical significances of the OVII intensity variation of 2010 and 2011 with respect to an average of 2006 to 2009 ($= 2.99 \pm 0.38$ LU) are 4.5σ (2010) and 2.3σ (2011), respectively. We suggest that this OVII variation relates to the geometrical change of slow and fast solar wind structures associated with the 11-year solar activity.

Second, we investigate multiple observations of two blank sky fields towards the dense molecular cloud MBM 16, and vicinity of the Seyfert galaxy NGC 2992, in order to evaluate enhancement of the SWCX induced X-ray emission by the Helium Focusing Cone (HeFC). The intensity of OVII emission was estimated to be 3.9 ± 1.3 (MBM 16) and 4.6 ± 0.7 (NGC 2992) LU when the line of sight is through the HeFC, while it was < 1.9 (MBM 16, 90 % upper limit) and 3.2 ± 0.6 (NGC 2992) LU off the HeFC, respectively. The chance probability of obtaining the observed intensity differences by the Poisson statistics is less than 0.3 % for both directions. Therefore H-SWCX induced emission at HeFC is suggested by these intensity variations. We also compare the observed OVII emission with simulated H-SWCX induced one. The observed intensity differences are better reproduced by the simulation under the solar minimum condition than the maximum one in both MBM 16 and NGC 2992. 90 % upper limit of the offset OVII intensity to reproduce observed OVII emission by the model is 0.1 (1.3) LU for solar minimum (maximum) simulation toward MBM 16. Due to the strong interstellar absorption at

MBM 16, this offset intensity express the upper limit contribution from Local Bubble. Whichever the simulation was applied with solar minimum or maximum situations, simulated OVII emission requires $\sim$ 2 LU offset intensity for the NGC 2992 field. This 2 LU offset OVII emission is consistent with the model parameters of the spectral model component interpreted to be from the halo of our Galaxy.

Third, we examine the spatial variability of OVII emission using 57 Suzaku observations. The observed OVII emission anti-correlated with absolute Galactic latitude in north hemisphere. In contrast, there are no ecliptic latitude dependence that is expected if the H-SWCX has large contribution to the spatial variation. These results suggest a presence of emission absorbed with Galactic neutrals. We compare the intensities between observed total and simulated H-SWCX induced OVII emissions. Observed intensity is larger than the simulated one in most directions. We also compare the OVII emission after subtraction of H-SWCX model prediction with the simple constant emission model absorbed with Galactic neutrals. More than 70 % of 57 observations, H-SWCX model subtracted OVII emission are included in the systematic uncertainties of the model. The observed directions having bright OVII emission to this simple model are localized near the LMC and north high latitude area extending $\ell = 90^\circ$ to 180° and $b = 30^\circ$ to 90°. In contrast, faint points are mainly found southern high latitude area of $\ell = 150^\circ - 180^\circ$ and $b = -50^\circ$ to -70°.

Acknowledgments

Many people supported me during these five years.

Foremost, I sincerely thank to my supervisor Prof. K. Mitsuda. This thesis would not have been possible unless he gave enormous supports and insightful comments to my study. He also led me in various situations during my graduate school period with a deep scientific view and taught me the logical thinking of various issues.

I would like to thank to Prof. N. Y. Yamasaki for her scientific advice and encouragements. Her advices are always precise and are found to be very instructive to me. I also express my thanks to Dr. Y. Takei who have hot discussions on scientific issues, instrumental experiments (, and other things) with me. I have a lot of respect for his quick mind and diligence.

I am grateful to Dr. D. Koutroumpa for showing us the details of her H-SWCX induced X-ray emission model and the valuable discussion.

I also wish to thank A. Yokoyama and S. Ito who are secretaries of our laboratory. Their supports to my school life and encouragements made me happy. I thank to my colleagues and friends at ISAS : Dr. Y. Ezoe, Dr. K. Shinozaki, H. Kawahara, T. Yoshino, S. Kimura, T. Hagihara, M. Koshiishi, H. Aono, I. Mitusishi, K. Morihana, K. Someya, W. Hirakoso, N. Sekiya, K. Sakai, K. Nagayoshi, and R. Yamamoto. A little discussion and a lot of trivial talks with them are precious memory for my life.

Finally I appreciate my parents for their great help and encouragement over a number of years.

Hiroshi Yoshitake.

Contents

List of Tables

List of Figures

Abbreviation

$(\lambda,\ \beta)$	Ecliptic coordinates
$(\alpha,\ \delta)$	Equatorial coordinates
$(\ell,\ b)$	Galactic coordinates
ACE	Advanced Composition Explorer
APEC	Astrophysical Plasma Emission Code
ARF	Auxiliary Response File
AU	Astronomical Unit $= 1.496 \times 10^{13}$ cm
BI	Back Illuminated (CCD)
CALDB	Calibration DataBase
CIE	Collisional Ionization Equilibrium
CIR	Corotating Interaction Region
CXB	Cosmic X-ray Background
FI	Front Illuminated (CCD)
FOV	Field of View
G-SWCX	Geocoronal Solar-Wind Charge Exchange
HeFC	Helium Focusing Cone
H-SWCX	Heliospheric Solar-Wind Charge Exchange
LAB	Leiden/Argentine/Bonn (Galactic HI Survey)
LB	Local Bubble
LIC	Local Interstellar Cloud
LOS	Line of Sight
LU	Line Unit $\equiv$ photons $\mathrm{s}^{-1}\,\mathrm{cm}^{-2}\,\mathrm{sr}^{-1}$
$M_\odot$	Solar Mass $= 1.988 \times 10^{33}$ g
NXB	Non X-ray Background
RASS	ROSAT All Sky Survey
RMF	Redistribution Matrix File
SCI	Spaced-row Charge Injection
SNR	Super Nova Remnant
SWICS	Solar Wind Ion Composition Spectrometer
SWCX	Solar-Wind Charge Exchange
SWIMS	Solar Wind Ion Mass Spectrometer
SXDB	Soft X-ray Diffuse Background
XIS	X-ray Imaging Spectrometer
XRT	X-Ray Telescope

1 Introduction

Diffuse X-ray emission over the sky under 1 keV was discovered from the early rocket observations in 1970s and its origin of it has been debated even now. For the origin of line emission of soft X-ray diffuse background (SXDB) in ROSAT *R45* band (0.44–1.21 keV), the situation became more complicated since the first discovery of solar-wind charge exchange (SWCX) in late 1990s. SWCX induced emission has bright OVII emission in R45 band that is the same spectral feature as thin thermal plasma emission with temperature of $kT \sim 0.1$ keV. Therefore, it is hard to distinguish whether the dominant line emission component is SWCX or thermal plasma (or both of them). However, since SWCX induced emission shows time and spatial variabilities, to study the variability is expected to give us clues to reveal the evidence of SWCX induced X-ray emission.

In this thesis, we investigate the time and spatial variabilities of SXDB especially focusing on the OVII (0.57 keV) emission with Suzaku satellite. XIS1, the X-ray CCD camera onboard Suzaku, achieves high sensitivity under 1 keV and OVII (0.57 keV) emission is clearly detected. Before starting analysis, we give a short review of SXDB in Chapter 2 at first. The brief description of Suzaku and solar wind monitoring satellites are summazived in Chapter 3. We explain the common methods of data reduction and spectral analysis in later 3 chapters in Chapter 4. In Chapter 5 and Chapter 6, we investigate the the time and spatial variabilities of H-SWCX induced OVII emission, respectively. In Chapter 7, we examine the spatial variability of OVII emission over the sky. We finally conclude new findings about SXDB revealed though the studies in this thesis in Chapter 8.

All error ranges quoted in text are for 90% confidence level, while vertical bars in figures show 1σ errors, unless otherwise noted. Throughout we use Anders & Grevesse (1989) abundances.

2 Review

2.1 Interstellar Medium

We started a review of this thesis from the general properties of interstellar medium (ISM). Our Galaxy, namely the Milky Way system, is not only made of stars. It also contains significant amounts of tenuous matter in gaseous states that spread out inhomogeneouslly throughout interstellar space. This gaseous ISM exists in the various forms (atoms, molecules, dusts, ions, and electrons) and accounts for $10-15$ % of the total mass of the Galactic disk.

Table 2.1 is a summary of physical parameters of the different components of the interstellar gas. All values were rescaled to $R_\odot = 8.5$ kpc. About half the interstellar mass is confined to discrete clouds, while they occupy only $\sim 1-2$ % of the interstellar volume. These interstellar clouds are also divided into three types: the dark clouds made of very cold molecular gas ($T \sim 10-20$ K), the diffuse clouds consisting of cold atomic gas ($T \sim 100$ K), and the intermediate clouds between them containing molecular and atomic gases. The rest of the interstellar matter, spread out between the clouds, exists in three different forms : warm (mostly neutral) atomic, warm ionized, and hot ionized gases, where warm refers to a temperature of $\sim 10^4$ K and hot to a temperature of $\sim 10^6$ K. The density of ISM in the vicinity of Sun varies from $\sim 1.5 \times 10^{-26}$ g cm^{-3} in the hot gas to $\sim 2.0 \times 10^{-20} - 2.0 \times 10^{-18}$ g cm^{-3} in the densest molecular cloud, with an average of $\sim 2.7 \times 10^{-24}$ g cm^{-3}. Both $\Sigma_\odot$ and $\mathcal{M}^\dagger$ in Table 2.1 include 90.8 % by number (70.4 % by mass) of hydrogen, 9.1 % (28.1 %) of helium, and 0.12 % (1.5 %) of heavier element.

Table 2.1 Physical properties of ISM in different phases from Ferriére (2001).

Component	Temperature T (K)	Density n (cm^{-3})	Mass density* $\Sigma_\odot$ ($M_\odot$ pc^{-2})	Total mass† $\mathcal{M}$ (10^9 $M_\odot$)	Filling factor ξ
Molecular	$10-20$	10^2-10^6	~ 2.5	$\sim 1.3-2.5$	$\sim 10^{-4}$
Cold atomic	$50-100$	$20-50$	~ 3.5	≥ 6.0	0.013
Warm atomic	$6000-10000$	$0.2-0.5$	~ 3.5		0.368
Warm ionized	~ 8000	$0.2-0.5$	~ 1.4	≥ 1.6	0.083
Hot ionized	$\sim 10^6$	~ 0.0065	–	–	~ 0.46

* Azimuthally averaged mass density per unit area at the solar circle.

† Total mass contained in the entire Milky Way.

The well-known vertical distributions of the mean densities (H nuclei per cm^{-3}) to the galactic

plane are given by following equations (Cox 2005) :

$$\text{Molecular} \ : \ n_m(z) = 0.58 \exp\left[-\left(\frac{z}{81\ \text{pc}}\right)^2\right] \quad \text{cm}^{-3} \tag{2.1}$$

$$\text{Cold atomic} \ : \ n_n(z) = 0.57 \times 0.7 \exp\left[-\left(\frac{z}{121\ \text{pc}}\right)^2\right] \quad \text{cm}^{-3} \tag{2.2}$$

$$\text{Warm atomic} \ : \ n_n(z) = 0.57 \left\{0.19 \exp\left[-\left(\frac{z}{318\ \text{pc}}\right)^2\right] + 0.11 \exp\left[-\left(\frac{|z|}{401\ \text{pc}}\right)\right]\right\} \quad \text{cm}^{-3} \tag{2.3}$$

$$\text{Warm ionized} \ : \ n_i(z) = 0.015 \exp\left[-\left(\frac{|z|}{70\ \text{pc}}\right)\right] \quad \text{cm}^{-3} \tag{2.4}$$

$$\text{Hot ionized} \ : \ n_i(z) = 0.025 \exp\left[-\left(\frac{|z|}{1000\ \text{pc}}\right)\right] \quad \text{cm}^{-3} \ . \tag{2.5}$$

Figure 2.1 shows the each and total density distributions from the above components. Due to the long scale height of the distribution function, interstellar space above $|z| > 0.5$ kpc is mostly filled with warm atomic and hot ionized ISMs.

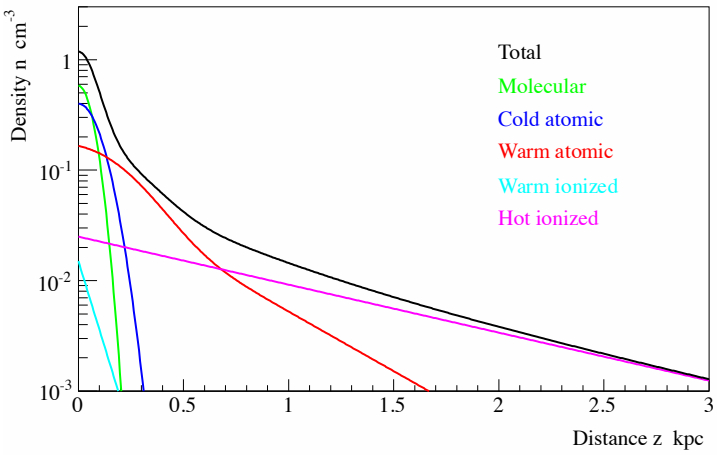

Figure 2.1 The distribution of interstellar hydrogen density above the Galactic Plane. Distributions are calculated from Equation (2.1) to (2.5).

The vertical gravity to the galactic plane at the Solar circle was resolved to its components. A simple exponential model is

$$|g|(z) = \left\{4.2\left[1 - \exp\left(-\frac{|z|}{165\ \text{pc}}\right)\right] + \frac{4.1|z|}{2\ \text{kpc}}\right\} \cdot \frac{1 - \dfrac{|z|}{27\ \text{kpc}}}{\sqrt{1 + \left(\dfrac{z}{6\ \text{kpc}}\right)^2}} \cdot 10^{-9}\ \text{cm s}^{-2} \ . \tag{2.6}$$

The first term in the curly bracket represents the contributions of the total ISM and disk stars, the second one is due to halo material, and the factor of previous two terms represents a correction factor for the gravity model in Dehnen & Binney (1998). Given the vertical density and gravity distributions, it is possible to calculate vertical distribution of total pressure p_{tot} above the Galactic plane under assumption of hydrostatic equilibrium $dp(z)/dz = n(z)g(z)$. The mid-plane value of

total pressure is estimated $p_{\rm tot}/k \sim 22000$ cm^{-3}K. However, the thermal pressure of the total ISM except high-temperature component in mid-plane is

$$p_{\rm th}/k = \sum_{\rm ISM\ phase} \xi nT \sim 2500 \text{ cm}^{-3}\text{K} \ . \tag{2.7}$$

Therefore thermal pressure is only 10 % of the total one. It is now considered that the magnetic fields $B \sim 5$ μG, cosmic ray (energy density $E_{\rm cr} \sim 2$ eV cm^{-3}), and dynamical (with a vertical velocity dispersion of $\sigma \sim 6$ km s^{-1}) pressures are each taken as one third of the total non-thermal pressure, $p/k \sim 7300$ cm^{-3}K (Cox 2005).

2.2 Overview of the Soft X-ray Diffuse Background

Next we review the recent studies of Soft X-ray Diffuse Background (SXDB). In this thesis we use the word, the "SXDB", to mean the emission below 1 keV that is spatially unresolved to individual sources. Above 2 keV, unresolved X-ray emission is called the cosmic X-ray background (CXB). We now believe that the most of the CXB comes from numerous faint extragalactic sources; active galactic nuclei (AGNs). With the deep observations of the Chandra and XMM-Newton observatories, about 80 % of the CXB has been actually resolved into point sources.

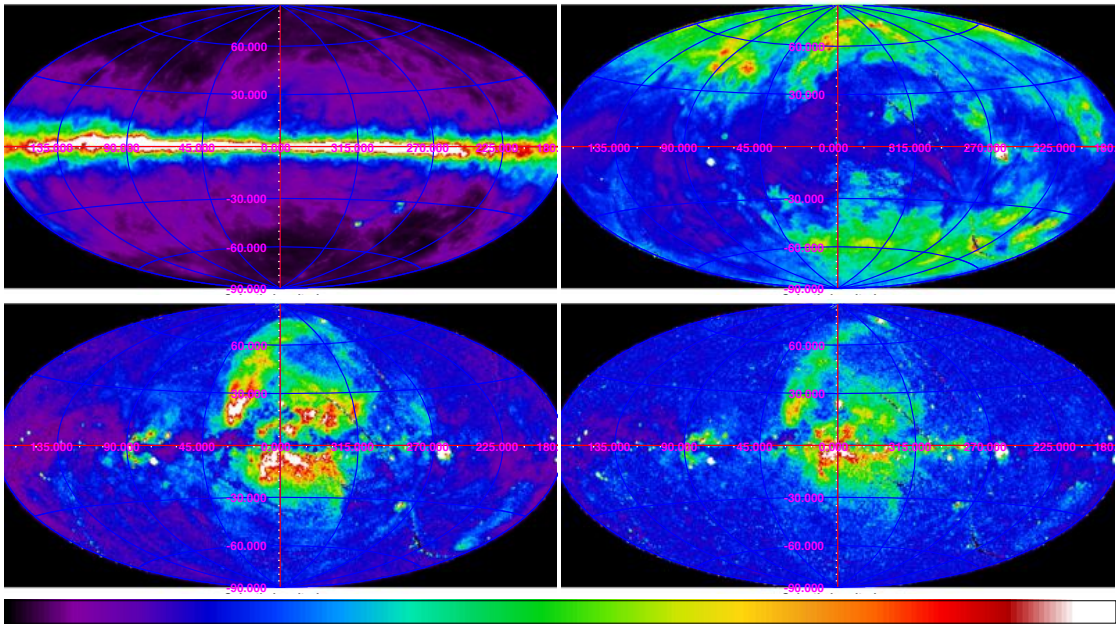

Figure 2.2 All sky maps of neutral hydrogen column density and soft X-ray diffuse emission in Galactic coordinate (Hammer-Aitoff). Upper Left : column density of the neutral hydrogen in our Galaxy derived from HI λ 21 cm line with LAB survey, Upper Right : ROSAT R12 (1/4 keV) band, Lower Right : ROSAT R45 (3/4 keV) band, and Lower Right : ROSAT R67 (5/4 keV) band.

The latest all sky maps of the SXDB was made by ROSAT satellite carried out in from 1990 to 1991 (Snowden et al. 1993a). Figure 2.2 shows all sky maps of neutral hydrogen column density with LAB survey (Kalberla et al. 2005) and SXDB emission with ROSAT in Galactic coordinate.

ROSAT all sky survey (RASS) gave the three images in R12 (1/4 keV), R45 (3/4 keV), R67 (5/4 keV) bands, whose energy ranges are $0.12-0.284$ keV, $0.47-1.21$ keV, and $0.76-2.04$, respectively, from an X-ray focusing mirror and the position sensitive proportional counter (PSPC) observations. The emission in R12 band is clearly anti-correlated with Galactic neutral hydrogen column density of the direction. The hydrogen column density varies from $\sim 1.0 \times 10^{22}$ cm^{-2} at mid-plane to $\sim 4.0 \times 10^{20}$ cm^{-2} at high latitude of $|b| >\sim 30°$. Given the values, about 90 % of X-rays outside of Galactic plane will be photoelectrically absorbed by cold ISM in R12 band even toward high latitude area (see Figure 2.3). Therefore the anti-correlation cannot be explained by the absorption of emission outside the Galactic plane. It is interpreted as a displacement of the neutral matter by hot plasma with temperature of $\sim 10^6$ K that is close to the solar neighborhood; the solar system is embedded in a hot plasma, and in the directions in which the hot plasma is more extended, the column density of the neutral matter is smaller on the contrary (Snowden et al. 1990).

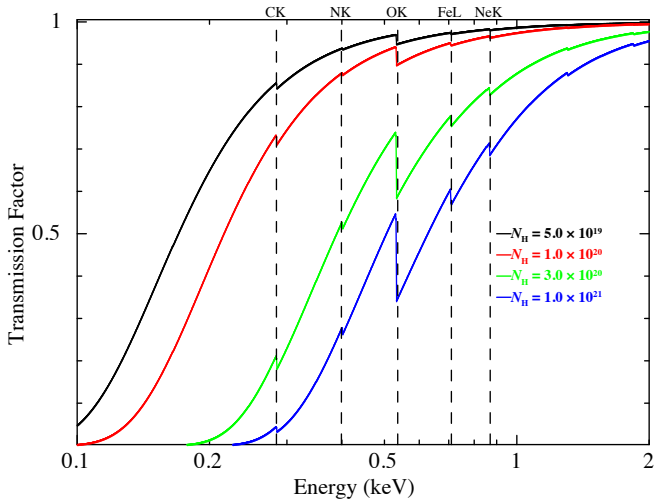

Figure 2.3 X-ray transmission factors to the cold ISM from 0.1 to 2.0 keV with different neutral hydrogen column densities. The dominant X-ray absorption edges are shown by vertical dashed lines.

X-ray emissions in R45 and R67 bands are quite uniform except the Galactic center region. Toward center region, X-ray emission is attributed to hot plasma of Galactic bulge and the famous supernova remnants (LoopI). The origin of this SXDB uniformity was directly indicated by the microcalorimeter observation onboard Wisconsin sounding rocket McCammon et al. (2002). Figure 2.4 left shows the SXDB spectrum toward high galactic latitude region centered at $(\ell, b) \simeq (90°, 60°)$ with 0.81 sr field of view (FOV). High resolution spectroscopy was achieved with an X–ray quantum microcalorimeter (XQC) whose energy resolution was ~ 9 eV (FWHM), while the low statistics is due to the short exposure ~ 100 s on the target. Strong lines at O VII Kα (561–574 eV, He-like triplet) and O VIII Lyα (653 eV, H-like doublet) were clearly identified on the spectrum in R45 band. The intensities of these lines are determined from the spectral fitting and results are summarized in Table 2.2.

Figure 2.4 right shows contributions to the observed total SXDB emission. The blue circles and

Table 2.2 Observed X-ray emission lines with XQC.

Line Identification	Line Energy eV	Photon Flux photons $s^{-1}cm^{-2}$ sr^{-1}	Energy Flux ergs $s^{-1}cm^{-2}$ sr^{-1}
FeIX, FeX, FeXI	$69 - 72$	100 ± 50	$(1.1 \pm 0.6) \times 10^{-8}$
CVI	368	5.4 ± 2.3	$(3.2 \pm 1.2) \times 10^{-9}$
OVII (triplet)	$561 - 574$	4.8 ± 0.8	$(4.4 \pm 0.7) \times 10^{-9}$
OVIII	653	1.6 ± 0.4	$(1.7 \pm 0.4) \times 10^{-9}$

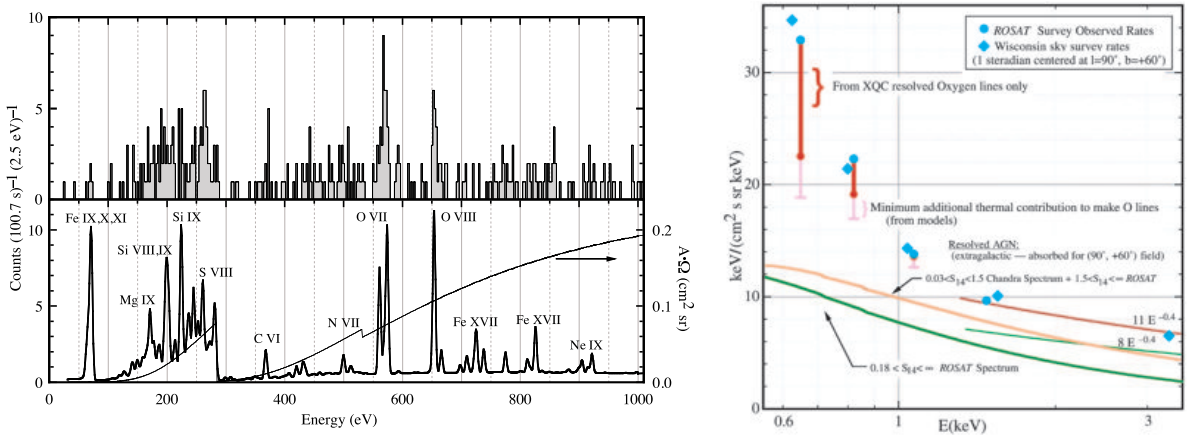

Figure 2.4 Results of X–ray quantum microcalorimeter (XQC) observation toward high galactic latitude (McCammon et al. (2002)). Left : SXDB Spectrum. The top panel shows the raw spectrum of XQC and the second one is the best fit model of it with XQC effective area. Right : contributions to the observed total diffuse background.

diamonds show the total observed sky survey rates. The red bars extending down from these are the contribution to these band rates from the OVII and OVIII fluxes observed with XQC. The magenta extensions on these bars are the almost model-independent minimum additional thermal emission that must be associated with the plasma producing the oxygen lines. The upper AGN spectrum (orange line) is the total flux that has currently been resolved into discrete sources. The gap between this and the bottom of the bars represents an absolute upper limit to any truly diffuse extragalactic source. The lines labeled $8E^{-0.4}$ and $11E^{-0.4}$ represent lower and upper limits to the CXB intensity in the $2 - 10$ keV range, as determined by several experiments. The contribution of CXB to the SXDB in R45 band is estimated up to ~ 40 %, and most of the remaining 60 % is the superposition of emission lines, especially affected by OVII Kα (0.57 keV) and OVIII Lyα (0.65 keV) emissions.

We review each SXDB component and explain the present understanding of the breakdown of the SXDB in the following sections.

2.3 Cosmic X-ray Background

In 1980's, the spectrum in the 3–50 keV range was found to resemble that of a hot plasma with a temperature of $\sim$ 40 keV (Marshall et al. 1980). This introduced the hypothesis that hot plasma is filling the universe. However, the low level of distortion of the cosmic microwave background (CMB) spectrum by the Compton up-scattering measured with COBE ruled out this possibility, implying that the origin of this emission, called "cosmic X-ray background (CXB)", is the superposition of faint discrete sources (Mather et al. 1994). A number of observations were conducted to resolve the CXB into discrete sources : with ROSAT (Hasinger et al. 1993), ASCA (Gendreau et al. 1995), XMM (Moretti et al. 2003), and Chandra (Mushotzky et al. 2000; Moretti et al. 2003; Yang et al. 2004; Hickox & Markevitch 2006). By virtue of the excellent spatial resolution of Chandra, 80–89 % of the CXB in 20-10 keV are resolved into individual sources (Moretti et al. 2003). Present understanding is that the CXB above $\sim$ 2 keV originates from numerous faint extragalactic sources; mostly AGNs (for a review see Brandt & Hasinger 2005). The energy spectrum of the CXB in 2–10 keV well reproduced by the single power-law function :

$$f(E) = N \left(\frac{E}{1 \text{ keV}} \right)^{-\Gamma} \text{ photons s}^{-1} \text{ cm}^{-2} \text{ sr}^{-1} \text{ keV}^{-1} , \tag{2.8}$$

where $N = 9.8 \pm 0.3$ photons s^{-1} cm^{-2} sr^{-1} keV^{-1} and $\Gamma = 1.42 \pm 0.02$ (Revnivtsev et al. 2005). However, the origin of SXDB, namely the diffuse emission below 1 keV, is more complicated. Excess emission to the interpolation of the CXB emission above $\sim$ 2 keV was first discovered by sounding rockets experiments in 1970s.

Because of the "contamination" of the Galactic emission, the spectrum of the CXB below $\sim$ 1 keV can not be observed directly. However, with ROSAT and Chandra, a large fraction of the CXB in 0.2–2 keV range has been resolved into individual sources. Thus we can estimate the CXB spectrum from the stacked (summed) composite spectrum. The individual sources resolved with the Chandra deep observation of the SSA 14 field (Mushotzky et al. 2000) show wide variety of spectra in 0.5–8 keV; from hard spectra of a negative photon index to soft spectra with a photon index larger than 2. There is clear tendency that the faint sources are harder. If we sum the spectra of sources brighter than 1×10^{-13} erg s^{-1} cm^{-2} in 2-10 keV, we obtain a power-law spectrum with a photon index of $\Gamma = 1.63$. On the other hand, if we sum all the sources, a photon index of $\Gamma = 1.42$ is obtained.

In the low energy range of below $\sim$ 1 keV, the contribution of hard sources to the CXB become smaller than in the hard band ($>\sim$ 2 keV). Thus the CXB spectrum in the low energy band should be softer than that of the hard band. Actually summed spectrum of the soft-band-selected sources from the Lockman hole ROSAT observation is represented by a power function of a photon index of $\Gamma = 1.96$ in the 0.1– 2.0 keV energy band (Hasinger et al. 1993). The normalization of the power law function was 7.8 ± 0.3 photons s^{-1} cm^{-2} str^{-1} keV^{-1}. Comparing the normalization of the CXB power-law function in 2-10 keV, we find that about 80 % of the CXB in 0.1–2keV is resolved. Thus it is likely that the CXB in < 2 keV has a steeper spectrum than in > 2 keV.

Smith et al. (2007) proposed to use the following model function as the CXB, basing on the above ROSAT result and unpublished Chandra results:

$$f_{\rm CXB}(E) = \begin{cases} A\left(\frac{E}{1\ {\rm keV}}\right)^{-1.54} + B\left(\frac{E}{1{\rm keV}}\right)^{-1.96} & \text{for } E < \ 1.2{\rm keV} \\ C\left(\frac{E}{1\ {\rm keV}}\right)^{-1.4} & \text{for } E \geq \ 1.2{\rm keV}, \end{cases} \tag{2.9}$$

whee $A = 5.7$, $B = 4.6$, and $C = 9.7$ photons s^{-1} cm^{-2} sr^{-1} keV^{-1} as the nominal values. The brightness of the CXB shows field-to-field fluctuations. Thus when they apply this model in the spectral fits of a field, they fix the value of A to the nominal value and varies the value of B as a free parameter. The value of C is adjusted so that the spectrum is continuously connected at 1.2 keV.

2.4 Solar-Wind Charge Exchange

When a solar wind ion X^{Q+} interacts with a neutral atom N (mainly H and He), electrons bound in the neutral are transferred to the excited state of the ion $X^{*(Q-1)+}$, and move to the ground state with emitting X-rays corresponding to the de-excitation energy. Therefore, this basic charge exchange process is expressed by the following equation

$$X^{Q+} + N \ \rightarrow \ X^{*(Q-1)+} + N^{+} \ \rightarrow \ X^{(Q-1)+} + N^{+} + h\nu \ . \tag{2.10}$$

The observed intensity of charge exchange (CX) induced emission line in a line of sight (LOS) is calculated

$$I = \frac{1}{4\pi}\int_0^{\rm LOS} y_{if}\, N_{X^{Q+}}(r)\, v_{\rm rel}\, \sigma_{(N,X^{Q+})}\, n_N(r)\ dr$$
$$\text{in unit of Line Unit (LU)} \equiv {\rm photons\,s^{-1}\,cm^{-2}\,sr^{-1}}\ , \tag{2.11}$$

where $N_{X^{Q+}}(r)$ and $n_N(r)$ are ion and neutral densities, $v_{\rm rel}$ and $\sigma_{(N,X^{Q+})}$ are relative velocity and cross section between them, and y_{if} is the photon yield of the interesting transition of the state $i \rightarrow f$, respectively (however, the energy dependence of the CX reaction is ignored. Averaged values of $N_{X^{Q+}}(r, E)$, $n_N(r, E)$, $\sigma_{(N,X^{Q+})}(E)$ are used for the simplification in the above equation). The position $r = 0$ is taken at the observer.

In this thesis, we especially focus on the contribution of the SWCX induced emission to the variability of SXDB in Chapter §5 and §6. Therefore, we describe more information about SWCX in the following subsections.

2.4.1 Discovery of the Solar-Wind Charge Exchange

The first discovery of the SWCX interaction came from the observation of comet Hyakutake with ROSAT satellite (Lisse et al. 1996). When C/Hyakutake passed at the close perigee (minimum geocentric distance was 0.102 AU from the Sun), ROSAT detected the X-ray and EUV emission in 0.09–2.0 keV band. Figure 2.5 shows a images of comet Hyakutake with ROSAT high resolution

imager (HRI, micro–channel plate with a field of view of 38′.0 with 2″ FWHM spatial resolution and whose energy range is 90 to 2100 eV) and wide field camera (WFC, same one with a field of view of 5° with 2′.3 HEW*1 spatial resolution and whose energy range is 90 to 206 eV), and comparison with optical image. Position of the detected photons were corrected for the motion of the comet during the observation. The origin of the cometary emission was expected to correlate with the solar activity by following three results. :

1. The emission was clearly offset sunward in 8 observations, except the short exposure one (Fig. 2.5 right).
2. The emission morphology of the comet was symmetric around the direction from the comet's nucleus to the Sun. However, it is not symmetric to a direction of a comet's motion with respect to the interplanetary neutrals.
3. The X-ray emissivity varies with slow (∼ several days) and impulsive (∼ a few hours) time scales. The latter short term variation was consistent with the enhancement of solar wind proton density observed with GOES-8 satellite.

The results 1 and 2 suggested that the origin of cometary X-ray emission had been related to interactions with solar X-ray photons or charged particles. Therefore, some interactions (solar X-ray scattering, and bremsstralung) were raised for the origin of the cometary emission in the paper. However all of them were inadequate, because the interaction cross sections are to small too to explain the observed luminosity. Note that the charge exchange process was not considered that time. Cravens (1997) first explained this unknown cometary X-ray emission by assuming the charge exchange reaction between the solar wind heavy ions and cometary neutrals. Charge exchange process has large cross section, because the transferred electron can be captured in orbits with large main quantum numbers. Combined models consisting of comet atmosphere, solar wind, and atomic transition physics successfully indicated the X-ray spectrum, morphology, and luminosity as well as their temporal variabilities.

2.4.2 Geocoronal Solar-Wind Charge Exchange

During the ROSAT all sky survey (RASS) campaign, unexpected temporal X-ray emissivity variation unrelated to any bright point source was observed with several tens ks to a few days scale, and affected especially at low energy band (R12 and R45, from 0.1 to 1.2 keV). Though LTEs were recognized before the comet observation, the origin of it was not revealed until the first SWCX discovery in 1997. From the discovery of SWCX-induced emission from the comets, it was soon realized that the same process should also occur at the geocorona. ROSAT "Long Term Enhancements" (LTEs, Snowden et al. 1994) problem was also explained by this geocoronal SWCX (G-SWCX) in the earth exosphere (Cox 1998, Fig.2.6).

X-ray observatories after the ROSAT era made it possible to reveal further physical properties of

*1 Half Energy Width

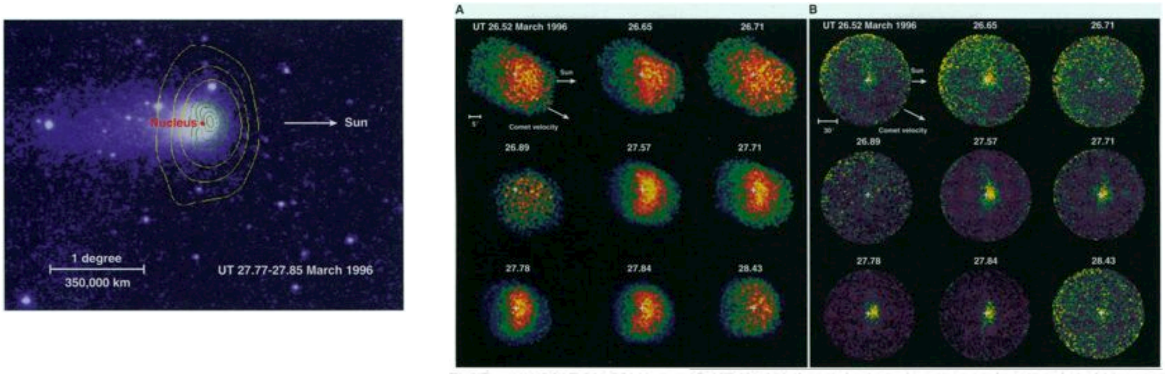

Figure 2.5 ROSAT observation of Comet C/Hyakytake 1996 B2 (from Lisse et al. (1996)). Left panel : The X–ray contours HRI (green) and WFC (yellow) overlaid on the optical image. Right panel : Time variations of HRI X-ray (0.1–2.0 keV, A) and EUV WFC (0.09–0.2 keV, B) images.

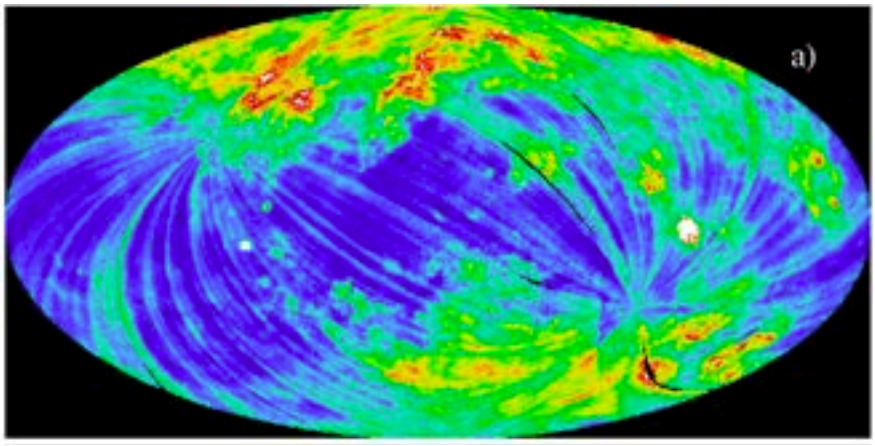

Figure 2.6 Enhanced X-ray emission observed during ROSAT all-sky survey in R12 band (0.11–0.284 keV). X-ray enhancement were caused along the lines of ROSAT scanning path done in ecliptic coordinate (Snowden et al. (2009)).

the G-SWCX induced emission from the high resolution image and spectroscopic analysis. Wargelin et al. (2004) directly showed the spectroscopic G-SWCX emission enhancement up to $\sim 2 \times 10^{-6}$ photons s^{-1} arcmin^{-2} cm^{-2} in 500–900 eV (primarily OVII and OVIII) of the "dark" side Moon observations with Chandra. The most straightforward method for discriminating the G-SWCX is to utilize its temporal variability. In Snowden et al. (2004), XMM-Newton observed Hubble Deep Field North where typical bright sources did not exist in the XMM FOV. During the observation, corotating interaction region (CIR), where slow solar wind is compressed by fast one and solar wind flux were enhanced, passed around the Earth. X-ray light curve at oxygen lines band (0.52–0.75 keV) was enhanced by the CIR passage.

Suzaku discovered further strong evidence of the G-SWCX induced emission in Fujimoto et al. (2007). Definite correlation was also shown between the intensity of G-SWCX induced lines and solar wind ion fluxes when interplanetary coronal mass ejection (ICME) passed around the Earth. Strong X-ray emission line of $\sim 3.09^{+0.74}_{-0.76}$ LU from CVI Lyδ transition (459 eV, $4p \rightarrow 1s$) that is

a typical signal from the charge exchange process (Kharchenko et al. 2003) was clearly detected. Since Suzaku revolves in the low earth orbit $\sim$ 550 km from the surface, observations were done inside the geomagnetic dipole field. When the cusp region of the dipole field came into the Suzaku line of sight, X-ray light curve in 0.3–2.0 keV was enhanced in synchronization with it (Figure 2.7, schematic view of the configuration is shown in the right one).

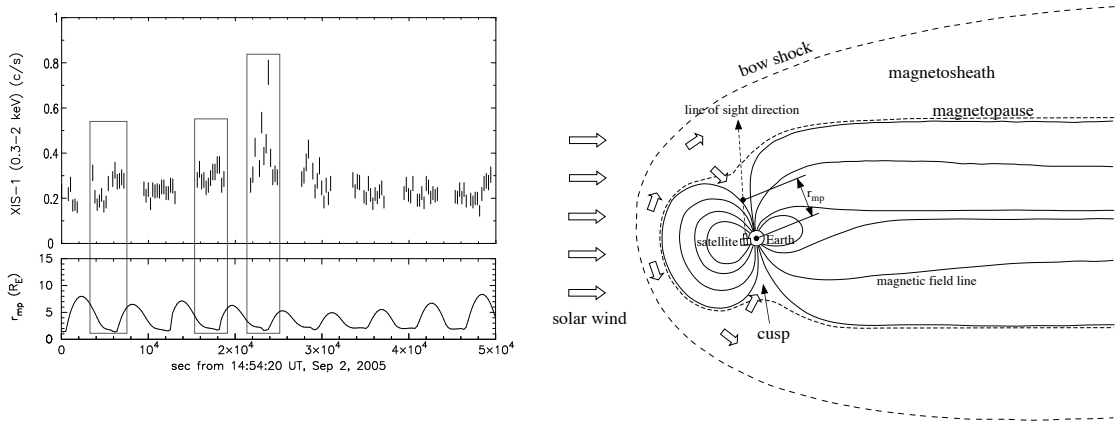

Figure 2.7 Correlation between the Suzaku 0.3–2.0 keV light curve and the geomagnetic field in the line of sight (Fujimoto et al. (2007)). The parameter $r_{\rm mp}$ in the left figure shows the distance from center of the earth to the point where the geomagnetic field becomes open to the interplanetary space in unit of earth radii. Configuration among the Suzaku satellite, solar wind flow, and geomagnetic dipole field is schematically shown in the right figure.

The G-SWCX induced emission was intensively modeled to reproduce the observation results. The solar wind ion flux roughly obeys r^{-2} dependence from the Sun, and it is treated as the constant value at 1AU. The scale height of the geocoronal neutral is known about 10 $R_{\rm E}$ from the Earth surface (Hodges 1994). In Yoshino (2009), the empirical model of the H distribution derived from the Lyα observation (Østgaard et al. 2003)

$$n_{\rm H}(r) = 10000 \exp\left(-\frac{r}{1.02}\right) + 70 \exp\left(-\frac{r}{8.2}\right) \quad {\rm cm}^{-3}, \tag{2.12}$$

where r shows the geocentric distance, were used for calculating the G-SWCX induced line intensity. Substituting the equation (2.12) and typical solar wind properties summarized in Koutroumpa et al. (2006) into the equation (2.11), the intensity of OVII line (the most bright line in R45 band) is derived in the case of Suzaku observation :

$$\begin{aligned} I_{\rm OVII} &= \frac{1}{4\pi}\,\sigma_{\rm CX}\,A({\rm O}^{+7})\,f_{\rm sw}\int_{r_{\rm mp}}^{\infty} n_{\rm H}(r)\,dr \\ &= \left\{ \begin{array}{ll} 0.33 \text{ LU} & \text{for } r_{\rm mp} = 10R_{\rm E} \\ 1.00 \text{ LU} & \text{for } r_{\rm mp} = 3R_{\rm E} \end{array} \right\} \left(\frac{\sigma_{\rm CX}\ {\rm cm}^{-2}}{3.4\times10^{-15}}\right)\left(\frac{A({\rm O}^{+7})}{0.2/1780}\right)\left(\frac{f_{\rm sw}\ {\rm cm}^{-2}{\rm s}^{-1}}{1.0\times10^{8}}\right), \end{aligned} \tag{2.13}$$

where $A({\rm O}^{+7})$, and $f_{\rm sw}$ are the solar wind abundance ratio of O^{+7} to proton and proton flux expressed by the product of density and relative velocity to the geoconal neutrals. The minimum height penetrating the solar wind to geocorona is determined by the distance $r_{\rm mp}$ in Suzaku line of sight (Figure 2.7 right) from the earth surface to the magnetopause where is the abrupt boundary between the solar wind ram pressure and geomagnetic one. According to the equation, G-SWCX

induced OVII emission will comprise a few tens percent of SXDB one, if the $r_{\rm mp}$ becomes smaller than $3R_{\rm E}$ or $f_{\rm sw}$ exceeds 4.0×10^8 cm^{-2}s^{-1} (Yoshino 2009).

2.4.3 Heliospheric Solar-Wind Charge Exchange

Simultaneously with the first notice of G-SWCX as an origin of ROSAT LTE, Cox (1998) also pointed out the presence of SWCX interaction with the interplanetary neutrals in the heliosphere distributed within $\sim$ 100 AU from the Sun. The solar system is embed in the local interstellar cloud (LIC), and the neutral species are attracted to the Sun's gravity. Solar wind ions collide with these neutrals deeply penetrating inside the heliosphere and charge exchange processes occur between them.

This heliospheric SWCX (H-SWCX) induced emission is thought to contribute as the "DC" offset level of the SXDB ; the solar wind ($\sim$ several hundred km s^{-1}) travels roughly a quarter of an AU per day, and the quiescent H-SWCX emission is an integral of the solar wind conditions over the previous year. Since the variable part of the SWCX emission was fairly effectively removed from the RASS data, it is the quiescent component producing the observed 1 keV background. Given the above spatial scale of H-SWCX, it is less susceptible to the temporal solar wind variation than G-SWCX. It is hard to identify the H-SWCX from the time variability, and the clear evidence of the H-SWCX is not obtained yet.

Instead of the time variability, the key to quantify the H-SWCX is to observe its spatial anisotropy. If the H-SWCX actually contributes to a certain amount of RASS map, long term emissivity variation related to the 11-year solar cycle and the inhomogeneity of the interstellar medium around the Sun is expected. As these variations are not clearly observed yet, Koutroumpa et al. (2006) simulated the all sky emissivity map of the H-SWCX induced OVI and OVIII lines on the basis of averaged, minimum and maximum solar activity in Solar Cycle 22. They obtained different OVI and OVIII maps with solar activity level, especially toward the high ecliptic latitude direction. This difference is mainly caused by the slow/fast solar wind distributions on the Sun's surface (McComas et al. 2008). Due to the difference of plasma temperature, O^{+7} and O^{+8} ionization fractions of the slow solar wind (higher temperature) is much larger than those of fast one. Conversely, the fast wind abounds in the fractions of lower order oxygen ions than O^{+7}. Figure 2.8 shows the solar activity from 1992 to 2010. During the solar minimum phase, the slow wind is suppressed within a low heliocentric ecliptic latitude area $|\beta| \lesssim 20°$, and the fast one widely extends from the polar regions (McComas et al. 2008). On the other hand, the slow wind almost covers the whole external surface of the Sun during the maximum phase.

The most influential dense neutral atom region to the H-SWCX anisotropy is "Helium Focusing Cone (HeFC)" : the cone-shaped structure in the down-flow direction of interstellar flow where interstellar He atoms are concentrated due to the Sun's gravity. From the observations of the He^+ pickup ion (Gloeckler et al. 2004) and backscattered HeI Lyα emission (Lallement et al. 2004b), the axis of the HeFC is derived at (74°.3, −5°.3). The pioneer research to investigate the observational evidence of the H-SWCX enhancement at the HeFC (Cox 1998) were Koutroumpa et al. (2007)

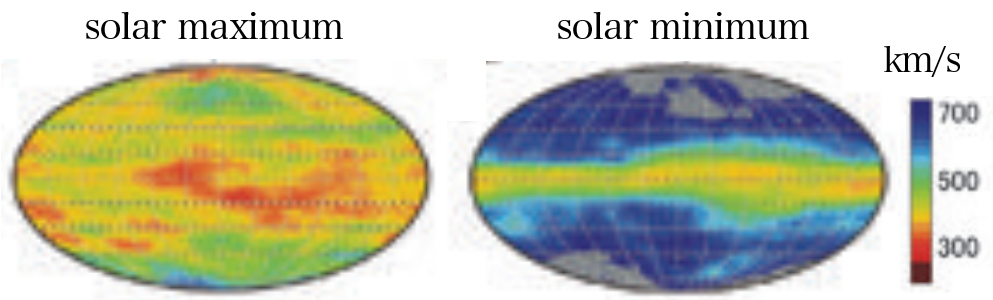

Figure 2.8 Images of solar wind distribution at the maximum and minimum phases observed by the interplanetary scintillation (http://stsw1.stelab.nagoya-u.ac.jp/).

and Koutroumpa et al. (2009b). Koutroumpa et al. (2007) compared the observed intensities of OVII and OVIII line with their H-SWCX emission model including the effect of Parker's spiral and propagation of interplanetary coronal mass ejection. The variations of observed intensities were consistent with the model prediction toward shadowing clouds (MBM 12 and South Galactic Filament). Especially, the model suggested that the variations toward MBM 12 (λ, $\beta = 47°.4$, $2°.6$) was caused by the enhancement of H-SWCX emission at HeFC. In Koutroumpa et al. (2009b), one of the multiple observations toward the south ecliptic pole ($\beta = -90°$) with XMM detected the maximum intensity of OVII and OVIII lines when the Earth revolves at the heliocentric ecliptic longitude $\lambda = 72°$. This is almost consistent with the axis of the HeFC. The observed intensity enhancement is 2.1 ± 1.3 LU at OVII and 2.0 ± 0.9 LU at OVIII.

The latest H-SWCX emission model is summarized in Koutroumpa et al. (2006). The specifics of H-SWCX induced emission model we also use in the later sections are summarized in Appendix A.

2.5 Local Bubble

It is widely believed that the hot plasma, so-called Local Bubble (LB), is the result of one or more supernova (SN) explosions (Cox & Anderson 1982). Modeling of the joint evolution of the Loop I and LB involve ~ 20 SNe occurring in the moving group of OB stars of the Sco-Cen cluster which passed through the present day local cavity. In such a scenario the formation age of the Local Hot Bubble is constrained to ~ 14.5 Myr, with the last re-heating occurring ~ 0.5 Myr ago (Breitschwerdt & de Avillez 2006). The history and age of the Local Bubble are much debated. Early observations with rocket-borne instruments led to the conclusion that the ROSAT 1/4 keV or M-band diffuse emission was dominated by hot and rarefied plasma with temperature of $T \sim 10^6$ K and density of $n_{\rm H} \sim 0.005$ cm^{-3}, embedded in a ~ 100 pc cavity of the cold ISM in which the Solar System resides (McCammon & Sanders 1990). Several clouds of warm $\sim 10^4$ K gas reside within the hot plasma, and one of these clouds, the LIC, envelops the Solar System.

Figure 2.9 shows the distribution of cold and neutral gas within ± 250 pc of the Sun revealed by interstellar NaI (λ 5890 Å) absorption measurements toward nearby stars (Lallement 2003).

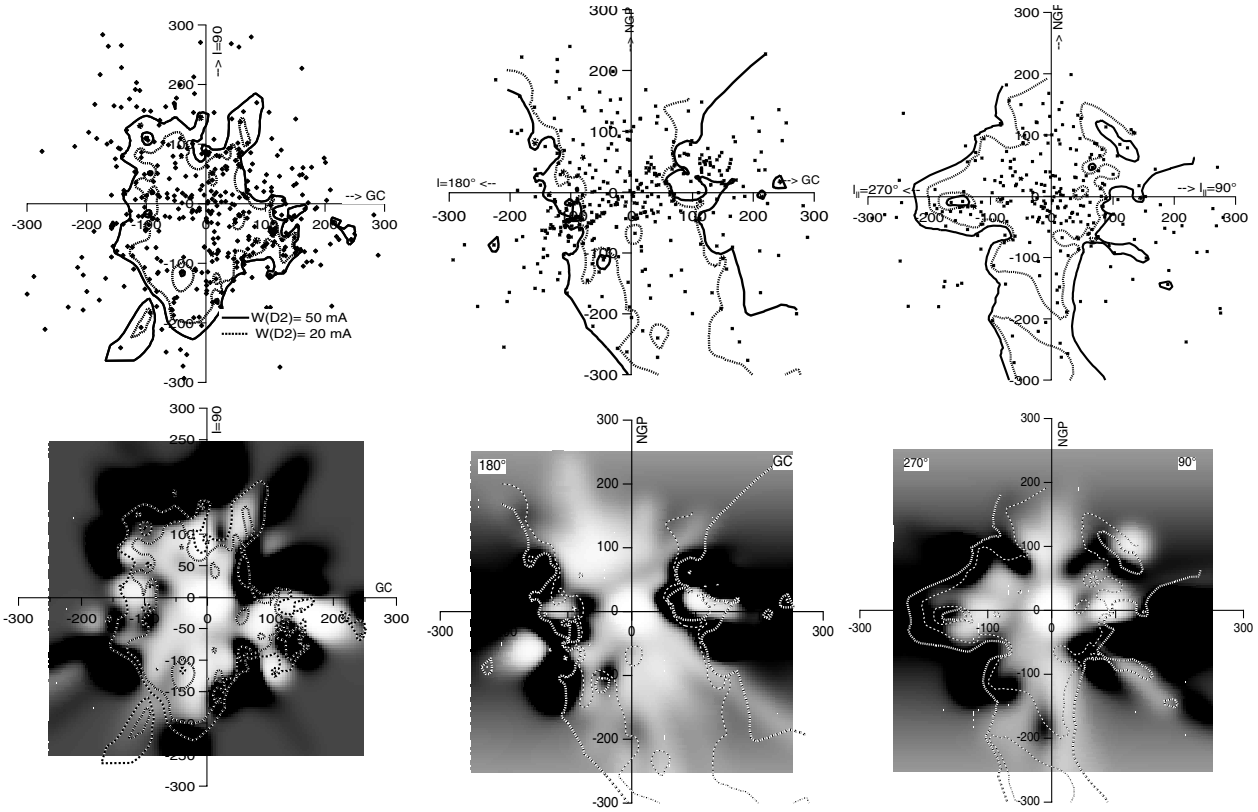

Figure 2.9 3D mapping of the Local Bubble using the NaI absorption lines in the galactic (left), meridian (center), and rotation (rotation) planes. Top panel : iso-equivalent width contours for $W = 20$ mÅ and 50 mÅ. Bottom pannel : cut in the 3D density obtained from the global inversion of the column densities.

Three panels are cross-sectional images of the galactic (left), meridian (center), and rotation (rotation) planes, respectively. Dark contour regions in the bottom panels represent neutral gas with $N_{\rm H} > 10^{19.3}$ cm^{-2}, and white regions are of low gas density of $N_{\rm H} < 10^{18.3}$ cm^{-2}. Interstellar absorption due to the NaI atom is a good indicator of the total amount of neutral interstellar gas in a particular line of sight, because NaI generally exists in gas whose temperature is $T < 1000$ K and predominantly neutral interstellar regions. The region of extremely low density (Local Cavity) varies in radius from 40 to 200 pc.

The interesting interstellar feature of these maps is extensions of the Local Cavity into the lower galactic halo (middle and right panels of Figure 2.9) through both of the open-ends of a rarefied "Local Chimney" feature. The SXDB emission toward the Local Chimney is bright in ROSAT R12 band (Figure 2.2). Koutroumpa et al. (2009a) made a comparison between observed ROSAT R12 emission and simulated H-SWCX induced one. The simulation can account for most of the observed emission at low galactic latitudes, but not at galactic latitudes above $|b| > 30°$. The region where the observed R12 fluxes are significantly larger than simulated H-SWCX one is consistent with the open-ends of Local Chimney (Figure 2.10).

Within the temperature changes between LB ($\sim 10^6$ K) and warm gas ($\sim 10^4$ K), intermediate temperature gas is expected to find in the transition zones between the clouds and the hot bubble

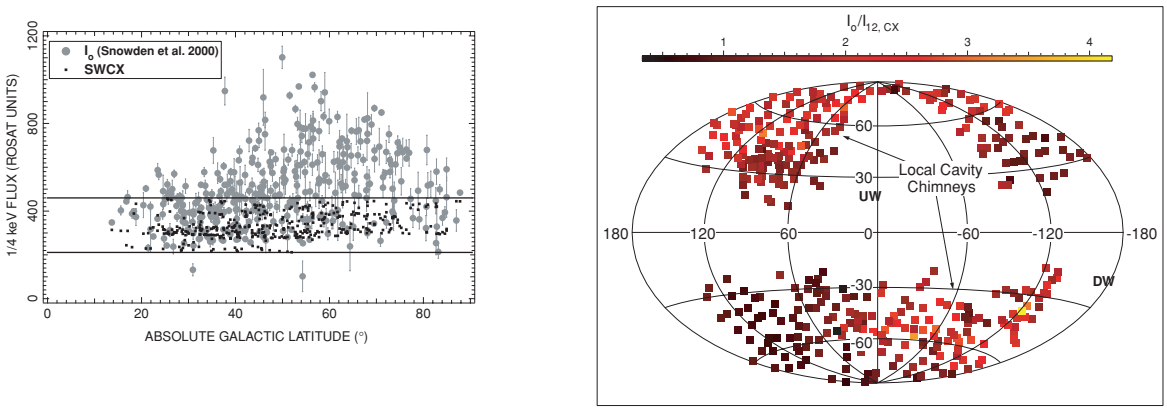

Figure 2.10 Comparison between ROSAT R12 intensity and predicted H-SWCX induced emission for 378 shadowing observations (Koutroumpa et al. (2009a)). Left : observed R12 flux (gray circle) and simulated H-SWCX flux (black dot). Right : observed flux data over simulated H-SWCX flux ratio map in galactic coordinate.

plasma. The OVI ion is a tracer of $\sim 3 \times 10^5$ K gas. Gas of this temperature is thermally unstable; it does not remain at this temperature for long periods unless hotter gas is present to resupply it. In analyses of FUSE (Far Ultra-violet Spectroscopic Explorer) data, OVI absorption lines are detected towards stars within a hundred parsecs of the Sun (Savage & Nicolas 2006). This distance range is thought to be similar to the LB's radius, which was determined from data on a molecular cloud residing just inside the LB boundary. According to Shelton (2009), the observed OVI ions are larger than the solar wind composition, and cannot be attributed to the solar wind ions or SWCX. The origin of OVI ion is therefore associated with the hot-cold ISM transition phase. However, EUV observations with CHIPS (Cosmic Hot Interstellar Plasma Spectrometer) satellite have suggested that 10^6 K hot gas occupies small region in LB (Hurwitz et al. 2005). The picture of the LB became more complicated from the first discovery of the SWCX and the presence of the 10^6 K hot gas has been debated even today (troubles with the LB are described in §2.7.1).

2.6 Galactic Halo

High energy emission data from ROSAT, XMM-Newton, and Suzaku, and X-ray absorption line data from Chandra, show the presence of hotter gas bound in the Galactic halo, with temperatures up to $T \sim 3 \times 10^6$ K. Several possible origins for the hot halo gas have been suggested, including supernova (SN) or stellar wind-driven outflows from the Galactic disk, gravitational heating of in-falling intergalactic materials and in situ heating by SNe above the plane.

In Yao et al. (2009) and Hagihara et al. (2010), they derive the physical properties of Galactic halo gas toward bright balzars from joint analysis using both Suzaku emission and Chandra absorption spectra simultaneously. Assuming vertically exponential distributions of the gas temperature and the density, the gas temperature and density at the Galactic plane and their scale heights as $3.6^{+1.1}_{-0.7} \times 10^6$ K, $1.4^{+2.0}_{-1.1} \times 10^{-3}$ cm^{-3}, $1.4^{+3.8}_{-1.2}$ kpc and $2.8^{+3.6}_{-1.8}$ kpc toward LMC-X3 at $(\ell,\ b) = (273°.4,\ -32°.6)$, while they are $2.5^{+0.6}_{-0.3} \times 10^6$ K, $1.4^{+0.5}_{-0.4} \times 10^{-3}$ cm^{-3}, $5.6^{+7.2}_{-4.2}$ kpc and $2.3^{+0.9}$

kpc toward PKS 2155-304 at $(\ell,\ b) = (17°.2,\ -52°.4)$, respectively.The parameters are consistent between two LOS.

2.7 Preceding Study of SXDB with recent X-ray Satellites

2.7.1 Shadowing Observations toward Dense Molecular Cloud

An well-used and successful way to study the local (closer than a few hundreds pc) component apart from distant emission is "shadowing" observations. This method uses an absorber, e.g, a molecular cloud, to block distant the component. By observing on-absorber and off-absorber directions, and assuming that the spatial variation is small betweens the two directions, both local (in front of the observer) and distant (behind the observer) emission were measured separately (Smith et al. 2007; Henly & Shelton 2008).

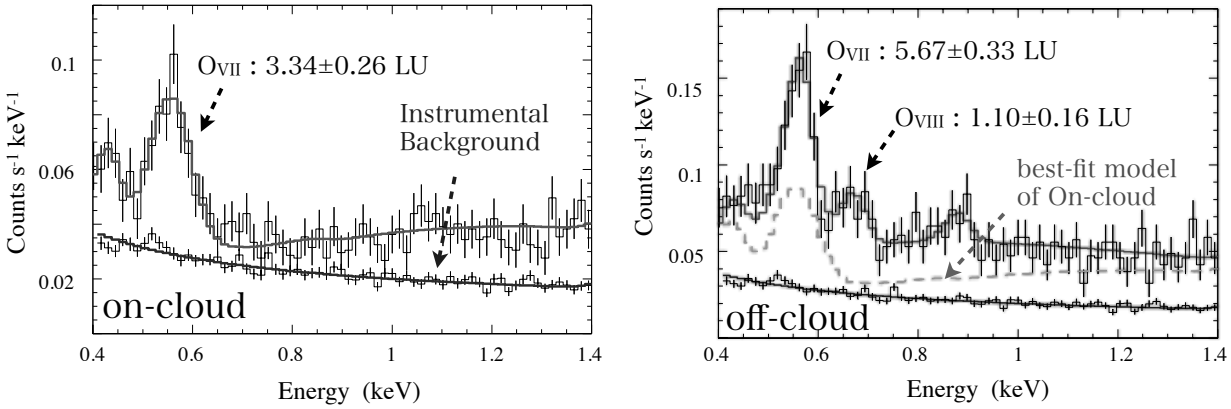

Figure 2.11 Suzaku observations toward MBM 12 (Smith et al. (2007)).

In Smith et al. (2007), they resolved local and distant emissions toward dense molecular cloud MBM 12 $(\ell,\ b) = (159.°20,\ -34.°47)$ existing ~ 100 pc away from us. Figure 2.11 shows the on-cloud (left) and off-cloud (right, $\sim 3°$ away from on-cloud) spectra toward MBM 12 observed with Suzaku with the best-fit models. OVII emission line was clearly detected with an intensity of 3.34 ± 0.26 LU toward MBM 12, and a net off-cloud OVII intensity is 2.34 ± 0.33 LU after subtracting the on-cloud foreground emission. If this more distant oxygen emission is from a thermal plasma in collisional equilibrium (CIE) beyond the Galactic disk, the temperature of it is calculated $(2.1 \pm 0.1) \times 10^6$ K with an emission measure of $(4 \pm 0.6) \times 10^{-3}$ cm^{-6}pc.

They also estimated the emission measure of the local 0.1 keV plasma (namely the LB) as 7.5×10^{-4} cm^{-6}pc assuming that the OVII emission obtained from the on-cloud spectrum is totally originated from the LB. This is inconsistent with the upper limit observed in EUV band. From the Fe lines near 72 eV observation with CHIPS (Cosmic Hot Interstellar Plasma Spectrometer), a 95 % upper limit of the emission measure is determined 4.0×10^{-4} cm^{-6}pc assuming the $10^{6.0}$ K hot gas with the solar abundance in LB (Hurwitz et al. 2005). This is one of the indirect evidences of the contribution from SWCX emission, and other papers argue that half of X-rays from local region

are due to the SWCX in ROSAT R12 band, and the most for OVII and OVIII lines (Robertson & Cravens 2003, Koutroumpa et al. 2007).

2.7.2 Systematic Analysis of OVII and OVIII emissions

In Yoshino et al. (2009), they showed a linear relation between OVII and OVIII intensities using Suzaku fourteen blank sky field observations toward various direction in the Galactic longitude $65° < \ell < 295°$, under removing the geocoronal SWCX. From their analysis, oxygen lines have following relation : (OVIII intensity) $= 0.5 \times$ [(OVII intensity) $-$ 2 LU], where they interpreted the proportional as distant thermal emissions from Galactic halo gas, and 2 LU OVII intercept as local emissions from LB and heliospheric SWCX. The linear component also suggests that temperatures averaged over each line of sight show a narrow distribution around ~ 0.2 keV, assuming the ionization fraction of solar abundance plasma in collisional ionization equilibrium (CIE).

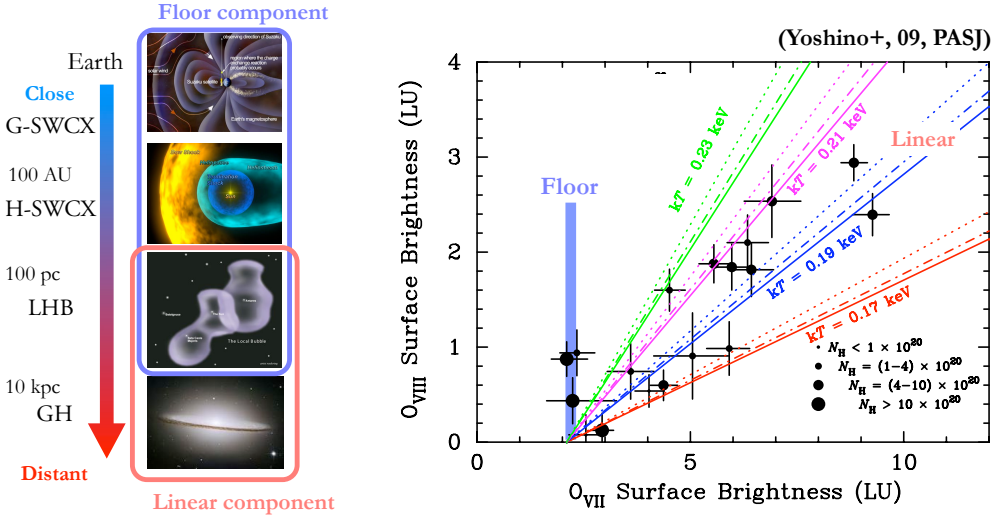

Figure 2.12 OVII v.s. OVIII emission relation toward fourteen field observed with Suzaku in Yoshino et al. (2009).

In Henly & Shelton (2010), they also derived the oxygen line intensities toward 303 blank field regions in $120° < \ell < 240°$, Figure 2.13 shows the measured oxygen intensities plotted against Galactic latitude. In the northern Galactic hemisphere, the OVII intensity is correlated with Galactic latitude. The intensity tends to increase from the Galactic plane to the north Galactic pole. This correlation exists with or without the proton flux filtering, and whether or not data from low Galactic latitudes are excluded. No such correlation exists for OVIII in the north. In the south, if we exclude the observations from low Galactic latitudes, we find that both the OVII and OVIII intensities are moderately correlated with latitude where the correlation implies a decrease from the Galactic plane to the south Galactic pole.

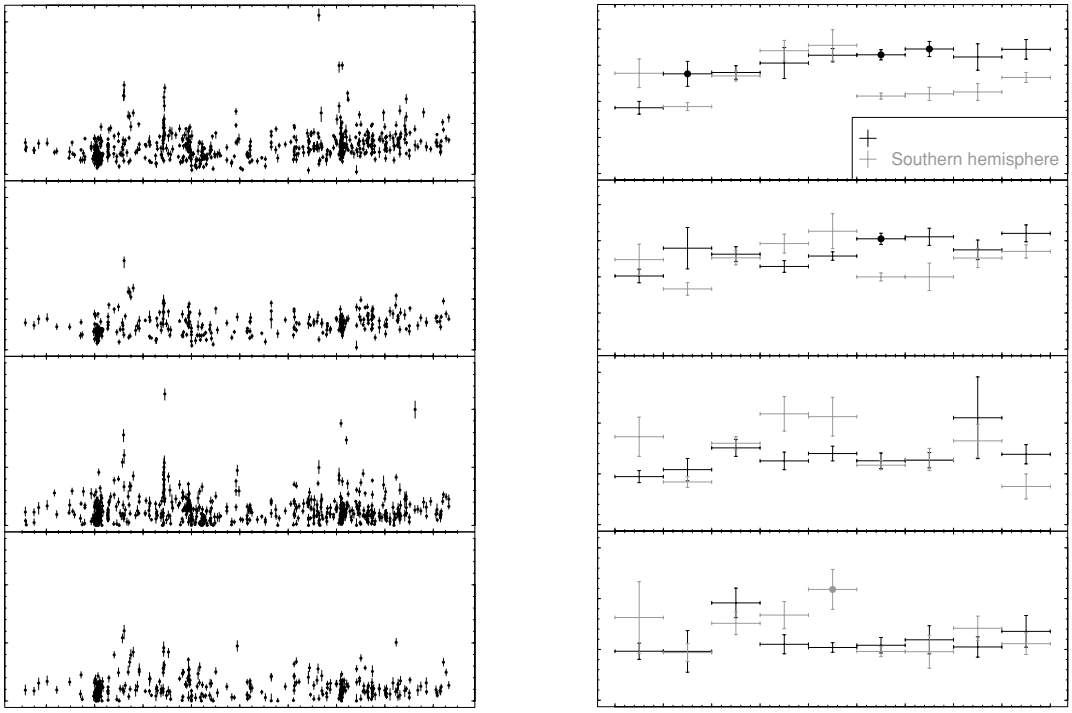

Figure 2.13 Variation of the observed oxygen line intensities with Galactic latitude (Henly & Shelton (2010)).

2.8 Summary of the Review

Currently, it is widely accepted that the SXDB consists of following 4 components :

1. Superposition of the extragalactic Active Galactic Nuclei (AGNs), represented by continuum emission called cosmic X-ray background (CXB).
2. Collisional ionization equilibrium (CIE) thin thermal plasma emission with temperature of $kT \sim 0.2$ keV in the Galactic halo absorbed by the neutrals in Galactic disk.
3. CIE thin thermal plasma with temperature of $kT \sim 0.1$ keV surrounding the solar system, so-called local bubble (LB).
4. Emission lines produced by the solar-wind charge exchange (SWCX) reaction with geocoronal or heliospheric interstellar neutrals.

The spectral shape of CXB is considered as a power law function, while those of the others consist of many emission lines. From the discovery of SWCX in 1997, breakdown of the SXDB to each emission component grows more opaque especially for the origins of line emission. This is caused by the time and spatial variabilities of H-SWCX induced emission, and it is hard to determine the physical properties of the distant plasma components.

Figure 2.14 shows a schematic view of the recent understanding about origins of SXDB from our solar system to the extragalactic space with their typical scales, based on the recent X-ray observation results. We are embed in a hierarchic structure from the SWCX to CXB, and hence it is hard to resolve the SXDB to each component. The contributions of local and distant emission can be separated by the shadowing method using a dense molecular cloud at $\sim$ 100 pc from us. However, there still remain two origins of local emission that are H-SWCX and LB. The contributions of these components to the SXDB are not proved clearly yet. To detect changes of emission intensities related to the 11-year solar activity and anisotropy of the distributions interplanetary neutrals are important to get the evidence of H-SWCX induced X-ray emission.

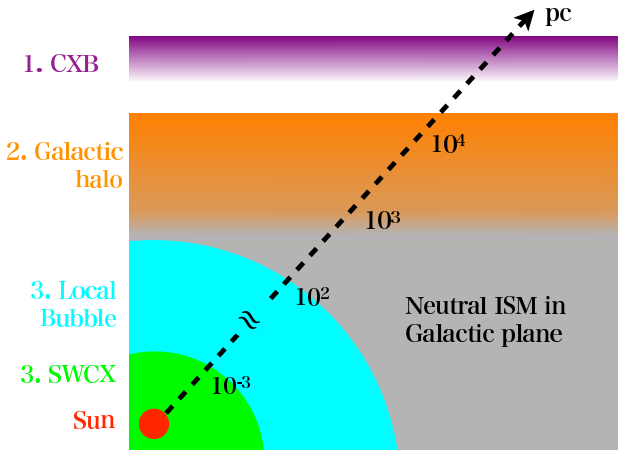

Figure 2.14 Schematic view of a recent understanding about origins of SXDB with their typical scales from us.

3 Instruments

3.1 Suzaku Satellite

3.1.1 Spacecraft

Suzaku is the fifth Japanese X-ray astronomy satellite. It was developed under Japan-US international collaboration and was launched on July 10, 2005, from JAXA Uchinoura Space Center. After launch, Suzaku first deployed the solar paddles and the extensible optical bench (EOB), and performed 10 days of the perigee-up orbit maneuver to get into a near circular orbit of a 570 km altitude with an inclination angle of 31°. The orbital period is about 96 minutes. Suzaku retains its excellent X-ray sensitivity, with high throughput over a broad-band energy range from 0.2 to 600 keV. Suzaku's broad bandpass, low background, and good CCD energy resolution makes it a unique tool capable of addressing a variety of outstanding problems in astrophysics.

The total mass at launch was 1706 kg. The five sets of X-ray mirrors are mounted on top of the EOB and five focal plane detectors and a hard X-ray detector are mounted on the base panel of the spacecraft (Figure 3.1 and 3.2). The spececraft length is 6.5 m along the telescope axis after the deployment of the EOB.

There are two gyroscopes mounted in skew directions, which provide redundancy. The spececraft pointing accuracy is approximately 0.24′ with a stability better than 0.022′ per 4 sec (a half of typical

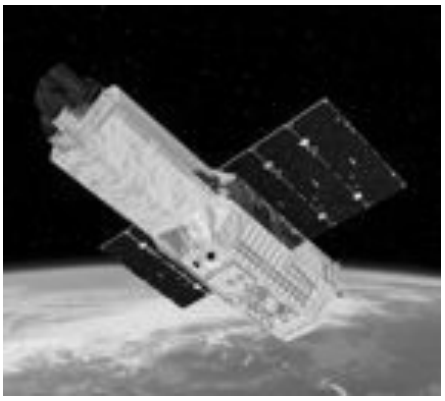

Figure 3.1 Schematic view of the Suzaku satellite in orbit.

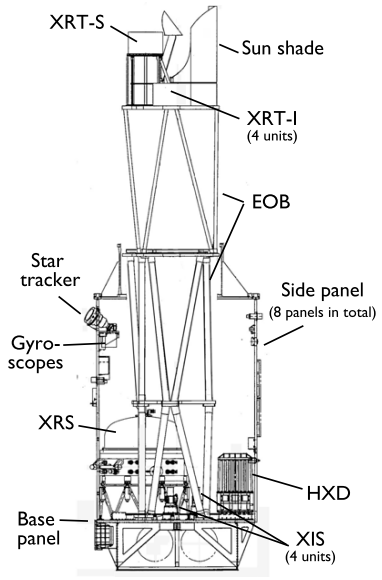

Figure 3.2 A side view of Suzaku with the internal structures after the EOB deployment (Mitsuda et al. (2007)).

exposure time of CCDs). Pointing direction of the telescope is limited by the power constraint of the solar paddle. The area of the sky accessible at a time is a belt within which the sun angle is between 65° and 115°. Any part of sky is accessible at least twice a year. The normal mode of operations will have the spacecraft pointing in a single direction for at least 1/4 day (10 ksec). Observation is also interrupted by passages of the South Atlantic Anomaly. The current projection is that the observing efficiency of the satellite will be about 43 %.

There are four X-ray sensitive imaging CCD cameras (X-ray Imaging Spectrometers, XISs, Koyama et al. 2007), three front-illuminated (FI named XIS0, 2, 3; energy range 0.4–12 keV) and one back-illuminated (BI named XIS1; energy range 0.2–12 keV), capable of moderate energy resolution. Each XIS is located in the focal plane of a dedicated X-ray telescope (XRT, Serlemitsos et al. 2007). General properties and Error Budgets of XRT and XIS are summarized in Table 3.1 and 3.2, respectively. In this thesis, we use the data observed with Suzaku XIS1 and describe the specifics of this instrument below (most of the information are referred from the Suzaku Technical Description[*1]).

Table 3.1 Overview of Suzaku capabilities.

S/C	Orbit apogee	568 km
	Orbital period	96 minutes
	Observing efficiency	$\sim$ 45 %
XRT	Focal length	4.75 m
	Field of view	$17'$ at 1.5 keV
		$13'$ at 8 keV
	Plate scale	0.724 arcmin/mm
	Effective area*	440 cm^2 at 1.5 keV
		250 cm^2 at 8 keV
	Angular resolution	$2'$ (HPD)
XIS	Field of view	$17.8' \times 17.8'$
	Bandpass	0.2–12 keV
	Pixel grid	1024×1024
	Pixel size	24 μm × 24 μm
	Energy resolution	$\sim$ 130 eV at 6 keV
	Effective area	340 cm^2 (FI), 390 cm^2 (BI) at 1.5 keV
	(incl XRT-I)	150 cm^2 (FI), 100 cm^2 (BI) at 8 keV
	Time resolution	8 s (Normal mode), 7.8 ms (P-Sum mode)

[*1] http://www.astro.isas.ac.jp/suzaku/doc/suzaku_td/

Table 3.2 Error Budgets of Scientific Instrument Calibrations.

	Calibration Item	Oct 2008	Requirement	Goal
XRT-I/XIS	On-axis effective area*	∼2%	5 %	5 %
	Vignetting*	∼10 %	5 %	2 %
	On-axis EEF †	∼3 %	5 %	1 %
	Off-axis EEF ‡	∼3 %	20 %	2 %
	Optical axis position in XIS	$\sim 0.5'$	$<0.2'$	$<0.2'$
	Energy scale	max(0.2%, 5eV)	0.1 %	0.1 %
	Energy resolution at 5.9 keV	5 % (FWHM) §	1 %	1 %
	Contamination thickness‖	$10^{18}\mathrm{cm}^{-2}$	N/A	N/A
	OBF integrity	unbroken	broken/unbroken	broken/unbroken

* Valid in the 1–8 keV band. Calibration uncertainty may become larger outside this energy range, especially below 0.3 keV (BI chip) and above 10 keV.

† For all integration radii from $1' - 6'$. No error on attitude control is included.

‡ As on-axis but for all XIS f.o.v. No calibration is currently scheduled.

§ When xisrmfgen is used. Note that an error of 5 % in the energy resolution could produce an artificial line width of as large as ∼25 eV in sigma at the iron band.

‖ Uncertainty represented as the carbon-equivalent column density. Valid only at the center of the field of view.

3.1.2 X-ray Telescope (XRT)

Basic Component

Suzaku has five light-weight thin-foil X-Ray Telescopes (XRTs). The XRTs have been developed jointly by NASA/GSFC, Nagoya University, Tokyo Metropolitan University, and ISAS/JAXA. These are grazing-incidence reflective optics consisting of compactly nested, thin conical elements. Because of the reflector's small thickness, they permit high density nesting and thus provide large collecting efficiency with a moderate imaging capability in the energy range of 0.2–12 keV, all accomplished in telescope units under 20 kg each, including the pre-collimators for rejection of stray lights. Four XRTs onboard Suzaku (XRT-I0 to XRT-I3) are used for the XIS.

The XRTs are arranged on the EOB on the spacecraft in the manner shown in Figure 3.3. The XRTs consist of closely nested thin-foil reflectors, reflecting X-ray at small grazing angles. An XRT is a cylindrical structure, having the following layered components :

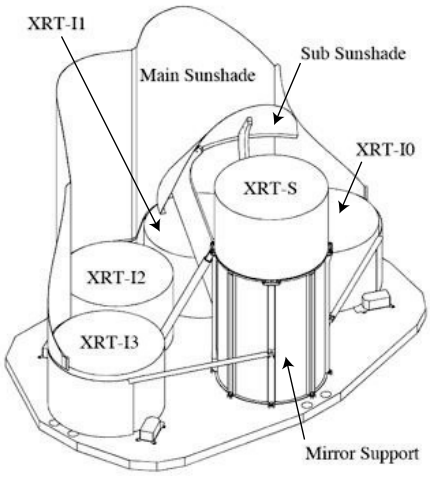

Figure 3.3 Schematic view of the Suzaku XRTs mounted on the top plate of the EOB.

Figure 3.4 Picture of the module XRT-I1.

1. a thermal shield at the entrance aperture to help maintain a uniform temperature,
2. a pre-collimator mounted on metal rings for stray light elimination,
3. a primary stage for the first X-ray reflection,
4. a secondary stage for the second X-ray reflection,
5. a base ring for structural integrity and interfacing with the EOB of the spacecraft.

All these components, except the base rings, are constructed in 90° segments. Four of these quadrants are coupled together by interconnect-couplers and also by the top and base rings (Figure 3.4). The telescope housings are made of aluminum for an optimal strength to mass ratio. Each reflector consists of a substrate also made of aluminum and an epoxy layer that couples the reflecting gold surface to the substrate. Including the alignment bars, collimating pieces, screws and washers, couplers, retaining plates, housing panels and rings, each XRT-I consists of over 4112 mechanically separated parts. In total, nearly 7000 qualified reflectors were used and over $\sim 1 \times 10^6$ cm^2 of gold surface was coated.

Angular Resolution

Figure 3.1.2 shows Point-Spread Function (PSF), and the Encircled Efficiency Function (EEF) of all the XRT (Serlemitsos et al. 2007). Verification of the imaging capability of the XRTs has been made with the data of a moderately bright point source (SS Cyg) observed at 2005 November 2. The EEF is normalized to unity at the edge of the CCD chip (a square of 17.′8 on a side). With this normalization, the Half-Power Diameter (HPD) of the XRT-I0 through I3, which is the diameter within which half of the focused X-rays are enclosed, is 1.′8, 2.′3, 2.′0, and 2.′0, respectively. These values are in general consistent with those expected from ground-based calibration measurements. The angular resolution does not significantly depend on the energy of the incident X-rays in the energy range of Suzaku, 0.2–12 keV.

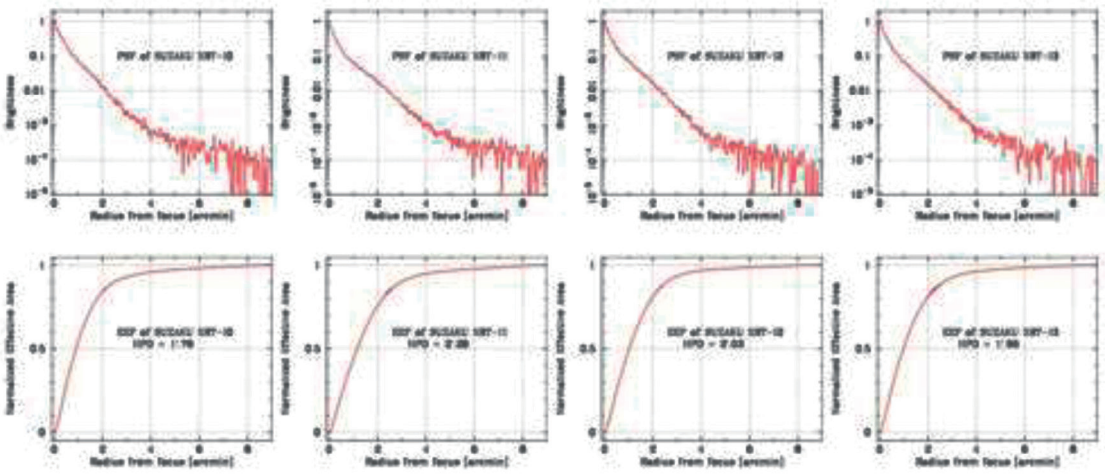

Figure 3.5 Point-Spread Function (PSF), and Encircled Efficiency Function (EEF) of the four XRT-I modules in the focal plane (Serlemitsos et al. (2007)).

Effective Area

The effective areas are typically 440 cm^2 at 1.5 keV and 250 cm^2 at 8 keV. The focal length of the XRT-I is 4.75 m. Actual focal lengths of the individual XRT quadrants deviate from the design values by a few cm. The optical axes of the quadrants of each XRT are aligned to within 2′ from the mechanical axis. The field of view for the XRT-Is is about 17′ at 1.5keV and 13′ at 8keV.

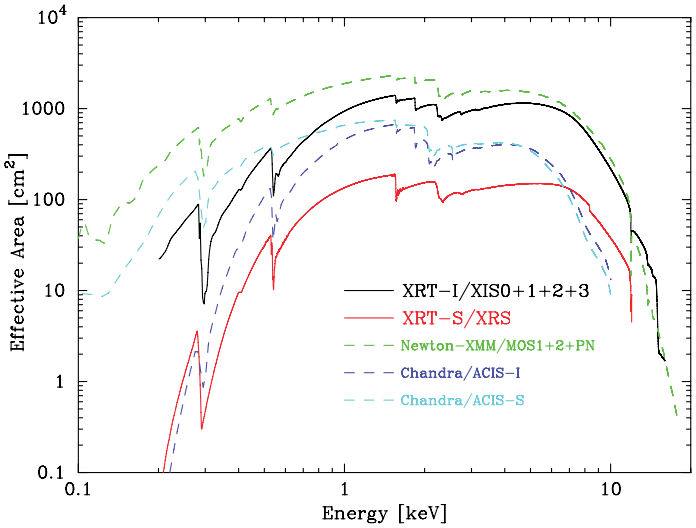

Figure 3.6 Total effective area of the four XRT-I modules in comparison with that of XMM-Newton and Chandra. Transmissions of the thermal shield and the optical blocking filter, and the quantum efficiency of the CCD are all taken into account.

Vignetting Effect

The vignetting curves calculated by the ray-tracing simulator are compared with the observed intensities of the Crab nebula at various off-axis angles. Figure 3.7 shows the vignetting curves in the two energy bands 3–6 keV and 8–10 keV. The counting rate of the Crab Nebula on the entire CCD field of view were calculated in every 0.′5 step using the ray-tracing simulator. Note that the abrupt drop of the model curves at $\sim 8'$ is due to the source approaching the detector edge. The vignetting over the XIS field of view predicted via ray-tracing coincides with that measured for observations of the Crab Nebula to within $\sim 10\%$. Most of the differences between the model curve and observed data can be attributed to scattering of the optical axis orientations of the four quadrants within a telescope.

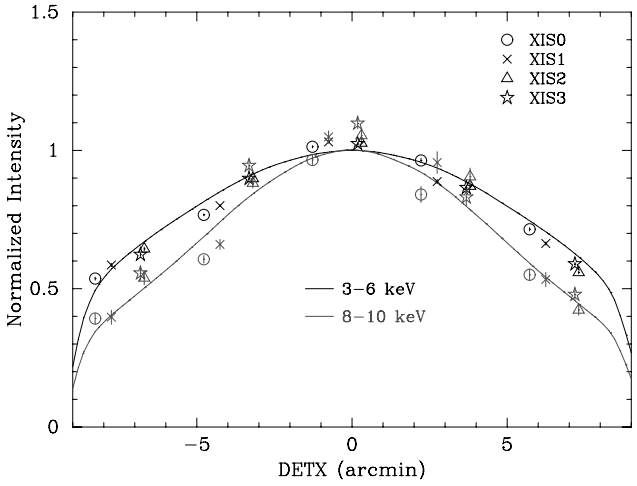

Figure 3.7 Vignetting of the four XRT-I modules using the data of the Crab Nebula taken during 2005 August 22–27 in the two energy bands 3–6 keV and 8–10 keV.

3.1.3 X-ray Imaging Spectrometer (XIS)

Overview of XIS

The X-ray Imaging Spectrometer (XIS) consists of four X-ray cameras, each combined with a single X-ray Telescope (XRT). These employ X-ray sensitive Si charge-coupled devices (CCDs) similarly to those used in the ASCA SIS, Chandra ACIS, XMM-Newton EPIC, and Swift XRT. Figure 3.8 is a photograph of one of the XIS sensor and Figure 3.9 is a cross section of it. In the photon counting mode, X-ray CCD detectors have imaging-spectroscopic capability. In each pixel of a CCD array, an incident X-ray photon is converted into a charge cloud with a total charge proportional to the energy of the absorbed X-ray. The charge is then shifted from one pixel to the next toward the gate of an output transistor by applying a time-varying electrical potential. This results in a voltage level (often referred to as "pulse height") proportional to the energy of the X-ray photon.

Figure 3.8 A photograph of one of the XIS sensor.

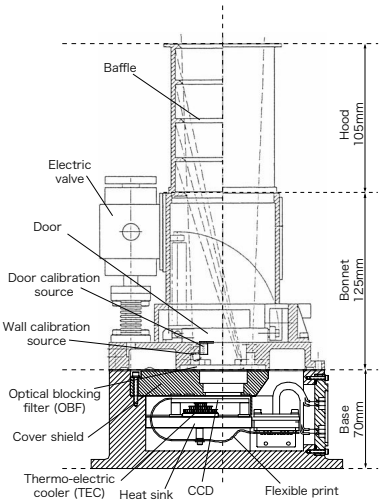

Figure 3.9 Cross section of the XIS sensor.

Each CCD camera has a single CCD chip with 1024 × 1024 pixels, and covers a 18 arcmin ×18 arcmin region on the sky. Each pixel is a 24 μm square, and the size of the CCD chip is 25 mm × 25 mm. One unit of XIS is equipped with a back-side illuminated CCD chip, while the rest contain a front-side illuminated CCD each. The XIS is developed at MIT, Kyoto Univ., Osaka Univ., and ISAS.

Figure 3.10 provides a schematic view of the XIS system. The Analog Electronics (AE) drive the CCD and processes its data. Charge clouds produced in the exposure area in the CCD are transferred to the Frame Store Area (FSA) after the exposure according to the clocks supplied by the AE. The AE reads out data stored in the FSA sequentially, amplifies the data, and performs the analog-to-digital conversion. The AE outputs the digital data into the memory named Pixel RAM in the Pixel Processing Units (PPU). Subsequent data processing is done by accessing the Pixel RAM. To minimize the thermal noise, the sensors need to be kept at ~ -90°C during observations. This is accomplished by thermo-electric coolers (TECs), controlled by TEC Control Electronics, or TCE. The AE and TCE are located in the same housing, and together, they are called the AE/TCE. Suzaku has two AE/TCEs. AE/TCE01 is used for XIS0 and 1, and AE/TCE23 is used for XIS2 and 3. The digital electronics system for the XIS consists of two PPUs and one Main Processing Unit (MPU); PPU01 is associated with AE/TCE01, and PPU23 is associated with AE/TCE23. The PPUs access the raw CCD data in the Pixel RAM, carry out event detection, and send event data to the MPU. The MPU edits and packets the event data, and sends them to the satellite's main digital processor.

To reduce contamination of the X-ray signal by optical and UV light, each XIS has an Optical Blocking Filter (OBF) located in front of it. The OBF is made of polyimide with a thickness of 1000 Å, coated with a total of 1200 Åof aluminum (400 Åon one side and 800 Åon the other side). To facilitate the in-flight calibration of the XISs, each CCD sensor has two ^{55}Fe calibration sources. These sources are located on the side wall of the housing and are collimated in order to illuminate

two corners of the CCDs. They can easily be seen in two corners of each CCD. A small number of these X-rays scatter onto the entire CCD.

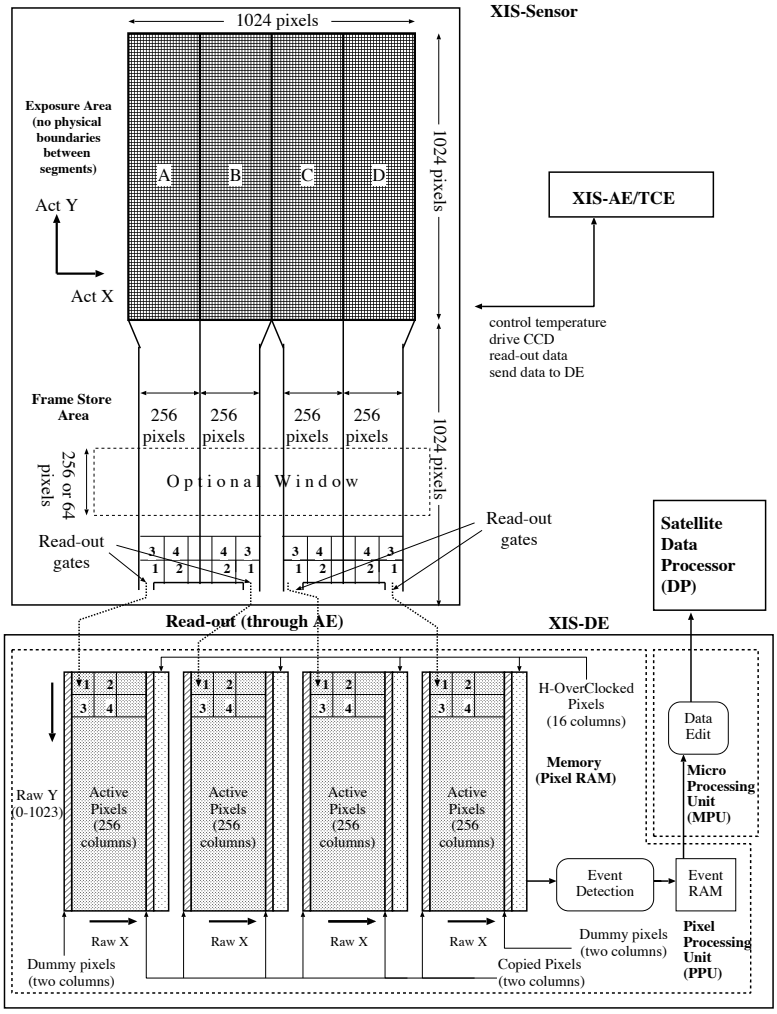

Figure 3.10 Schematic view of the XIS system. Each XIS consists of a single CCD chip with 1024×1024 X-ray sensitive cells, each 24μm square.

Energy Gain and Resolution

Pulse hight distribution function for a monochromatic X-ray line can be represented by a Gaussian-like peak and low energy tail component. Energy resolution for OI Kα line at 0.525 keV is about 50 eV (FWHM) for BI and 40 eV for FI (Koyama et al., 2007). The fraction of the low energy tail component of Suzaku XIS is very small in comparison with other X-ray CCDs used in X-ray satellite mission. Figure 3.11 shows energy spectra (pulse height distribution) for a monochromatic X-ray line emission at $E = 0.5$ keV, in comparison with X-ray CCDs on-board XMM-Newton. Clear peaks are shown by Suzaku FI/BI CCDs. Actual energy spectra of a SNR 1E0102-72 is shown in Figure 3.12. Kα lines of OVII (0.57 keV) and OVII (0.65 keV) are clearly resolved with excellent energy resolution. Thus Suzaku is the most suitable to study diffuse hot

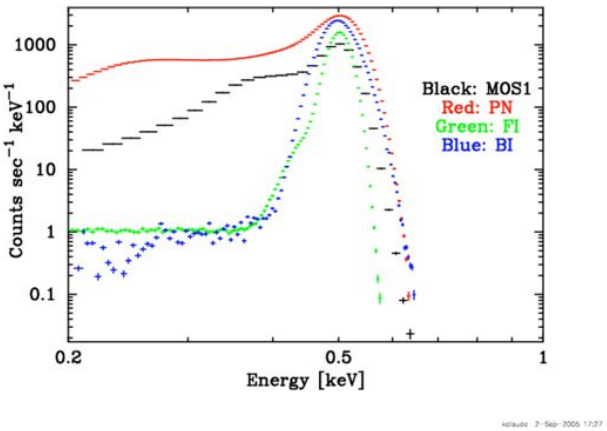

Figure 3.11 Energy spectra for monochromatic line by Suzaku FI/BI sensors and PN and MOS1 CCD onboard XMM-Newton.

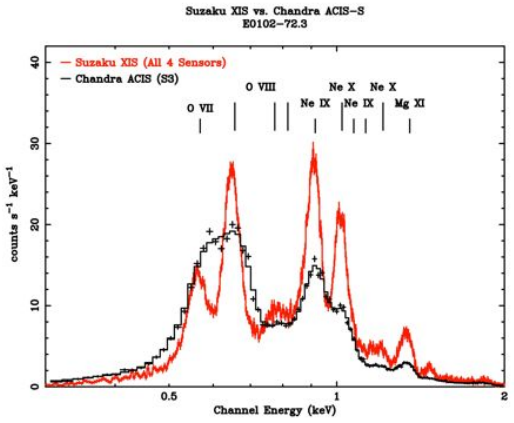

Figure 3.12 Energy spectra of SNR 1E0102-72 by a sum of 4 XIS of Suzaku and S3 CCD onboard Chandra. The OVII and OVIII lines are clearly resolved by Suzaku.

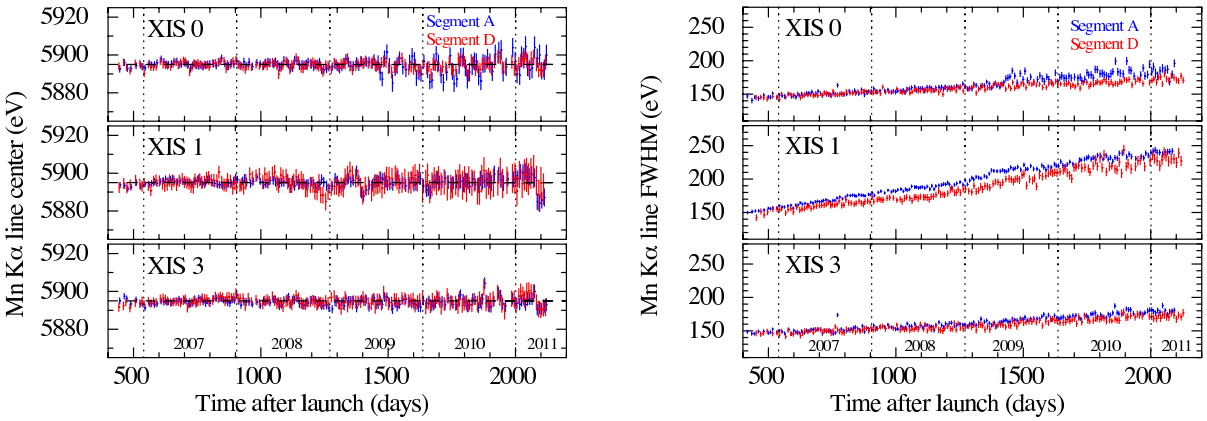

Figure 3.13 Energy gain (left panel) and resolution (right one) at 5.9 keV for the Normal mode XISs using the ^{55}Fe calibration source on-board Suzaku.

plasma which can be characterized by emission lines.

The Normal mode without option is the best calibrated mode of the XIS. The CTI is measured using observations of the Perseus Cluster (all segments, hard band), SNR 1E0102-72 (segments B and C, soft band), and the ^{55}Fe calibration sources (segments A and D, hard band). Fig. 7.8 and 7.9, respectively, show the gain and energy resolution in the hard band using the ^{55}Fe calibration sources, while Fig. 7.10 and 7.11, respectively, show the gain and energy resolution in the soft band using the E0102-72 observations.

Spaced-Row Charge Injection

X-ray CCD devices are subject to degradation in orbit. One of the outcomes is an increase of charge traps under the constant irradiation by cosmic rays in the space environment. This results in an increase of the charge transfer inefficiency (CTI), which leads to a degradation of the energy

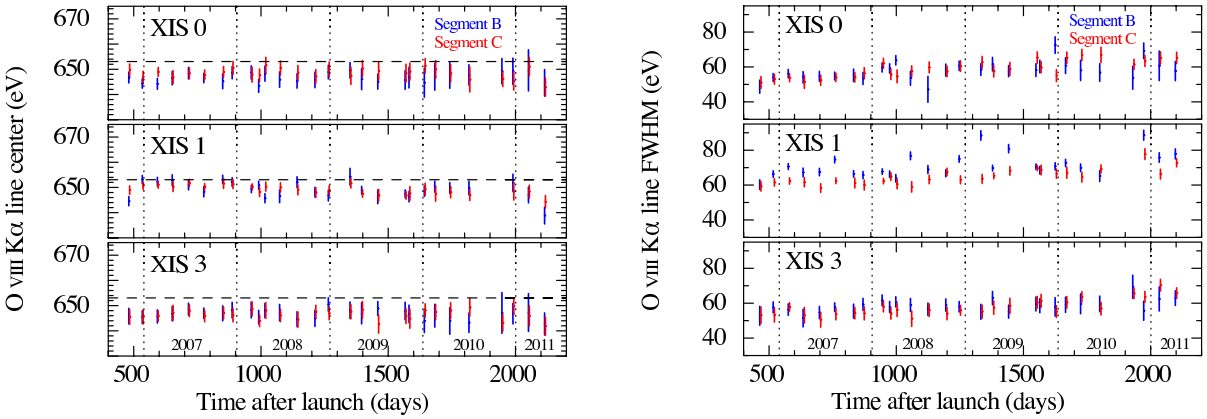

Figure 3.14 Energy gain (left panel) and resolution (right one) at 0.65 keV for the Normal mode XISs using the SNR E0102-72.

resolution. The SCI technique was put into routine operation in the middle of 2006 and has brought a drastic improvement. At the start of SCI operations, an amount of charges equal to the amount produced by a 6 keV X-ray photon ("6 keV equivalent") was injected for the FI devices and a smaller amount ("2 keV equivalent") for the BI device. The smaller amount for XIS1 was chosen because of the expected, SCI-related increase of noise in the soft spectral band, at which the BI device has an advantage over the FI device.

Quantum Efficiency

The quantum efficiency below ∼2 keV has been decreasing since launch due to accumulation of contaminating material on the optical blocking filter (OBF) of each sensor. The OBF is cooler than other parts of the satellite, thus is prone to contamination. The contaminant consists of several different materials with time-varying composition. The chemical composition is modeled phenomenologically with time-varying columns of H, C, and O. This requires sufficient photons between the CI and OI K edges at 0.28 and 0.53keV, respectively.

Figure 3.15 shows the evolution of the thickness derived from the E0102-72 observations. The thickness increased rapidly after launch for one year and continued to increase at a moderate pace thereafter.

Non X-ray Background

All Suzaku XISs have low backgrounds, due to a combination of Suzaku's orbit and the instrumental design. The large effective area at the Fe K line band (comparable to the XMM-Newton PN) combined with this low background makes Suzaku a powerful tool for investigating high energy sources. The background originates from the cosmic X-ray background (CXB) combined with charged particles (the non-X-ray background or NXB). Currently, flickering pixels are a negligible component of the background. When observing the dark Earth (i.e., the NXB), the background rate in the 0.4–12 keV band is 0.1–0.2 counts s^{-1} in the FI CCDs and 0.3–0.6 counts s^{-1} in the BI CCD. Figure 3.16 shows the NXB spectra for each sensor. There are also fluorescence features

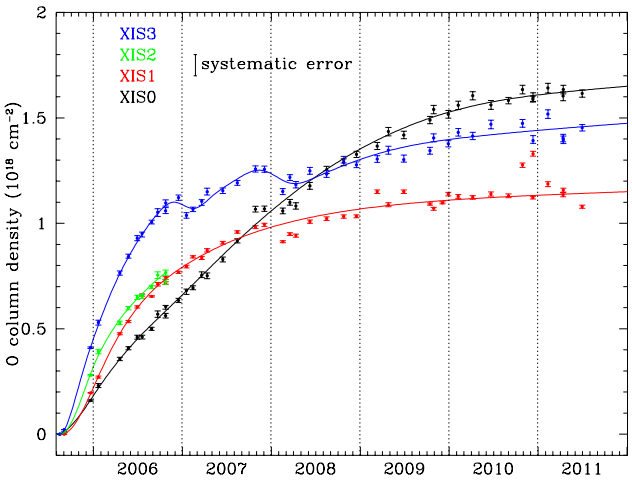

Figure 3.15 Time dependence of the contamination thickness at the XIS nominal position derived from the E0102-72 observations.

arising from the calibration sources as well as material in the XIS and XRTs. The Mn lines are due to scattered X-rays from the calibration sources. The other lines are fluorescent lines from the material used for the sensor. Table 3.3 shows the current best estimates for the strength of these emission features.

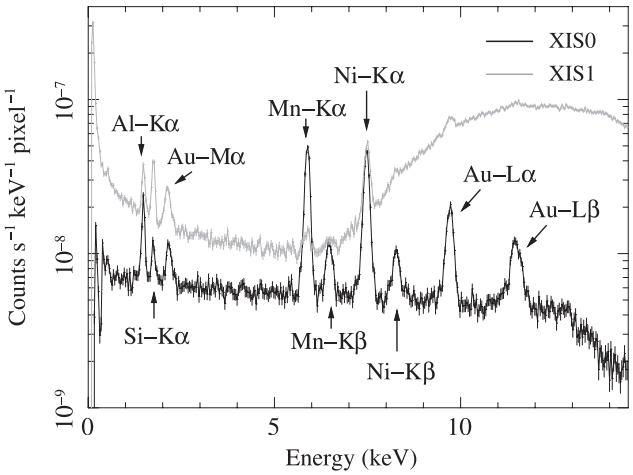

Figure 3.16 Spectra of the NXB in the XIS0 (black) and the XIS1 (gray).

Table 3.3 Error Budgets of Scientific Instrument Calibrations.

Line	Energy	XIS0	XIS1	XIS2	XIS3
	keV	10^{-9} cps/pix	10^{-9} cps/pix	10^{-9} cps/pix	10^{-9} cps/pix
Al Kα	1.486	1.45 ± 0.11	1.84 ± 0.14	1.41 ± 0.10	1.41 ± 0.10
Si Kα	1.740	0.479 ± 0.081	2.27 ± 0.15	0.476 ± 0.080	0.497 ± 0.082
Au Mα	2.123	0.63 ± 0.093	1.10 ± 0.13	0.776 ± 0.097	0.619 ± 0.092
Mn Kα	5.895	6.92 ± 0.19	0.43 ± 0.14	1.19 ± 0.13	0.76 ± 0.11
Mn Kβ	6.490	1.10 ± 0.11	0.26 ± 0.13	0.40 ± 0.11	0.253 ± 0.094
Ni Kα	7.470	7.12 ± 0.19	7.06 ± 0.37	8.01 ± 0.20	7.50 ± 0.20
Ni Kβ	8.265	0.96 ± 0.10	0.75 ± 0.22	1.16 ± 0.11	1.18 ± 0.11
Au Lα	9.671	3.42 ± 0.15	4.15 ± 0.49	3.45 ± 0.15	3.30 ± 0.15
Au Lβ	11.51	2.04 ± 0.14	1.93 ± 0.48	1.97 ± 0.14	1.83 ± 0.14

3.2 Solar Wind Monitoring Satellites

3.2.1 ACE Satellite

The Advanced Composition Explorer (ACE) is an Explorer mission that was managed by the Office of Space Science Mission and Payload Development Division of the NASA/GSFC. ACE launched on August 25th 1997, from the Kennedy Space Center in Florida. ACE orbits the L1 libration point which is a point of Earth-Sun gravitational equilibrium about 1.5 million km from Earth and 148.5 million km from the Sun.

The Solar Wind Electron, Proton, and Alpha Monitor (SWEPAM) measures the solar wind plasma electron and ion fluxes (rates of particle flow) as functions of direction and energy. That is designed to measure the 3D characteristics of solar wind and suprathermal electrons in $1 - 900$ eV and ions in $0.26 - 36$ keV. These data provide detailed knowledge of the solar wind conditions and internal state every minute.

The Solar Wind Ion Composition Spectrometer (SWICS) and the Solar Wind Ion Mass Spectrometer (SWIMS) on ACE are instruments optimized for measurements of the chemical and isotopic composition of solar and interstellar matter. SWICS determines uniquely the chemical and ionic-charge composition of the solar wind, the temperatures and mean speeds of all major solar-wind ions, from H through Fe, at all solar wind speeds above 300 km/s (protons) and 170 km/s (Fe^{+16}), and resolves H and He isotopes of both solar and interstellar sources. SWICS measures the distribution functions of both the interstellar cloud and dust cloud pickup ions up to energies of 100 keV/e. SWIMS measures the chemical and isotopic and charge state composition of the solar wind for every element between He and Ni. Each of the two instruments uses electrostatic analysis followed by a time-of-flight and, as required, an energy measurement.

3.2.2 WIND Satellite

WIND satellite was launched on November 1, 1994 and is the first of two NASA spacecraft in the Global Geospace Science initiative and part of the International Solar Terrestrial Physics Project. WIND also orbits the Lagrangian 1 point. Wind carries an array of scientific instruments for measuring the charged particles and electric and magnetic fields that characterize the interplanetary medium, solar wind and a plasma environment. WIND provides nearly continuous monitoring of the solar wind conditions near Earth. In the WIND data, we mainly used Solar Wind Experiment (SWE) data, which provides the high time resolution 3 dimensional velocity distributions of the ion component of the solar wind, for ions with energies ranging from 200 eV to 8.0 keV.

4 Common Methods of Data Reduction and Spectral Analysis

In the next three chapters, we always use Suzaku XIS1 (back illuminated CCD that achieves high sensitivity under 1 keV) data and try to estimate the intensities of emission line from highly ionized oxygen (OVII Kα at 0.57 keV and OVIII Lyα at 0.65 keV) from spectral fitting. Some data reduction procedures and analysis methods are common. We prospectively describe these processes in this chapter.

4.1 Data reduction

4.1.1 Removal of Point Sources

To investigate the emission from diffuse plasma emission, point sources are removed. Identification of point sources are basically done by using the XAssist catalog. XAssist catalog contains point sources whose fluxes are above $\sim 1.0 \times 10^{-15}$ erg cm^{-2} s^{-1} in 0.3–8.0 keV range, based on Chandra, XMM-Newton and ROSAT observations (Ptak & Griffiths 2003).

4.1.2 Removal of Short Term X-ray Emissivity Variation by Geocoronal SWCX

A time scale of the variation of geocoronal SWCX (G-SWCX) is considered to be about tens of ksec to a few days (Snowden et al. 2004, Fujimoto et al. 2007). The intensity of lines induced by G-SWCX depends on the product of the neutral density in the atmosphere and solar wind ion flux. A typical scale hight of the geocoronal neutral is $\sim 8.2\,R_{\rm E}$ from Earth's surface (Østgaard et al. 2003), and the penetration depth of solar wind ions to the atmosphere is determined by the interplanetary plasma condition (Yoshino et al. 2009). Here we explain the specifics how to determine the data reduction criteria.

First, we checked the solar wind data at 1 AU available at OMNI database[*1] for the solar wind proton, and ACE/SWICS-SWIMS[*2] for the solar wind heavy ions, respectively. The data of ACE/SWICS-SWIMS were only used when the quality flags of solar wind parameters were equal to 0 (meaning "Good quality"). In these observation intervals, there were some lack of ACE Level 2 data, and we compensated the solar wind proton data with WIND.

[*1] http://omniweb.gsfc.nasa.gov/index.html
[*2] http://www.srl.caltech.edu/ACE/ASC/level2/lvl2DATA_SWICS-SWIMS.html

4.1.3 Removal of the Neutral Scattering OI Line.

Solar X-ray photons scattered with the neutral oxygen in Earth's atmosphere create the OI Kα emission (centroids are $E_{O_2} = 525$ eV and $E_O = 540$ eV). We checked the contamination of oxygen emission to OVII emission. In accordance with the previous studies (Smith et al. 2007, Miller et al. 2008, and Yoshino et al. 2009), we calculated the $O+O_2$ column density of sunlit atmosphere in the Suzaku LOS using the Normal MSISE–00 model 2001[*3] (Hedin 1991).

4.2 Spectral Analysis

4.2.1 Response File

We created the Redistribution Matrix File (RMF) for conversion from energy spectrum to pulse invariant (PI), and Auxiliary Response File (ARF that describes energy dependence of X-ray detection efficiency) for the spectral fitting by using the Suzaku FTOOLS software **xisrmfgen** ver.2009–02–28 and **xissimarfgen** ver.2010-11-05, respectively (Ishisaki et al. 2007). Emission source of the ARF file is assumed to an uniform sky with radius of $20'$ that is larger than the Suzaku FOV ($17'.8 \times 17'.8$ square).

4.2.2 Background

Non X-ray Background (NXB) are constructed by using the software **xisnxbgen** ver.2008–03–08 (Tawa et al. 2008). We checked count rates of NXB spectra above 12 keV where the XRT does not reflect X-ray photons. The count rates of each observation above 12 keV were consistent with that of the NXB in 10 %. If we scaled the normalization of each NXB spectrum and equalized the count rate above 12 keV among the observations, we confirmed that influences of this scaling were smaller than statistical errors in the spectral fitting.

4.2.3 Emission Model of the Soft Diffuse X-ray Background

The purpose of the later spectral analysis is to obtain the OVII Kα (0.57 keV) and OVIII Lyα (0.65 keV) line intensities precisely. However, there are some contributions at these line energies from the other diffuse emission components that cannot be resolved with CCD resolution. Therefore, we need to estimate this contribution by assuming spectral models.

The diffuse emission model consists of three components

1. Cosmic X-ray Background expressed by double broken power laws absorbed by Galactic neutrals
2. Emission for a CIE (collisional ionization equillibrium) plasma. This component represents emission for Galactic halo absorbed by Galactic neutrals (Kuntz & Snowden 2000).

[*3] http://ccmc.gsfc.nasa.gov/modelweb/atmos/nrlmsise00.html

3. Emission for a CIE plasma with a temperature of $kT \sim 0.1$ keV without galactic absorption. This component is considered to represent the H-SWCX or blend of H-SWCX and LB emission. (Yoshino et al. 2009, Henly & Shelton 2010).

The emission of CXB that is dominant component above 1 keV is represented by double broken power laws. The photon indices of them are $\Gamma = 1.96$ and $\Gamma = 1.54$ below the folding energy at 1.2 keV and $\Gamma = 1.40$ above it. Following to Smith et al. (2007), we fixed the normalization of the broken power law component with photon index of $\Gamma = 1.54$ as 5.7 photons s^{-1} cm^{-2} keV^{-1} sr^{-1} at 1 keV.

Though the H-SWCX induces non-thermal emission, we treated the LB+SWCX blend as a single CIE plasma in this analysis following many previous works (Smith et al. 2007, Yoshino et al. 2009, and Henly & Shelton 2010). Both spectra of the LB and SWCX show similar shape that consists of many transition lines and contains strong OVII emission (Figure 4.1). The two spectra cannot be distinguished from each other. The temperature of LB+SWCX blend was fixed at the typical temperature $kT = 0.099$ keV ($\sim 1.15 \times 10^6$ K), derived from the observations of local blank field region where the contribution of the halo were almost negligible due to the large interstellar absorption (Yoshino et al. 2009, Masui et al. 2009).

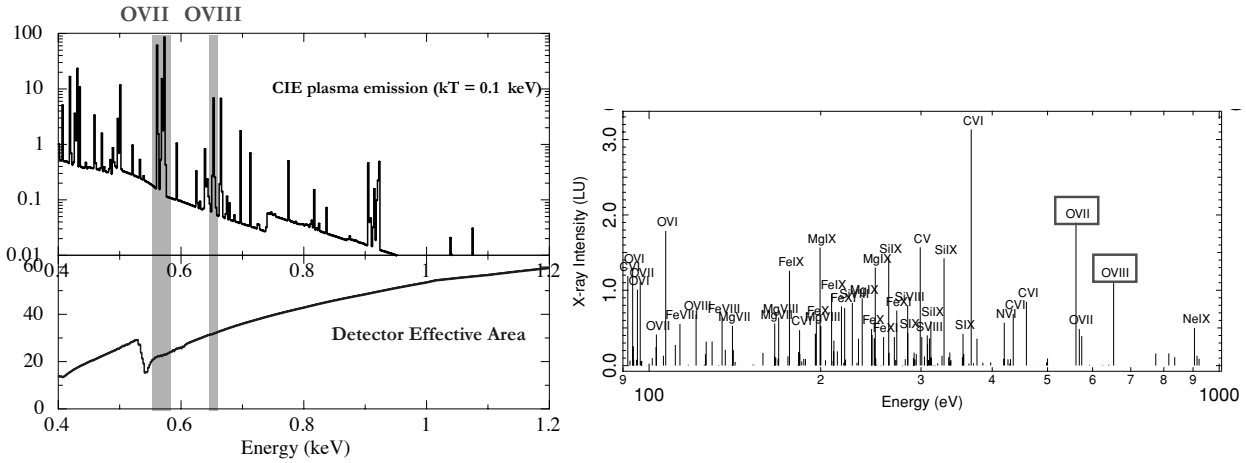

Figure 4.1 Comparison of the typical emission spectra between thin thermal plasma in CIE with temperature of $kT = 0.1$ keV (left) and solar-wind charge exchange (right, referred from Koutroumpa et al. (2009a)). The second raw of left figure shows the detector efficiency of Suzaku XIS1.

For the thin thermal plasma emission, *APEC* model (with AtomDB ver.2.0.1) is applied to estimate both the Galactic halo gas and the LB+SWCX emissions.

4.2.4 Derivation of OVII and OVIII Line Intensities

After determining the model parameters of wide band spectra in §4.2.3, we tried to fit the same spectra again under fixing the halo temperature at the best fit values, and oxygen abundances at zero for both the halo and LB+SWCX, but inserting three gaussian lines at OVII Kα, OVIII Lyα,

and OVII kβ energy. As reported in Yoshino et al. (2009), the intensities of OVIII Lyα emission are weak in the observations we show later and OVIII Kβ emission exists at 666 eV that can not be resolved with OVII Lyα. For this reason, to determine the error range of its energy centroid is hard in the observations. We fixed the centroid of OVII Kα, OVIII Lyα, OVII Kβ at 567 eV averaging the centroids of resonance (574 eV) and forbidden (561 eV) line, 653 eV, and 666 eV respectively. The fraction of the OVII Kβ to OVII Kα was also fixed at 8.3 % that is expected for the SWCX induced emission (Kharchenko et al. 2003). Here we define the intensity of OVII and OVIII emissions as the normalization of two inserted gaussians.

There is an uncertainty of line intensity ratio of OVII Kβ to Kα, because it depends on model (i.e., either thermal emission or SWCX emission). The OVIII intensity is affected by the assumption because OVII K β emission contaminates the OVII Lyα emission. In Yoshino et al. (2009), they estimated OVIII intensity using the OVII Kβ/OVII Kα of 0.04 for CIE plasma at 0.1 keV and 0.08 for SWCX. They also confirmed that the best-fit value of OVIII line intensities are at most 10 % higher and lower for the case of plasma at 0.1 keV and SWCX, respectively, which are within the statistical errors.

5 Long Term Variability of OVII Emission from 2006 to 2011

5.1 Purpose of Analysis

The purpose of this chapter is to investigate the variabilities of the heliospheric SWCX (H-SWCX) induced OVII emission on long time scales, which may be related to the long term solar cycle of $\sim$ 11 years. To avoid the direction dependence of H-SWCX, we must use a set of observations toward the same direction. We also need to note that parallax also produces the variation, since the distributions of interstellar neutral in the heliosphere are quite anisotropic (Pepino et al. 2004). We thus need to use those observations made at the same period of time in a year. In addition, we need to remove the time periods when the OVII intensity was enhanced on time scales about tens of ks, which we considered the enhancement by geocoronal SWCX (G-SWCX).

We analyzed OVII and OVIII line intensities toward Lockman Hole (relatively in high ecliptic latitude area at $\beta = 45.2°$) with Suzaku annually observed from 2006 to 2011. This interval covers about half Solar Cycle headed from the solar minimum phase at the end of Cycle 23 to the maximum of Cycle 24. This is the first time to compare the energy spectra toward blank field region under fixing both the line of sight and observation configuration strictly. If the significant differences of the oxygen line intensity among the observations still exist, these differences will indicate the long term variability of the H-SWCX induced emission related to the 11-year Solar Cycle.

5.2 Observations

Suzaku annually observes Lockman Hole direction $(\alpha, \delta)/(\ell, b) = (162°.94, 57°.25)/(149°.71, 53°.21)$ from 2006 as a calibration target for Hard X-ray Detector (HXD). This field is characterized by very low hydrogen column density; $N_{\rm H} = 5.6 \times 10^{19}$ cm^{-2} (Dickey & Lockman 1990, and Hasinger et al. 1993), or 5.8×10^{19} cm^{-2} (Kalberla et al. 2005). Details of the observations are summarized in Table 5.1. Though all observations were carried out in the same pointing direction within $2'$, the roll angles[*1] are different by at most $\sim 40°$ (the field of views differ $\sim 20\%$) among them. We use the data of X-ray Imaging Spectrometer (XIS) on–board Suzaku (Koyama et al. 2007) ver.2.0, 2.0, 2.2, 2.4, 2.5, and 2.5 processed for LH06, LH07, LH08, LH09, LH10, and LH11 respectively. Their energy gain corrections were performed by using **xispi** with the latest makepi file `ae_xi1_makepi_20110621.fits` in CALDB. All XIS data sets were observed with the normal clocking and the 3×3 or 5×5 editing mode. The Spaced–raw Charge Injection (SCI) was adopted

[*1] Roll angle is defined as a rotating angle from $\delta = 0°$ in a counterclockwise direction.

except LH06 observation. The observation LH06 was also analyzed in Yoshino et al. (2009), and our result was consistent with them (see the details below).

Table 5.1 Log of the Suzaku Lockman Hole observations.

ID	Start / End date (UT)	Exposure (ks)		Screening		Pointing		Roll angle
	YYMMDD hh:mm:ss	total*	screened†	1‡	2§	R. A.	Dec.	
LH06	060517 17:44:06 / 060519 19:03:18	80.4	32.5	✓		162°.937	57°.256	281°.872
LH07	070503 23:12:08 / 070506 02:00:19	96.1	56.7		✓	162°.937	57°.258	319°.511
LH08	080518 11:07:29 / 080520 01:16:14	83.4	58.4			162°.937	57°.255	281°.530
LH09	090612 07:17:40 / 090614 01:31:21	92.8	63.8			162°.938	57°.255	281°.530
LH10	100611 07:29:06 / 100613 01:59:22	78.0	50.0	✓		162°.937	57°.251	279°.887
LH11	110504 17:46:34 / 110505 18:25:20	42.3	19.4		✓	162°.920	57°.251	305°.984

* Total exposure of the XIS1 after the standard screening.

† Screened exposure extracted when COR2 > 8 GV c^{-1} and screened by the criteria 1 and 2 (next 2 colums).

‡ Effect of the geocoronal SWCX induced emission was removed (see §5.3.1).

§ Contamination of the neutral OI Kα emission was removed (see §5.3.2).

5.3 Data Screening

We start from the XIS1 cleaned event files that are processed with standard data screening criteria. To avoid high energy particles penetration due to the low Earth's magnetic field, we extracted the data when Cut Off Rigidity (COR2) was larger than 8 GV c^{-1}. Two bright sources whose flux was larger than 1.0×10^{-14} erg cm^{-2} s^{-1} in 0.5 – 2.0 keV were removed by circles with diameters $3'.0$ and $4'.0$ centered at ($\alpha = 162°.811,\ \delta = 57°.271$) and ($163°.005,\ 57°.178$).

After the data were screened with the above criteria, we further removed the interval when G-SWCX induced emission and neutral OI Kα one in the Earth atmosphere were enhanced (screening procedures were described in §5.3.1 and §5.3.2). Table 5.1 shows the exposures of total cleaned events and screened ones, and what screening was applied in each observation.

5.3.1 Removal of Short Term X-ray Emissivity Variation by Geocoronal SWCX

During LH07, LH09, and LH11, proton fluxes, expressed as a product of the density and the velocity, were always less than 4.0×10^8 cm^{-2}s^{-1}. According to the solar wind monitoring at L1, Both LH07 and LH09 were settled in the slow solar wind condition, and LH11 be in the temporary fast one (typical properties of the slow/fast solar winds are summarized in Koutroumpa et al. (2006), Table 1). They were not screened by solar wind flux.

In LH06 and LH10, both proton and ion fluxes were enhanced by passage of the corotating interaction region (CIR) around the Earth, where slow solar wind is compressed by fast one. We compared the OVII line intensities between the CIR passage and the rest of the observation interval.

OVII estimated from the spectral fitting (details are described in the next section) were $5.6^{+1.1}_{-1.1}$ (CIR passage) / $2.6^{+0.8}_{-0.7}$ (the rest) LU in LH06, and 7.7 ± 1.3 (CIR passage) / 6.1 ± 1.1 (the rest) LU in LH10, respectively. We used the data when the solar wind absolutely settled in slow or fast condition (after 90 ks from the observation beginning of LH06, and before 110 ks from that of LH10).

Though spiky increase of the proton density was presented between 60 ks to 100 ks from the beginning of LH08, there was no enhancement in both of O^{+7} flux and OVII. Estimated OVII intensities are $2.7^{+1.5}_{-1.3}$ (60 ks to 100 ks) / $3.0^{+1.0}_{-0.9}$ (the rest) LU respectively. We did not screened the LH08 by solar wind flux.

Second, we calculated the structure of the geomagnetic field toward Suzaku line of sight (LOS) using the Geopack 2008 (Tsyganenko & Sitnov 2005). In all observations, distance of the Earth–center to the magnetopause (ETM) varied from 1.5 to 15.0 $R_{\rm E}$. However, the effect of low ETM distance to the energy spectrum was only confirmed during the passage of CIR in LH06 that had been already removed. In this analysis, we did not screen the data based on the ETM distance.

5.3.2 Removal of the Neutral OI Line.

We checked the mixing of neutral oxygen lines to OVII line. Solar X-ray photons scattered with the neutral oxygen in Earth's atmosphere create the OI Kα line emission (centroids are $E_{\rm O_2} = 525$ eV and $E_{\rm O} = 540$ eV). In accordance with the previous studies (Smith et al. 2007, Miller et al. 2008, and Yoshino et al. 2009), we calculated the distributions of the neutral in Earth's atmosphere using the Normal MSISE–00 model 2001*2 (Hedin 1991).

The count rate in 0.5–0.6 keV increased with the neutral column density only in LH07. We decided to use the X-ray events of LH07 when the neutral oxygen column density was less than 1.0×10^{14} cm^{-2} for observation intervals at day Earth side, or 1.0×10^{15} cm^{-2} in the night. The spectral differences in 0.5–0.6 keV band were also seen in LH11 when the satellite revolved in the day or night Earth side. It is thought to be an effect of the neutral scattering occurred in the atmosphere very close to Suzaku. We only used the LH11 data for spectral analysis when Suzaku revolved in the night Earth side.

The GOES C4.2 class X-ray flare came to the Earth at May 5th 11:00 (UT) in LH07 and the M2.0 class one did at June 12th 9:00 in LH10. However, there was no significant OI Kα enhancement on both the Suzaku light curve and the energy spectrum, so we used data during the flare arrivals.

*2 http://ccmc.gsfc.nasa.gov/modelweb/atmos/nrlmsise00.html

5.4 Spectral Analysis

Response and background files used for the spectral fitting were created by the procedure in §4.2.1 and §4.2.2.

5.4.1 Spectral Fitting in 0.4–5.5 keV Band

The purpose of this spectral analysis is also to obtain the OVII Kα (0.57 keV) and OVIII Lyα (0.65 keV) line intensities, and scrutinize the variability of them among different observations.

To estimate the oxygen line intensities, we first tried to fit the spectra using broad energy range from 0.4 to 5.5 keV. Figure 5.1 shows the Lockman Hole spectra with their best fit double broken power laws + Galactic halo + (LB + SWCX) models explained in §4.2.3. All six spectra are fitted simultaneously. First, we tried to fit the spectra with the normalization of CXB same among all observations, because the pointing directions of them were almost same. The result showed that 90 % confidence ranges of the temperature and normalization of the halo were overlapped among all. Therefore, we determined to take the same value of the halo parameters among them. The best fit values of them are summarized in the upper 6 rows in Table 5.2. Reduced χ^2 is 0.999 for 636 d.o.f., and all spectrum was well reproduced by this model.

5.4.2 Derivation of OVII and OVIII Line Intensities

We fitted the same spectra again to estimate the intensities of OVII and OVIII emission based on the method of §4.2.4. The lower 6 rows in Table 5.2 shows the best fit results with this new model, and here we define the intensity of OVII and OVIII lines as the normalization of two inserted gaussians. According to this fitting result, OVII intensities of the earlier four observations were almost settled within 90 % statistical error range. However, those of LH10 and LH11 are $2-3$ LU (= photons $s^{-1}cm^{-2}sr^{-1}$) brighter than the others. Statistical significances of the OVII intensity variation of LH10 and LH11 with respect to an average of LH06 to LH09 ($= 2.99 \pm 0.38$ LU) are 4.5σ (LH10) and 2.3σ (LH11), respectively.

5.4.3 Systematic Uncertainties of OVII and OVIII Lines

The absolute intensities of OVII and OVIII emission strongly depend on the X-ray detection efficiency and emission model (Yoshino et al. 2009). First, we checked the uncertainty of contaminant thickness on the XIS optical blocking filter. The systematic uncertainty of contaminant thickness is estimated to be $\pm 10\%$ to the nominal value of CALDB files (Suzaku technical description[*3]). We changed the efficiency described in the ARF using the software **xiscontamicalc** version 2010–11–05 according to the thickness uncertainty. These systematic errors are smaller than the 90 % statistical ones in Table 5.2, and we only show the results with the ARF of nominal contamination thickness.

[*3] http://www.astro.isas.jaxa.jp/suzaku/doc/suzaku_td/

If OVII emissions of LH10 and LH11 are equal to the early four observations, the thicknesses must be overestimated 50% at May 2010 and 40% at June 2011 to the nominal values (of the latest CALDB `ae_xi[1-3]_contami_20091201.fits`).

Second, we checked the contribution of the uncertainty of the CXB spectrum below 2 keV to the determination of oxygen line intensities. We tried to use a single power law model with photon index $\Gamma = 1.4$ for the CXB emission instead of double broken power laws. The oxygen lines systematically became $0.3 - 0.4$ LU larger than in the case of using the double broken power laws CXB model. However, differences among them were not dependent to the CXB model.

Table 5.2 Results of spectral fitting with double broken power laws CXB + Galactic halo+ (LB+SWCX) models.

component	CXB	Galactic Halo		LB+SWCX	OVII	OVIII	χ^2/d.o.f.
model	*phabs* (bknpwls†)*	*phabs* (APEC)*		*APEC‡*	*gaussian§*	*gaussian§*	
parameter	norm.	kT	norm.	norm.	norm.	norm.	
unit	‖	keV	♯	♯	**	**	
LH06	4.1 ± 0.2	$0.216^{+0.025}_{-0.029}$	$1.7^{+1.1}_{-0.4}$	$9.1^{+4.0}_{-5.3}$	–	–	635.2/636
LH07				$18.4^{+4.1}_{-5.4}$	–	–	
LH08				$17.4^{+4.3}_{-5.5}$	–	–	
LH09				$14.7^{+4.5}_{-5.6}$	–	–	
LH10				$39.7^{+5.7}_{-6.5}$	–	–	
LH11				$31.8^{+8.4}_{-8.9}$	–	–	
LH06	4.1 ± 0.2	0.216 (fixed)	2.1 ± 0.8	9.0 ± 8.4	2.55 ± 0.74	0.21 (< 0.62)	615.9/625
LH07				20.7 ± 9.7	3.68 ± 0.72	0.61 ± 0.37	
LH08				27.5 ± 10.3	3.03 ± 0.77	0.94 ± 0.41	
LH09				25.0 ± 10.9	2.69 ± 0.80	0.77 ± 0.42	
LH10				60.1 ± 13.7	6.06 ± 1.07	0.86 ± 0.49	
LH11				42.0 ± 22.5	5.28 ± 1.60	0.97 ± 0.76	

* Absorption column density is fixed at $N_{\rm H} = 5.8 \times 10^{19}{\rm cm}^{-2}$ (Kalberla et al. (2005)).

† Normalization of the power law with $\Gamma = 1.54$ is also fixed at 5.7 photons ${\rm s}^{-1}{\rm cm}^{-2}{\rm keV}^{-1}{\rm sr}^{-1}$@1keV.

‡ See details in the text in §5.4.1.

§ See details in the text in §5.4.2.

‖ The unit of the normalization of a power law component is photons ${\rm s}^{-1}{\rm cm}^{-2}{\rm keV}^{-1}{\rm sr}^{-1}$@1keV.

♯ The emission measure integrated over the line of sight, $(1/4\pi)\int n_{\rm e} n_{\rm H} ds$ in the unit of 10^{14} ${\rm cm}^{-5}$ ${\rm sr}^{-1}$.

** The normalization of gaussian component shows the surface brightness whose unit is defined as L.U. (Line Unit) = photons ${\rm s}^{-1}{\rm cm}^{-2}{\rm sr}^{-1}$.

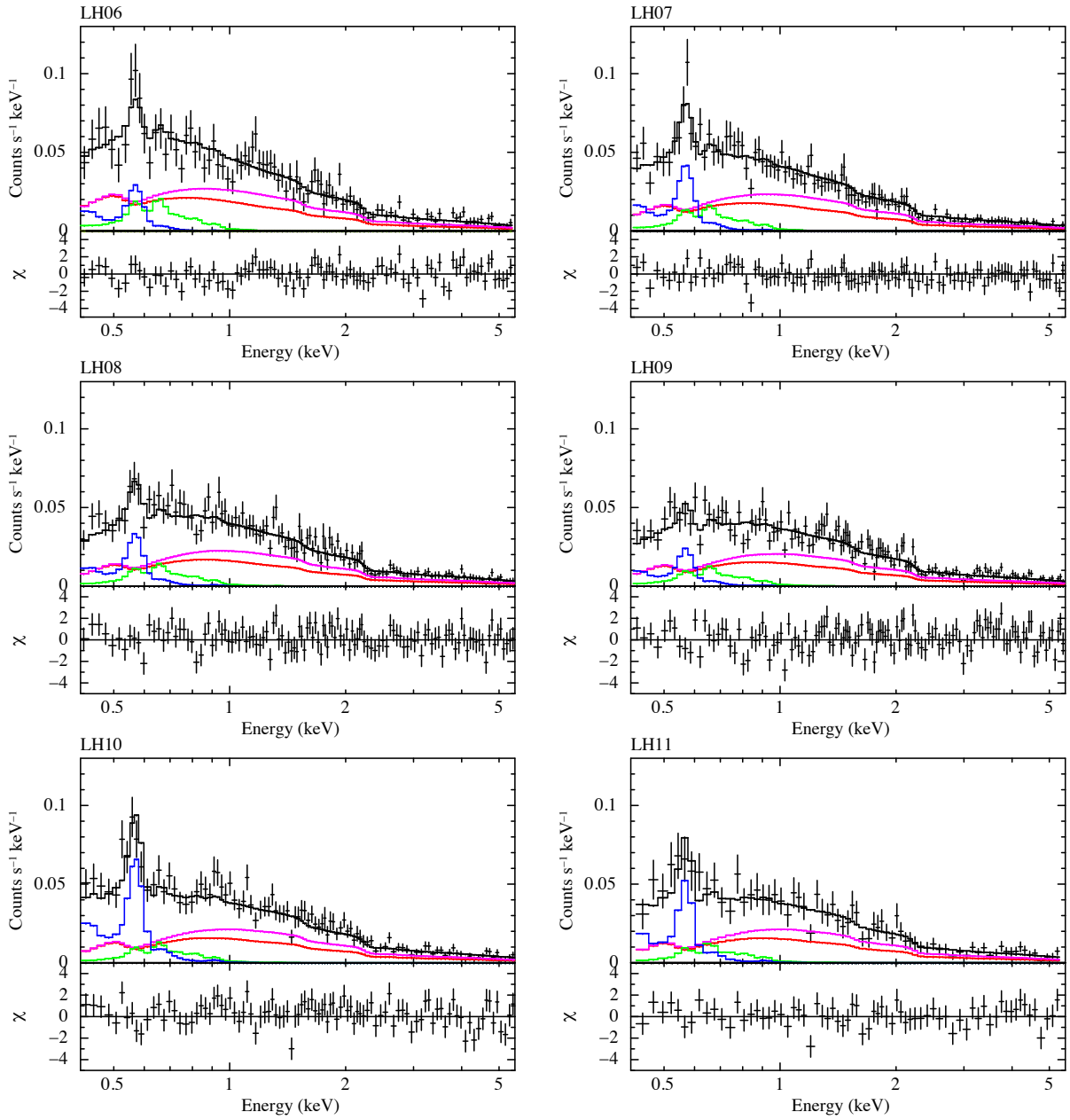

Figure 5.1 0.4 – 5.5 keV Suzaku XIS1 (back illuminated CCD) spectra and best fit emission models of the blank field toward Lockman hole from 2006 to 2011 convolved with the CCD and telescope responses (top panel) and residual of the fit (bottom panel). Black crosses show the observed spectra. Step lines show the models with best fit values; total (black), Galactic halo (green), LB+SWCX (blue), CXB with $\Gamma = 1.54$ (magenta), and CXB with $\Gamma = 1.96$ (red) respectively.

5.5 Discussion

From the results of spectral fitting, we found that OVII intensities toward Lockman Hole were enhanced by $2-3$ LU in 2010 and 2011, compared to that from 2006 to 2009 during which the intensity was consistent to be constant within 90% statistical errors. The variation of OVIII line was not detected significantly over the statistical uncertainties of this analysis.

As we described in Chapter 2, OVII emission is considered to arise from four different origins: hot Galactic halo, LB, G-SWCX, and H-SWCX. The emission from the halo and LB is not time variable on the present observation time scales, and the small difference of the filed of view due to azimuthal rotations (20 %) is not likely to produce the observed variation.

We removed enhancement on times of a few tens of ks as much as possible. We consider that enhancement due to G-SWCX is mostly removed. However, enhancement due to increase of solar wind ion flux near the Earth (~ 0.5 AU scale) is not removed. Thus we next checked the correlation between the OVII intensity and the solar wind flux averaged over the observation period. The result is shown in Figure 5.2. During the four Suzaku observations excluding the first and last ones (LH06 and 11), slow solar wind passed around the Earth. Both the observation LH1 and LH6 were carried out during the fast solar wind condition around the Earth. The ionization states of ions can be considered to be similar for the four observations (LH07 to LH10). Therefore we can consider that the O^{+7} flux is proportional to the proton flux at least for the four observations. Since the typical elapsed time of the observations is two days, and the typical wind speed is ~ 400 km/s, the lack of positive correlation in Figure 5.2 suggests that the OVII variation is not correlated with the average ion flux on ~ 0.5 AU scales.

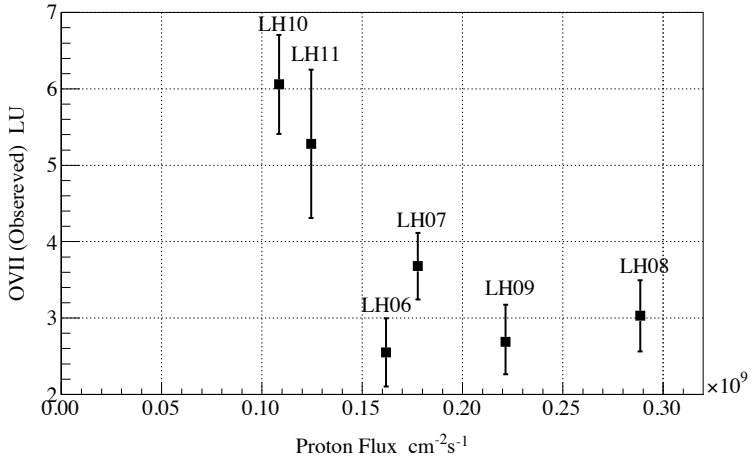

Figure 5.2 Comparison of the OVII line intensities obtained from the spectral fitting in Table 5.2 and solar wind proton flux value. Proton flux was represented by the average of WIND/SWE data during each Suzaku observation.

As we discussed in §5.1, the parallax can produce intensity variation. However, all the observations were made between May 3 and June 13, and we find no correlation between the OVII intensity and

the day of year of the observation. Thus the variation is not due to parallax. We thus consider that the variation is related to variations of the ion flux or the density of neutrals averaged along the line of sight for the length longer than ~ 0.5 AU. A possible explanation for this is the long term variation of the solar wind properties associated with the solar activity. As we described in §5.1, one of the observational differences between the solar maximum and the minimum is distributions of the slow and fast solar wind on the surface of the Sun (McComas et al. 2008). The direction toward Lockman Hole is relatively in high ecliptic latitude area at $\beta = 45.2°$, and hence the variability of the boundary between the slow and fast winds would affect the OVII intensity.

Figure 5.3 shows the time dependences of relative sunspot number (NAOJ, private communication with Prof. S. Tsuneta) representing long term ($\sim$ 11-year) solar cycle together with the present OVII intensities. Based on the sunspot number, the solar minimum of the Cycle 23 was around December 2008, and the Solar Cycle 24 began. Solar activities between northern and southern hemispheres show the different time dependences. The sunspot numbers in southern hemisphere change symmetrically to the solar minimum, and those in 2006 are almost same in 2010 to 2011. On the other hand, the sunspot numbers in northern hemisphere are less than 10 from 2006 to 2010, while they rapidly increase after the minimum and reach 40 in June 2011. The Suzaku line of sight (LOS) points toward the northern hemisphere of the Sun, and here we focus on the solar activity in the northern hemisphere. Figure 5.4 shows the comparison between relative sunspot numbers in northern hemisphere at each Suzaku observation and OVII line intensities. It appears that the enhancement of OVII emission in 2010 is coincided with the rapid increase of sunspot number in the northern hemisphere.

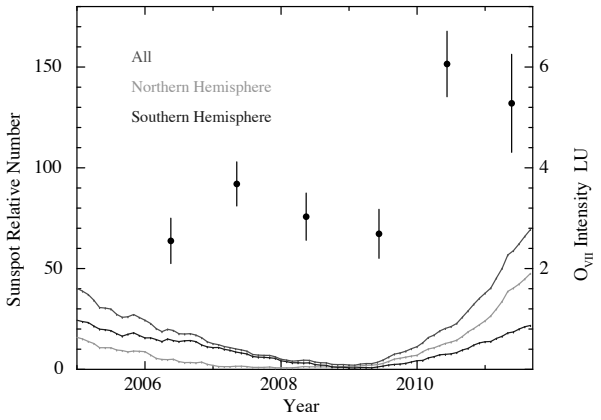

Figure 5.3 Time dependences of the NAOJ relative sunspot numbers (red, green, and blue, left y axis) and Suzaku OVII line intensities (black, right one).

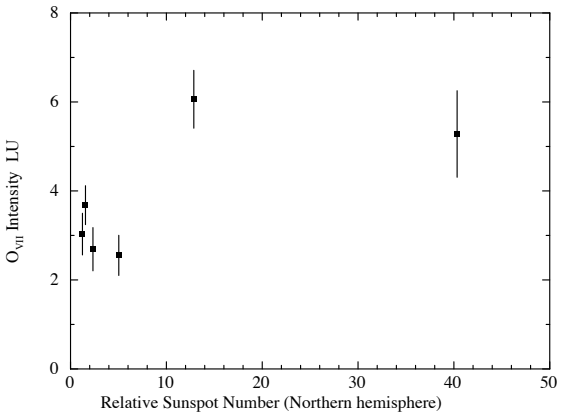

Figure 5.4 Comparison between relative sunspot numbers in northern hemisphere and OVII line intensities.

Figure 5.5 shows the Magnetic concentrations at polar regions observed with Hinode Solar Optical Telescope / Spectropolarimeter (Shiota et al. 2012). In 2008 to 2009, magnetic fields around north and south polar regions are polarized in positive (N, blue points in Figure 5.5) and negative (S, orange points) poles respectively, and the solar magnetic field globally forms dipole structure. This is a typical feature of a coronal holes and fast solar wind flows from polar regions (McComas et

al. 2008). However, the Hinode data (Figure 5.5) indicates that the polarity reversal is about to take place only in the northern polar region. This is seen in the appearance of the mixed (positive and negative) polarity situation in the map of the northern polar region taken in 2011. Such mixed region is not seen in the southern polar region. Magnetic field lines in such mixed polarity region are locally closed near the surface of the Sun, and this is the region from which slow solar wind usually emanates. This situation is very commonly seen near the equatorial region at around the solar maximum (McComas et al. 2008). Remnant magnetic fields from sunspots and active regions are carried latitudinally by the meridional flow or by the turbulent diffusion from low latitude to the polar region whose magnetic polarity is opposite to such magnetic fields transported to the polar region (Dikpati & Charbonneau 1999). The reversal of the polar magnetic fields takes place at around the solar maximum as the result. The polar magnetic fields in the southern polar region is stable at around the minimum as expected, whereas those of the northern polar region appears to start the reversal. This unusual situation may be consistent with the unbalanced lager number of sunspots seen in the northern hemisphere.

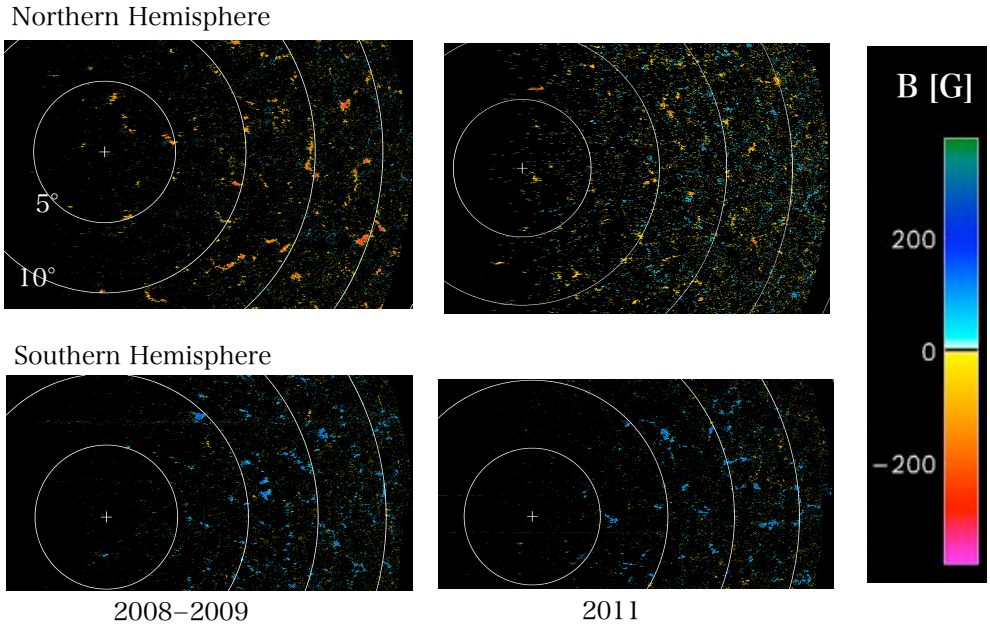

Figure 5.5 Magnetic concentrations at polar regions observed with Hinode (Shiota et al. (2012)).

Figure 5.6 shows the solar wind distribution maps in the Carrington rotation number versus heliographic latitude obtained by the interplanetary scintillation method (STE lab.[*4]). Though the fast wind whose velocity is $>\sim$ 600 km s^{-1} extends in high latitude from 2006 to 2009, slow solar wind ($<\sim$ 400 km s^{-1}) actually spreads throughout the northern hemisphere in 2011. If the slow/fast solar wind boundary is at $|\beta| = 20°$ at solar minimum, the line of sight (LOS) of preset observations crosses the boundary and enters into the fast-wind region at $\sim$ 0.5 AU from the Earth. Beyond that point, the LOS stays in the fast wind region. On the other hand, if we assume the

[*4] http://stsw1.stelab.nagoya-u.ac.jp/ips_data.html

boundary is at $|\beta| = 50°$ at the solar maximum, the LOS is in the slow wind all the way to the outer boundary of the Heliosphere.

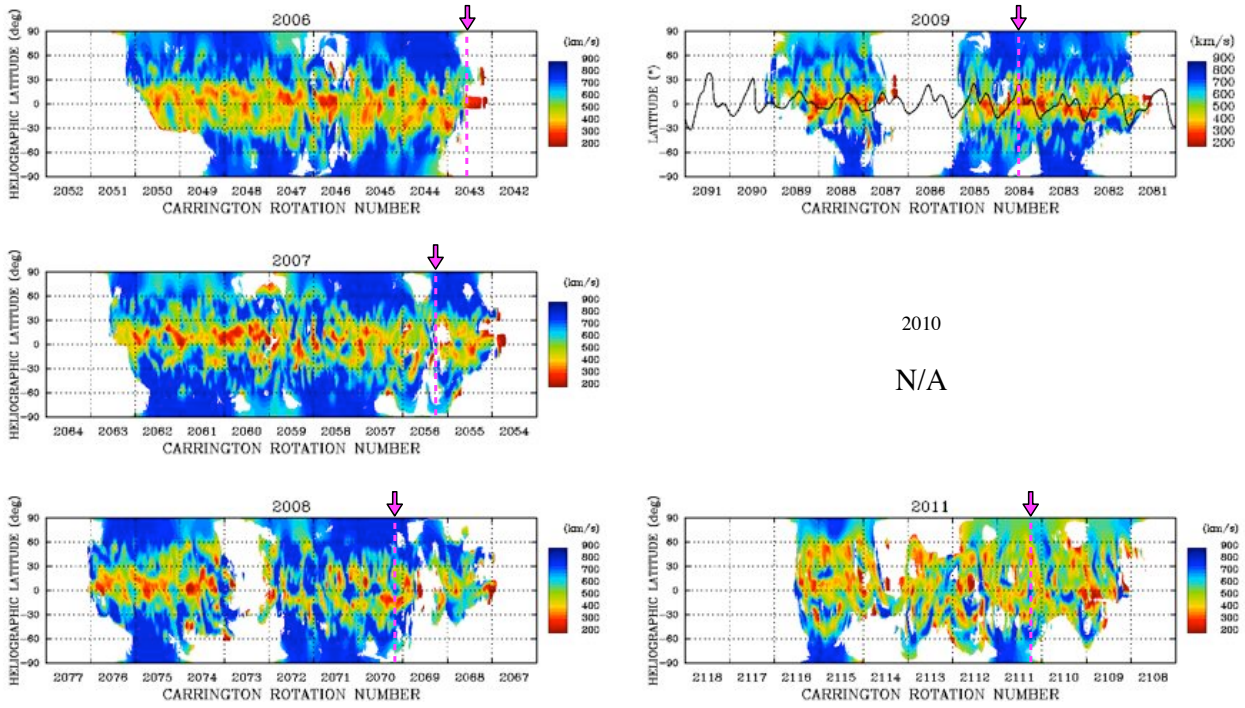

Figure 5.6 Solar wind velocity maps in the Carrington rotation number versus heliographic latitude obtained by the interplanetary scintillation method (STE lab.). The Source surface was assumed to be at 2.5 solar radii. Results in 2010 are not available due to an extensive update of observatories. The vertical magenta lines show the dates of Suzaku observation.

Therefore, the observation results of the OVII intensity, sunspot number, solar wind distribution, and unusual magnetic situation around the northern polar region are consistent with each other. Slow and fast solar wind distributions in the northern interplanetary space are thought to be closer to the solar maximum state at Suzaku observations in 2010 and 2011. Namely, the slow wind reaches much higher latitude in the northern hemisphere.

Next, we estimated the SWCX OVII intensity following the model developed by Koutroumpa et al. (2006). Details of the model are described in Appendix A. This model predicts that the intensity of the H-SWCX induced OVII line is 0.9 LU at solar minimum ($|\beta| = 20°$), and 1.7 LU at solar maximum ($|\beta| > 50°$), respectively. Note that the increase of OVII intensity is smaller than that expected when we just change the beta angle of fast/slow wind boundary, because the density of neutrals decreases due to the strong photoionization by the solar UV photons and charge exchange by the solar wind protons. Thus this model can explain about one third of the observed OVII intensity variations. There are uncertainties in the solar wind parameters, especially in high ecliptic latitude directions. The factor of about three discrepancy may be explained by those uncertainties.

Because solar wind contains ions other than O^{+7}, the SWCX induced X-ray emission should also

contain emission other than OVII. However, those lines were too weak. OVIII emission was positively detected, however the temporal variation was not significantly detected. The upper limit of the intensity variation (0.75 LU) is consistent with the model prediction of the H-SWCX (Koutroumpa et al. 2006).

6 Enhancements of the SWCX induced OVII Emission Associated with the He Focusing Cone.

6.1 Purpose of Analysis

In this chapter, we investigate the enhancement of SWCX induced emission at the helium focusing cone (HeFC) using the two low ecliptic latitude directions with Suzaku. Suzaku observed each direction twice from the different position on the Earth yearly round orbit. One observation contains the HeFC in the line of sight (LOS), and the other is far from it. To minimize the contributions of distant emission at oxygen lines beyond the heliosphere from us, we proposed the observations toward shadowing region by the dense molecular cloud MBM 16, located within < 100 pc in Suzaku AO5. We also used the Suzaku archival data toward NGC 2992. There are two archival observations of the NGC 2992, one with the LOS through HeFC, while the other not. The contribution of distant emission is expected in the NGC 2992 observations because the column density of neutral gas is not large enough.

6.2 Observations

Log of the observations are summarized in Table 6.1. To reduce the spatial variations of the distant emission beyond the heliosphere, we use the data sets with their field of views (FOVs) almost fixed. Figure 6.1 shows the schematic view of these configurations on the heliocentric ecliptic plane. The green area roughly shows the HeFC region where the density of neutral He is about twice larger than the average value $n_{\rm He} = 0.015$ cm^{-3} at 1 AU from the Sun (Gloeckler et al. 2004). In each data set, Suzaku LOS of one observation intersects with the HeFC, while the other does not by the orbital motion of the Earth.

The neutral column density toward MBM 16 is well studied from the observation of rotational and hyperfine structures of CH, and CO, and the color excess $E(B-V)$ in Magnani et al. (2003). The value of neutral column density in Suzaku FOV is $N_{\rm H} = 1.5 \times 10^{21} - 4.5 \times 10^{21}$ cm^{-2} that is a summation of atomic and molecular hydrogen column densities $[N({\rm HI}) + N({\rm H_2})]$. From the comparison between IRAS 100 μm and ROSAT maps, MBM 16 is considered to be located in the local bubble (LB) about $60-95$ pc from us (Kuntz et al. 1997). Assuming the above column density range, X-ray photons behind MBM 16 should be photoelectrically absorbed by 65–96 % at OVII Kα (0.57 keV), and by 51–89 % at OVIII Lyα (0.65 keV) (Henly & Shelton 2010). The neutral

Table 6.1 Log of the Suzaku observations toward MBM 16 and NGC 2992.

ID	Sequence	Start date	Exposure (ks)		Pointing		Roll angle
		YYMMDD hh:mm:ss	total*	screened†	Galactic	Ecliptic	
M16-onC	505061010	100802 16:49:43	80.8	33.8	(170°.98, −37°.86)	(50°.11, −7°.08)	73°.695
M16-offC	505062010	110130 03:08:15	82.8	36.1	(170°.96, −37°.85)	(50°.11, −7°.05)	253°.700
N2992-onC	700005010	051106 14:17:44	38.8	= total	(249°.67, 28°.82)	(154°.02, −26°.06)	102°.630
N2992-offC	700005020	051119 21:04:33	39.7	= total	(249°.69, 28°.83)	(154°.05, −26°.06)	88°.782

* Total exposure of the XIS1 extracted with the standard screening criteria and COR2 > 6 GV c^{-1}.

† Enhancement of the geocoronal SWCX induced emission was removed (§6.3.2).

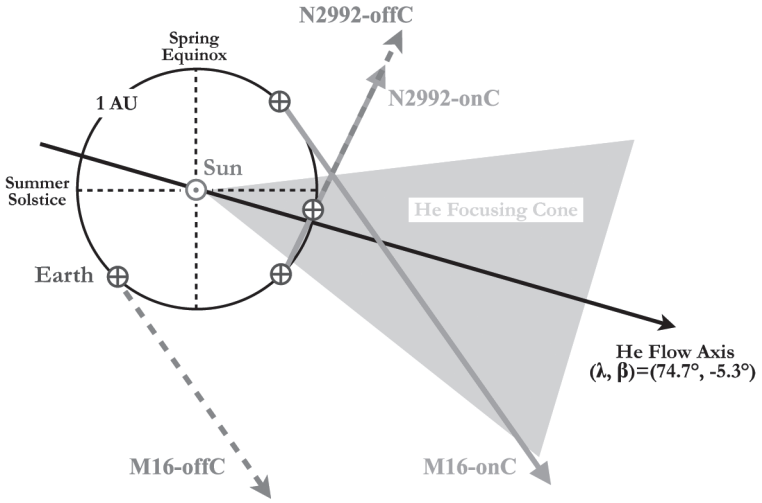

Figure 6.1 Schematic view of the observation configuration projected on the heliocentric ecliptic plane.

column density in our Galaxy toward NGC 2992 is $N_{\rm H} = 4.8 \times 10^{20}$ cm^{-2} (Kalberla et al. 2005) that absorbs 30 % of X-ray photons at OVII emission.

6.3 Data Reduction

We use the XIS1 cleaned event files that are processed with standard data screening criteria. To avoid high energy particles penetration due to the low Earth's magnetic field, we extracted the data when Cut Off Rigidity (COR2) was larger than 6 GV c^{-1}.

After the data were screened with the above criteria, we also removed the point sources and the interval when geocornal SWCX induced lines were enhanced (screening procedures were described in §6.3.1 and §6.3.2). Table 6.1 shows the exposures of total cleaned events and screened ones.

6.3.1 Removal of Point Sources

We removed typical bright sources to suppress their emission to the diffuse faint one of the interstellar space. NGC 2992 $(\ell, b) = (249.^\circ706, 28.^\circ781)$ and NGC 2993 $(\ell, b) = (249.^\circ761, 28.^\circ771)$ were removed by circular regions with radius $4.0'$ and $3.0'$ respectively. According to Yaqoob et al. (2007), energy flux of the NGC 2992 (brighter than NGC 2993) from 0.5 – 2.0 keV range was $\sim 1.6 \times 10^{-12}$ erg cm^{-2} s^{-1}. Leakage flux outside of the removed circular region is calculated $\sim 8 \times 10^{-14}$ erg cm^{-2} s^{-1} by using the Suzaku encircled energy function of the on–axis response (Serlemitsos et al. 2007). In contrast, the energy flux of the interstellar space was $\sim 3 \times 10^{-12}$ erg cm^{-2} s^{-1} in 0.5 – 2.0 keV estimated from the spectral fitting (details are described in §6.4). This is much lager than the leakage one from NGC 2992, and the contribution of these sources is negligible in our analysis.

Furthermore, we removed two point sources toward NGC 2992 and five ones toward MBM 16 whose energy fluxes were larger than 1×10^{-14} erg cm^{-2} s^{-1} in 0.4 – 5.0 keV by the circular regions with radius $2.0'$.

6.3.2 Reduction of Geocoronal SWCX Induced Emission

The two NGC 2992 observations were entirely settled in the fast and slow solar wind condition, respectively. These observations were not screened by the solar wind conditions. During the observations of MBM 16, interplanetary coronal mass ejection and corotating interaction region passed around the Earth. G-SWCX is usually enhanced in these interval (Snowden et al. 2004, Fujimoto et al. 2007). We removed from these observations for the spectral analysis the durations when the value of solar wind proton flux obtained by the product of its density and bulk velocity was larger than 4.0×10^8 cm^{-2}s^{-1} (Yoshino et al. 2009). The observation interval from the start to 70 ks and after 200 ks of M16-onC and that from the observation start to 80 ks of M16-offC were extracted for the spectral fitting, respetively.

We also calculate the distance of the Earth to magnetopause (ETM) in Suzaku line of sight (LOS). Because the LOSs toward both MBM 16 and NGC 2992 are far from the geomagnetic pole, ETM distances are always larger than $10\,R_{\rm E}$ that is longer than the typical scale height of geocoronal neutrals $\sim 8.2\,R_{\rm E}$ (Østgaard et al. 2003). In Yoshino et al. (2009), the enhancement of G-SWCX induced emission were confirmed only when the ETM distance is less then $5\ R_{\rm E}$ due to an increasing geocoronal neutral density below its scale height $\sim 8.2\,R_{\rm E}$. Therefore, we did not screen the data by the value of ETM distance.

To summarize, we reduced the data both of MBM 16 observations by the proton flux value. The observations of NGC 2992 were not screened.

6.4 Spectral Analysis

Response and background files used for the spectral fitting were created by the procedure in §4.2.1 and §4.2.2.

6.4.1 Broad Band Spectral Fitting from 0.4 to 5.0 keV

We tried to fit the Suzaku XIS1 spectrum from 0.4 to 5.0 keV. The emission model consisted of three components described in Chapter 2, 4, and 5, namely the

1. Cosmic X-ray Background expressed by double broken power laws absorbed by Galactic neutrals
2. Galactic Halo gas represented by a CIE plasma with the temperature of $kT \sim 0.2$ keV absorbed by Galactic neutrals.
3. a blend of SWCX induced lines and LB thermal gas represented by a CIE plasma with the temperature of $kT \sim 0.1$ keV surrounding our Solar system that could not be resolved (Yoshino et al. 2009; Henly & Shelton 2010)

The emission of CXB is modeled by the double broken power-laws shown in §4.2.3. The value of interstellar absorption toward NGC 2992 was fixed at the value of Kalberla et al. (2005) in the fitting. We treated the column density toward MBM 16 as a free parameter. Due to the expected strong photoelectric absorption and the location of MBM 16 (details are described in §6.2), the model of the Galactic halo emission is not contained toward MBM 16. The temperature of LB+SWCX blend was fixed at the typical temperature $kT = 0.099$ keV ($\sim 1.15 \times 10^6$ K).

Figure 6.2 shows the M16-onC/offC spectra with their best fit models and the parameters are summarized in Table 6.2. The case of the N2992-onC/offC observations is also shown in Figure 6.3 and Table 6.3. Both on and off cone spectra were fitted simultaneously and well reproduced by the best fit models (confidence level is ~ 50 % in both cases). Because the Suzaku FOVs covered almost the same sky between the on/off cone observations, the normalization of CXB and the temperature and emission measure of the Galactic halo were constrained to take same values. We also tried to fit the onC/offC spectra independently to confirm the simultaneous fitting. The best-fit parameters of the CXB and the Galactic halo were consistent within 1σ statistical range between the two spectra.

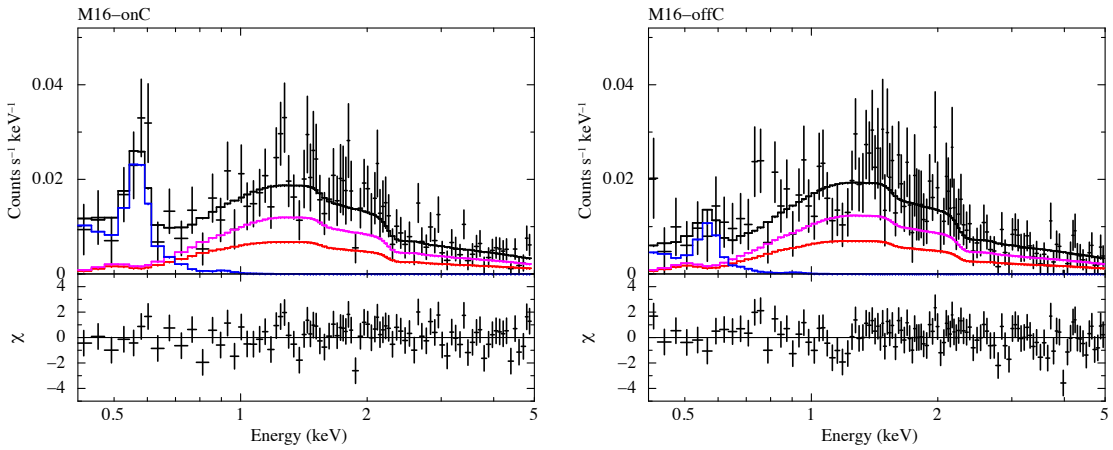

Figure 6.2 0.4 – 5.0 keV Suzaku XIS1 (back illuminated CCD) spectra and best fit emission models of the blank field toward MBM 16 (top panel) and residual of the fit (bottom panel). Left and Right panels show the onC and offC spectra, respectively. Black crosses show the observed spectra. Step lines show the models with best fit values; total (black), LB+SWCX (blue), CXB with $\Gamma = 1.54$ (magenta), and CXB with $\Gamma = 1.96$ (red), respectively.

Table 6.2 Results of spectral fitting toward MBM 16 with CXB + (LB+SWCX) models.

component	$N_{\rm H}$	CXB	LB+SWCX	OVII	OVIII	χ^2/d.o.f.
model	*phabs*	*phabs (bknpwls*)*	*APEC*†	*gaussian*	*gaussian*	
parameter		norm.	norm.	norm.	norm.	
unit	10^{21} cm^{-2}	‡	§	LU	LU	
M16-onC	$2.37^{+0.50}_{-0.46}$	3.5 ± 0.7	21.7 ± 5.9	–	–	200.8/201
M16-offC			$8.9^{+4.7}_{-4.8}$	–	–	
M16-onC	2.37 (fixed)	3.5 ± 0.5	15.8 ± 13.6	3.91 ± 1.25	< 0.76	198.5/198
M16-offC			14.9 ± 12.9	< 1.85	< 0.82	

* Photon indices are fixed to $\Gamma = 1.96$ and 1.54 below 1.2 keV, and 1.4 above that. Normalization of the power law with $\Gamma = 1.54$ is fixed at 5.7 photons s^{-1}cm^{-2}keV^{-1}sr^{-1}@1keV.

† Temperature of LB+SWCX is fixed at $kT = 0.099$ keV.

‡ photons s^{-1}cm^{-2}keV^{-1}sr^{-1}@1keV.

§ The emission measure, $(1/4\pi) \int n_{\rm e} n_{\rm H} ds$ in the unit of 10^{14} cm^{-5} sr^{-1}.

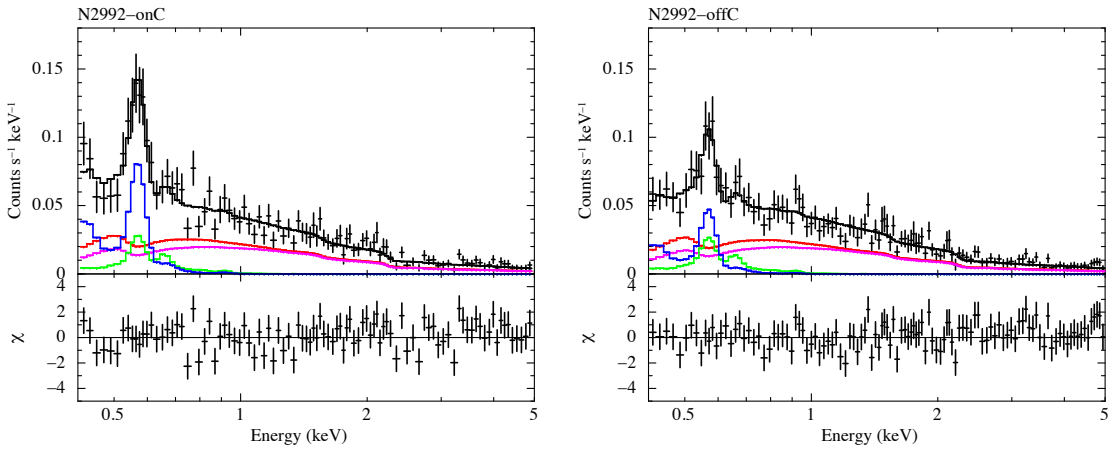

Figure 6.3 0.4 – 5.0 keV Suzaku XIS1 spectra and best fit emission models of the blank field toward NGC 2992 convolved with the CCD and telescope response (top panel) and residual of the fit (bottom panel). Left and Right panels show the onC and offC spectra, respectively. Black crosses show the observed spectra. Step lines show the models with best fit values; total (black), Galactic halo gas (green), LB+SWCX (blue), CXB with $\Gamma = 1.54$ (magenta), and CXB with $\Gamma = 1.96$ (red), respectively.

Table 6.3 Results of spectral fitting toward NGC 2992 with CXB + TAE + (LB+SWCX) models.

component	$N_{\rm H}$	CXB	Galactic Halo		LB+SWCX	OVII	OVIII	χ^2/d.o.f.
model	*phabs*	*phabs(bknpwls***)*	*phabs(APEC)*		*APEC*†	*gaussian*	*gaussian*	
parameter		norm.	kT	norm.	norm.	norm.	norm.	
unit	10^{21} cm^{-2}	‡	keV	§	§	LU	LU	
N2992-onC	0.48 (fixed)	6.6 ± 0.4	$0.171^{+0.048}_{-0.041}$	$2.8^{+5.2}_{-1.9}$	$21.7^{+5.9}_{-10.0}$	–	–	207.2/208
N2992-offC					$13.4^{+5.6}_{-9.8}$	–	–	
N2992-onC	0.48 (fixed)	$6.8^{+0.4}_{-0.5}$	0.171 (fixed)	< 5.1	$24.8^{+7.9}_{-9.6}$	4.64 ± 0.72	0.82 ± 0.38	205.2/205
N2992-offC					$18.5^{+7.0}_{-8.8}$	$3.17^{+0.62}_{-0.63}$	$0.51^{+0.36}_{-0.37}$	

* Photon indices are fixed to $\Gamma = 1.96$ and 1.54 below 1.2 keV, and 1.4 above that.
Normalization of the power law with $\Gamma = 1.54$ is fixed at 5.7 photons s^{-1}cm^{-2}keV^{-1}sr^{-1}@1keV.

† Temperature of LB+SWCX is fixed at $kT = 0.099$ keV.

‡ photons s^{-1}cm^{-2}keV^{-1}sr^{-1}@1keV.

§ The emission measure, $(1/4\pi) \int n_{\rm e} n_{\rm H} ds$ in the unit of 10^{14} cm^{-5} sr^{-1}.

6.4.2 Derivation of OVII and OVIII intensities

We fitted the same spectra again fixing the plasma temperatures at the best fit values, and plasma oxygen abundances at zero, but inserting three emission lines as Gaussian at OVII Kα (567 eV), Kβ (666 eV) and OVIII Lyα (653 eV), respectively (details are described in §4.2.4). The lower two rows in Table 6.2 and 6.3 show the best fit results with this new model. The normalizations of the inserted Gaussian are defined as the oxygen line intensities. In both MBM 16 and NGC 2992 cases, OVII lines of the on-cone observations are relatively enhanced to those of off-cone about 1–2 LU, while the differences of OVIII are not significant compared to the 90 % error range.

If the OVII and OVIII intensities were set to the same values between on/off observations, χ^2 increased from $\chi^2 = 198.5$ (198 d.o.f.) to 208.7 (200 d.o.f.) for MBM 16, and from $\chi^2 = 205.2$ (205 d.o.f.) to 213.2 (207 d.o.f.) for NGC 2992. According to the the F-statistics, the chance probabilities of obtaining the observed OVII and OVIII intensities differences by the Poisson statistics were less than $\sim 0.01\,\%$ ($= 0.7\,\%$ for MBM 16 $\times$ 1.2 % for NGC 2992).

6.4.3 Systematic Uncertainties of the Oxygen Line Enhancements

The systematic uncertainty to determine the absolute oxygen line intensities depends on the temporal variation of detection efficiency by the contamination accumulating on the XIS optical blocking filter. The systematic uncertainty of contaminant thickness is estimated to be $\pm 10\%$ to the nominal value of CALDB files (Suzaku technical description[*1]). If we overestimated the thickness by $+10\%$ at the onC observations and underestimated it by -10% at the offC ones (this is the worst case), chance probability to obtain the intensity difference got larger to 0.27% ($= 6.3\,\%$ for NGC 2992 $\times$ 4.3 % for MBM 16). The significance was still comparative to 3σ confidence level.

Next we check effects of the choice of the spectral fit model on oxygen line intensities. The values of hydrogen column density, the temperature of LB+SWCX component, and power law index of the CXB below ~ 1 keV would change from the fixed ones. According to Dickey & Lockman (1990), hydrogen column density toward the vicinity of NGC 2992 is $N_{\rm H} = 5.3 \times 10^{20}$ cm^{-2}. In Yoshino et al. (2009), the temperature of LB+SWCX component fluctuates from 0.08 to 0.14 keV toward fourteen blank fields in $65^\circ < \ell < 295^\circ$. Some works adopt the CXB model expressed by the single power law with $\Gamma = 1.4$ (Yoshino et al. 2009, Hagihara et al. 2010). Even if we change these parameters in the above ranges, the intensity of OVII emission changes by at most 0.4 LU from the results in §6.4.2 that is smaller than the statistical fluctuations. The oxygen line intensities were not susceptible to the uncertainty of emission model below 1 keV.

We conclude that the variations of the oxygen line intensity especially at the OVII Kα are significantly detected in these observations.

[*1] http://www.astro.isas.jaxa.jp/suzaku/doc/suzaku_td/

6.5 Comparison with the H-SWCX induced OVII Emission Model

We compare the observed OVII intensities with the heliospheric SWCX model predictions. For the SWCX model, we follow again that developed by Koutroumpa et al. (2006). The observations were done from November 2005 to February 2011 when the Solar Cycle 23 passed the minimum at early 2009[*2]. The long term solar activity during the observations is almost regarded as the minimum. As we have shown in the previous Chapter, the SWCX emission towards LH has increased since early 2010 due to increased solar activity. Thus the present observations of MBM 16 were made when the solar activity has started increasing from minimum. However, we have typical SWCX model parameters for solar minimum and maximum. We thus calculate the modeled H-SWCX intensities for the four observations assuming both minimum and maxim solar activities. We will try to compare them with the observations, respectively. In the model, both solar wind ions and interstellar neutrals distribute self-consistently by considering the loss processes by the charge exchange; the density of the solar wind ion basically has r^{-2} dependence from the Sun, and the densities of interstellar hydrogen and helium were simulated from the so-called classical "hot model" (Lallement et al. 1985) with the HeFC with an axis for $(\lambda, \beta) = (74^\circ.3, -5^\circ.3)$. We integrated the heliospheric SWCX emission along the LOS from the Earth to 20 AU from the Sun. Detail of the model are described in Appendix A.

The Suzaku LOS is entirely placed within the slow wind toward MBM 16, while it cuts across the slow wind region at ~ 0.8 AU from us toward NGC 2992 at solar minimum. The highest interstellar He density region exists at $0.4 - 0.5$ AU from us in the N2992-onC observation and most part of the expected HeFC region is included in the slow solar wind stream.

The intensities of simulated H-SWCX induced OVII emission are summarized in Table 6.4, and the observed intensity is plotted as a function of the model intensity in Figure 6.4. We fit the relation with a linear function

$$(\text{Observed OVII}) = (\text{Simulated OVII}) + (\text{Offset OVII}) \ , \tag{6.1}$$

where (Offset OVII) emission is treated as a free parameter. Fitting results are also summarized in Table 6.4 and Figure 6.4. Dashed lines in the figure show the best-fit model function. The observed intensity differences are better reproduced by the simulation under the solar minimum condition than the maximum one in both MBM 16 and NGC 2992. An offset intensity of ~ 2 LU is required to explain the observed OVII intensity of NGC 2992 direction, regardless of solar minimum/maximum assumptions. On the other hand, offset is not necessary for MBM 16 if we assume solar minimum with an upper limit of 0.1 LU. The offset is at most 1.3 LU if we assume the solar maximum model.

[*2] http://www.swpc.noaa.gov/SolarCycle/

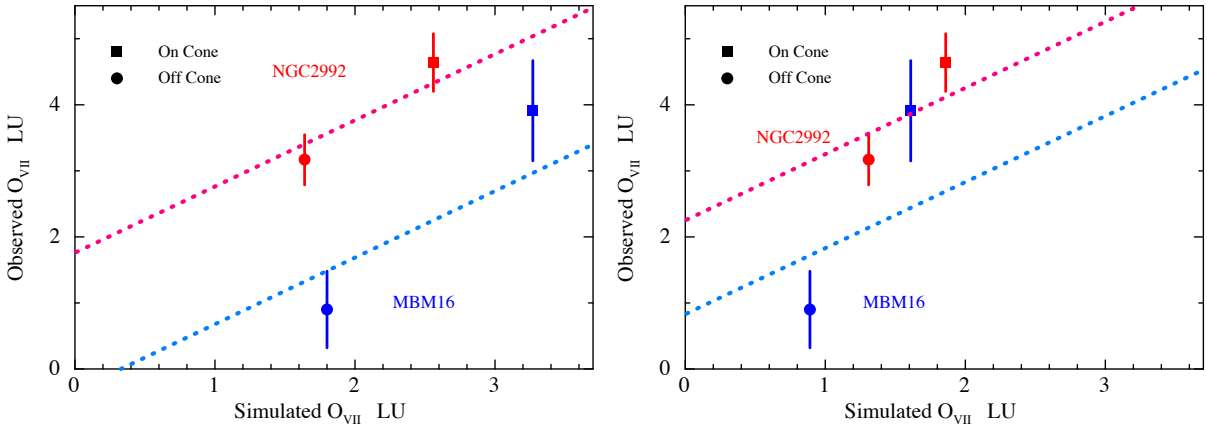

Figure 6.4 Comparison of OVII intensities between observation and H-SWCX simulation. Dash lines show the best fit value of Equation (6.1). Left panel : assuming the solar minimum situation. Right panel : assuming the solar maximum situation.

Table 6.4 Simulated H-SWCX induced OVII emission toward MBM 16 and NGC 2992, and expected offset OVII level to the 1:1 relation between observed and simulated intensities.

obsevations		minimum model			maximum model		
		LU	offset LU	$\chi^2/1$ (prob.)	LU	offset LU	$\chi^2/1$ (prob.)
MBM 16	OnC	3.27	-0.33 ± 0.46	2.60 (0.11)	1.61	0.83 ± 0.46	5.39 (0.02)
	OffC	1.80			0.89		
NGC 2992	OnC	2.56	1.76 ± 0.29	0.91 (0.34)	1.86	2.25 ± 0.29	2.54 (0.11)
	OffC	1.64			1.31		

6.6 Discussion

From the spectral analysis in §6.4.2, we found that the OVII line was enhanced in the observations through the HeFC. The intervals when the solar wind ion flux was enhanced were removed in §6.3.2, and the spatial variations of OVII emission is negligible because the Suzaku FOV are almost same in each observation set. We conclude that the OVII enhancements are actually due to the HeFC.

Enhancements of other line emission (OVIII, Fe-L complex, NeIX, and NeX) in these observations are not significantly detected over the statistical uncertainties. These lines are also expected to be enhanced at the HeFC. However, for example, the fraction of O^{+8} ion contained in the solar wind is typically less than $\sim 1/3$ of O^{+7}, while the charge exchange cross sections of O^{+8} are comparative to those of O^{+7} (Koutroumpa et al. 2006). Therefore, expected enhancements of OVIII emission are $\sim 1/3$ of that of OVII one which are less than statistical uncertainties. The results are consistent with the expectation, based on the typical solar wind properties.

From comparisons with simulated H-SWCX induced OVII emission developed by Koutroumpa et al. (2006), the offset OVII emission of $\sim$ 2.0 LU is required toward NGC 2992 to explain the observed intensities by the model both in solar minimum and maximum situations. However, the offset intensity is not necessary or at most 1.3 LU toward MBM 16. This suggests that the OVII emission towards MBM 16 can be explained only with the H-SWCX model. The contribution of the

LB component is smaller than that of the H-SWCX component. Due to the differences of neutral hydrogen column density between two directions, the $\sim$ 2.0 LU offset OVII emission in NGC2992 direction is thought to be the distant origin beyond the heliosphere. As we described in §6.3, this distant emission component is treated as hot gas in the Galactic halo. Within the uncertainties of the model parameters of the halo component in Table 6.4, OVII intensity of this component is estimated to be $1.2^{+2.2}_{-1.0}$ LU. This is consistent with the $\sim$ 2 LU offset.

7 Spatial Variability of OVII Emission over the Sky

7.1 Purpose of Analysis

From the results in Chapter 5 and Chapter 6, we confirmed the time and spatial variations of OVII emission. Both variations are consistent with those of H-SWCX induced emission: time one is related to the long term solar activity cycle with a $\sim$ 11-yr, and the other is to the anisotropic distribution of interstellar He atoms in heliosphere, namely the HeFC. OVII emission, having a large contribution on the SXDB in ROSAT R45 band, actually varies its intensity by the H-SWCX even in the same field of view, as some previous studies have predicted (Cox 1998, Robertson & Cravens 2003, Lallement 2004a, and Koutroumpa et al. 2006).

In this chapter, we finally investigate the emission beyond the solar system. We study the spatial variations of this emission component taking into account the time and spatial variabilities of the foreground SWCX emission for the first time. As we explained in Chapter 2, it is widely accepted that this variation relates to the emission from the LB and Galactic halo gas. To avoid contributions from other thermal plasma emissions of Galactic bulge, North Polar Spur, famous SNRs, and supper bubbles (Loop I, Cygnus loop, etc), we basically use the observations toward AntiGalactic center region where the galactic longitude is $60^\circ \lesssim \ell \lesssim 300^\circ$, where ROSAT R45 map widely shows almost the uniform intensity.

7.2 Observations

Figure 7.1 shows the ROSAT R45 band centered at AntiGalactic center $(\ell, b) = (180^\circ, 0^\circ)$. Observation points used in this analysis are plotted with white circles on the map, and they are numbered according to the galactic latitude. We use the Suzaku archival data as many as possible in $120^\circ \lesssim \ell \lesssim 240^\circ$ if the data satisfy the following conditions : point sources are not so bright, and exposure is sufficient to determine the OVII intensity. As we claimed in §7.1, the purpose of the study in this chapter is to investigate the origin of the faint diffuse emission widely extended in our Galaxy. Therefore, observations toward the famous superbubbles (Monogem Ring and Eridanus Super-bubble) and star forming region were also excluded in this analysis.

We limited the observation interval to investigate the spatial variability of OVII emission in a situation where the long term ($\sim$ 11-yr) solar activity can be regarded as the same level. Suzaku satellite was launched in July 2005, and observations are made over the solar minimum phase in Cycle 23th. However, OVII emission toward Lockman Hole has been enhanced since June 2010, while its variations from 2006 to 2009 were smaller than the statistical fluctuation according to

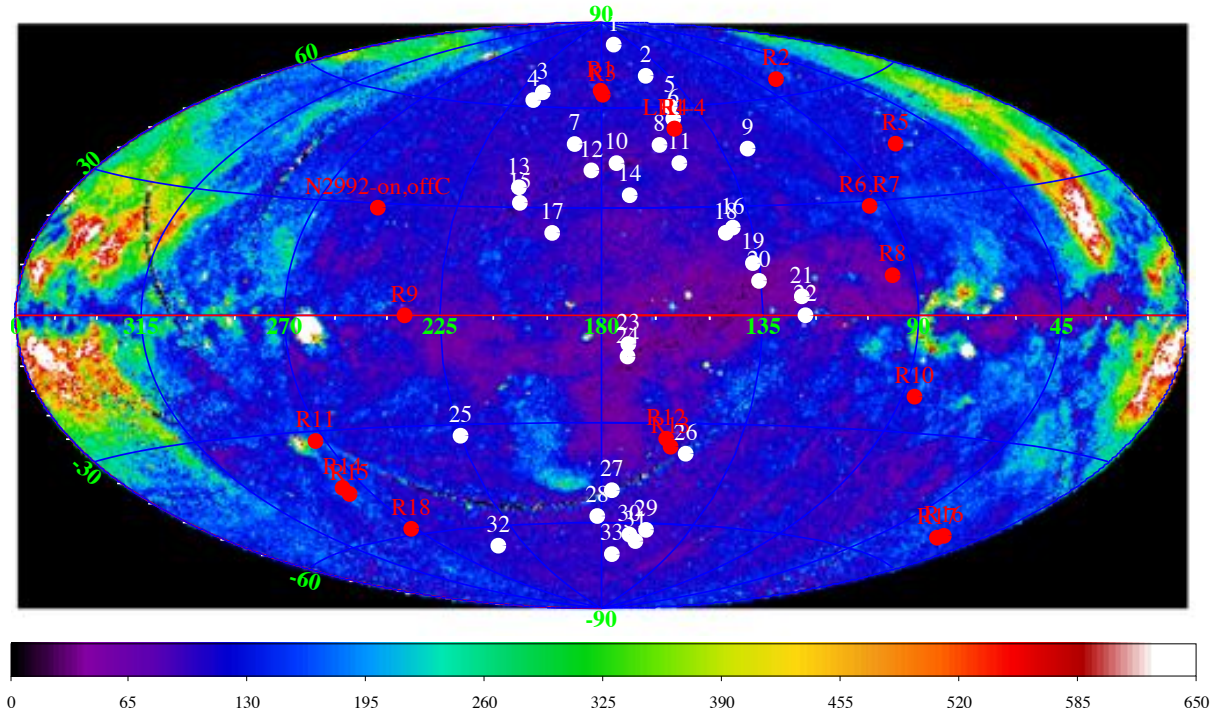

Figure 7.1 Suzaku observations on the ROSAT R45 band image. The image is centered at $(\ell, b) = (180°, 0°)$.

the result in §5. We discussed in Section 5.5 that this enhancement is related to the long-term variations of the solar activity in which the distribution of slow and fast winds on the Sun's surface changes. Then the solar-minimum model can be applied to the Suzaku observations until about 80 days before June 2010, since the slow wind propagate across $\sim$ 20 AU with a typical velocity of $\sim$ 400 km s^{-1} (McComas et al. 2008). As we explained in Appendix A, H-SWCX induced OVII emission witin 20 AU from us have $\sim$ 80 % of the total intensity in the Heliosphere (to termination shock at $\sim$ 90 AU from us). We also use results of 19 Suzaku observations of $90 < \ell < 120$ and $180 < \ell < 240$ by Yoshino et al. (2009), Hagihara et al. (2010), and Sakai et al. (in prep.). We also include the results obtained in Chapters 5 and 6. The observation directions used in this chapter are plotted in Figure 7.1. Referred LOSs are also plotted by red circles with ID R ♯ in Figure 7.1.

The informations of all observations we used here are summarized in Table B.1 and B.2 in Appendix B.1. We finally choose 33 archives that are appropriate for the above criteria. Observations are done in a long term $\sim$ 5 years from October 2005 to January 2010.

7.3 Data Reduction and Spectral Analysis

The processes of the data reduction and spectral analysis to derive oxygen intensities are basically same as previous chapters. We describe these processes and summarize the results in Appendix B. Intensities of observed OVII emission exist over a range from 1 to 6 LU, and those of OVIII from 0 to 2.5 LU. These intensities in referred papers are also summarized in Table B.6 in the appendix.

7.4 Calculation of Heliospheric SWCX induced OVII Emission

We calculate H-SWCX induced OVII emission using the model described in Chapters 5 and 6. As we described in §7.2, the observation interval used in this chaper is limited from September 2005 to January 2010 when the long term solar activity is regarded as the same situation judged by the Lockman Hole observations (Chapter 5). This interval covers the solar minimum in Cycle 23th that exist early 2009 [*1], and we therefore calculate the H-SWCX emission assuming the case of solar minimum in Koutroumpa et al. (2006). Table 7.1 shows the results of OVII emissions predicted by the H-SWCX induced model.

Table 7.1 Simulation Results of H-SWCX induced OVII emission.

ID	OVII	ID	OVII	ID	OVII	ID	OVII
	LU		LU		LU		LU
1	1.10	16	0.72	31	2.22	R13	3.14
2	1.12	17	3.23	32	1.27	R14	0.63
3	3.91	18	0.74	33	2.77	R15	0.63
4	2.75	19	0.74	R1	1.74	R16	3.35
5	0.90	20	0.59	R2	0.88	R17	3.34
6	1.44	21	0.71	R3	1.74	R18	0.65
7	2.30	22	0.67	R4	1.18		
8	0.92	23	2.17	R5	0.74		
9	0.70	24	1.89	R6	0.64		
10	1.40	25	0.65	R7	0.64		
11	0.72	26	2.03	R8	0.74		
12	1.77	27	3.15	R9	0.77		
13	2.13	28	1.13	R10	0.98		
14	0.96	29	2.51	R11	0.60		
15	3.46	30	2.22	R12	3.30		

7.5 Spatial Distributions of OVII emission

Figure 7.2 shows the Galactic latitude dependences of OVII and OVIII emissions observed with Suzaku. Plots are sorted with longitude by different colors. The neutral hydrogen column density $N_{\rm H}$ observed with LAB survey (Kalberla et al. 2005) is also shown in the bottom panel.

[*1] http://www.swpc.noaa.gov/SolarCycle/

For observations in $120° < \ell < 240°$, the intensity of OVII emission generally increases with incasing Galactic latitude in northern hemisphere (red plots in Figure 7.2). As seen in the bottom panel in the figure, the neutral column density increases at low latitude. It leads to the suggestion that the photoelectric absorption by the galactic neutrals contributes to the latitude dependence of OVII emission. The enhancement of OVII emission at high latitude region is also confirmed in southern hemisphere. However, it is not significant compared with the case of northern hemisphere. OVII emission in northern galactic hemisphere is brighter than that in southern. This difference between northern and southern hemispheres is apparent at high latitude direction. The OVII intensities are enhanced up to $\sim$ 6 LU where $b > 30°$, while they are suppressed to $\sim$ 4 LU where $b < -30°$. These features are also suggested from XMM-Newton observations in Henly & Shelton (2010) and become more explicit in our analysis. On the other hand, we cannot confirm the galactic latitude dependence of OVIII emission. Most OVIII intensities in $120° < \ell < 240°$ (red plots in Figure 7.2) distribute from 0 to 1 LU, and differences are smaller than the statistical fluctuations.

Observations whose OVII emission is larger than 6 LU are in most cases located outside $120° < \ell < 240°$ (black and blue plots Figure 7.2). They show deviations from the intensity trend confirmed in $120° < \ell < 240°$, and other contributions to these OVII enhancements are indicated.

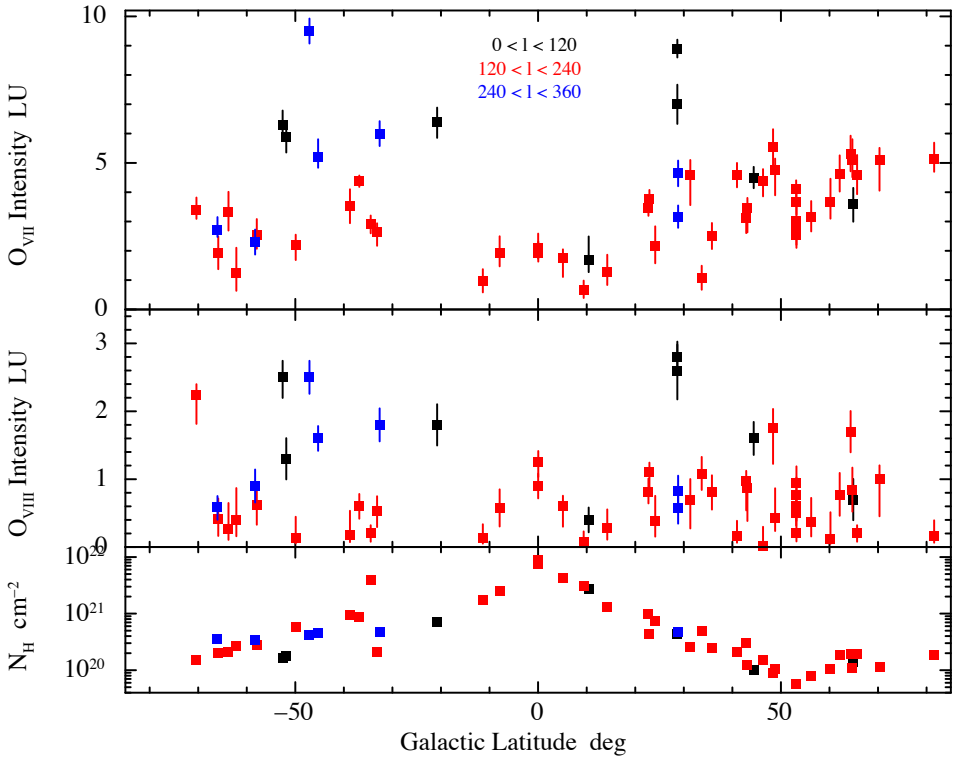

Figure 7.2 Galactic latitude dependence of oxygen emission lines. Top panel : OVII emission, middle : OVIII emission, and bottom : neutral column density $N_{\rm H}$.

Figure 7.3 shows the comparison of OVII emissions between Suzaku observation and the model of the H-SWCX induced emission calculated in §7.4. Red dashed line shows 1:1 relation between them. The plots are classified whether neutral column density is smaller (black cross with box) or

larger (blue cross with circle) than 1×10^{21} cm^{-2}. Most observed OVII intensities are larger than or equal to the simulated values. The data points with $N_{\rm H} > 1 \times 10^{21}$ cm^{-2} show smaller discrepancy from the 1:1 line compared to those with $N_{\rm H} < 1 \times 10^{21}$ cm^{-2}. The observed intensity is widely scattered for $N_{\rm H} < 1 \times 10^{21}$ cm^{-2}. Some data points exist near the 1:1 line.

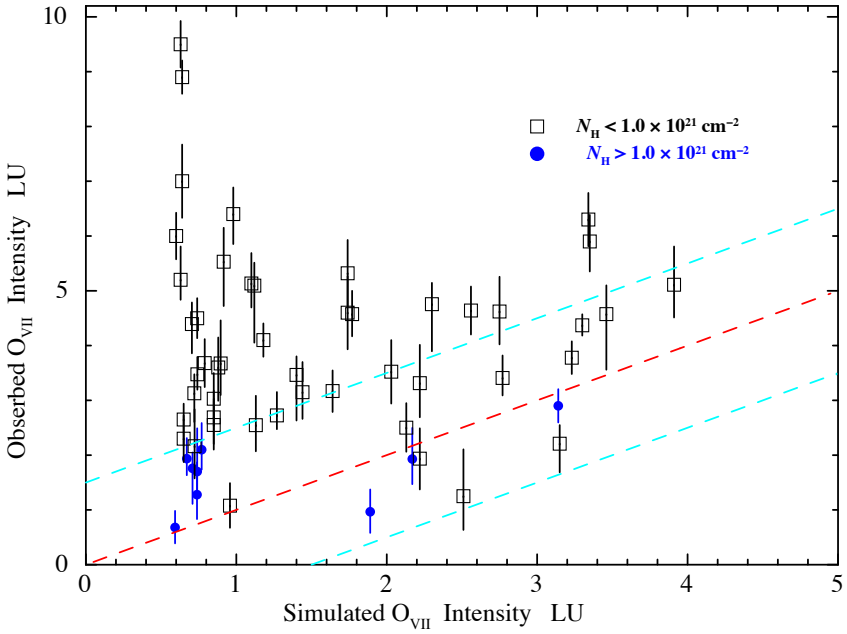

Figure 7.3 Comparison between the observed OVII intensity with Suzaku and simulated H-SWCX induced one. Red dashed line shows 1:1 relation between them. The sky blue dashed lines show the systematic uncertainties between the model and observation estimated from the multiple observation toward same field of views.

There is a still uncertainty in the prediction of the H-SWCX model. We estimate it from the differences of H-SWCX subtracted OVII emission among same field of views : N2992-onC and offC, LH1 to LH4, and R6 and R7 (North Ecliptic Pole). Table 7.2 summarizes H-SWCX subtracted OVII intensities of these three observation sets. The H-SWCX subtracted OVII intensities in the same field of view vary their nominal values from 0.1 LU (LH1 and LH4) to 2.9 LU (R6 and R7). Since there are five independent pairs and the maximum difference is 2.9 LU, we estimate that the model prediction uncertainty is roughly 1.5 LU at a 80 % statistical confidence. The sky blue dashed lines in Figure 7.3 show the systematic uncertainties ($\pm$1.5 LU) to the 1:1 relation between the model and observation, estimated from the multiple observation toward same field of views. All observations are larger than the lower limit of the systematic uncertainty. Especially, the intensities in the directions of $N_{\rm H} > 1 \times 10^{21}$ cm^{-2} are consistent to the H-SWCX model within the systematic uncertainties, and therefore it is suggested that the OVII emissions toward dense hydrogen column density regions are almost reproduced by the H-SWCX induced emissions. The other data points indicate that simulated H-SWCX induced emission determine the minimum intensity of the observed emission.

Table 7.2 Comparison of H-SWCX subtracted OVII emission in same field of views.

Observation Set	ID	(Observed − modeled H-SWCX) OVII LU
1	N2992-on	2.08 ± 0.72
	N2992-off	1.53 ± 0.62
2	LH1	1.70 ± 0.74
	LH2	2.89 ± 0.72
	LH3	2.18 ± 0.77
	LH4	1.84 ± 0.80
3	R6	8.26 ± 0.50
	R7	6.36 ± 1.10

7.6 Anti-Correlation between OVII Emission and Neutral Column Density

The Galactic latitude dependence of OVII emission in the previous section suggests that the OVII emission anti-correlates with the neutral column density. Figure 7.4 shows the relation between observed OVII emission and neutral hydrogen column density $N_{\rm H}$. When the column density is larger than 1.0×10^{21} cm^{-2}, OVII emission is systematically small. According to Henly & Shelton (2010), photoelectric absorption cross section to a neutral hydrogen at OVII emission (0.57 keV) is $\sigma = 6.965 \times 10^{-22}$ cm^2. This cross sections was calculated using data from Balucinska-Church & McCammon (1992), with a revised He cross section from Yan et al. (1998), and Wilms et al. (2011) interstellar abundances. If $N_{\rm H}$ is larger than 1.44×10^{21} cm^{-2}, the optical depth $\tau \equiv \sigma N_{\rm H}$ exceeds 1 and absorption is expected to be apparent to OVII emission. Magenta vertical dash line in the figure means that the optical depth $\sigma N_{\rm H} \sim 1$ at OVII emission (0.57 keV).

Figure 7.5 shows the ecliptic latitude dependences of observed OVII and OVIII emissions. Plots are sorted with longitude by different colors. If the observed OVII emissions are dominantly attributed to H-SWCX, their intensities will be enhanced at low ecliptic latitude zone $\sim |\beta| < 20^\circ$ during the solar minimum (Koutroumpa et al. 2006). However, there is no dependence on ecliptic latitude in OVII and OVIII intensities.

The OVII intensity in Figure 7.4 includes contribution of H-SWCX, which varies from 0.5 to 4 LU by point to point. Thus in order to study the relation between the excess emission over the H-SWCX and the neutral column density, we subtracted the model H-SWCX OVII intensity from each observed OVII intensity and plotted as a function of $N_{\rm H}$. A large fraction of data points looks to follow a simple relation;

$$I(N_{\rm H}) = I_0 \, e^{-\sigma N_{\rm H}} \ , \tag{7.1}$$

Namely, the unabsorbed intensity is uniform all over the sky, and the intensity is determined only by $N_{\rm H}$. We determined the value of I_0 by fitting the data. We excluded some data points from the

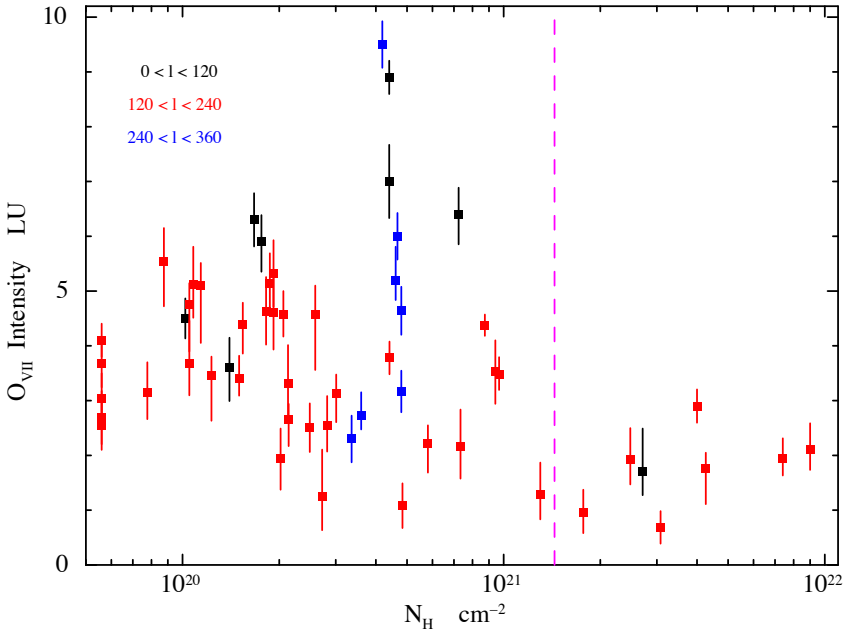

Figure 7.4 Suzaku OVII intensity v.s. LAB survey neutral hydrogen column density. Magenta dash line means that the optical depth at OVII emission (0.57 keV) equals to ~ 1.

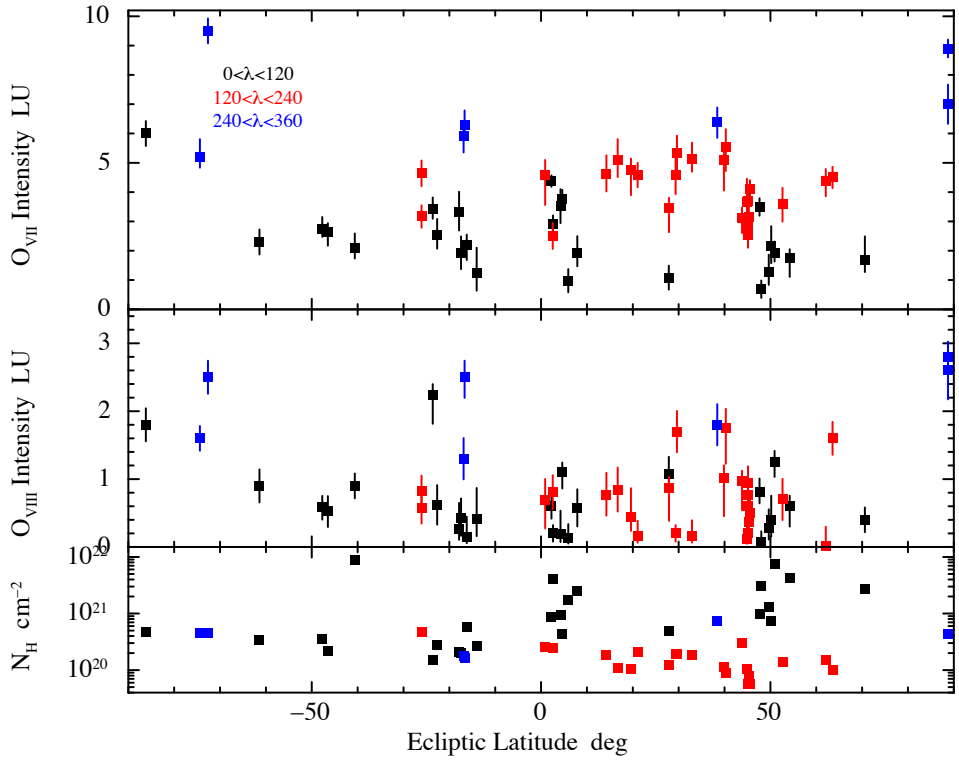

Figure 7.5 Ecliptic latitude dependence of oxygen lines. Top panel : OVII emission, middle : OVIII emission, and bottom : neutral column density $N_{\rm H}$.

fit because of the following reasons : Within $\sim$ 5 degrees from the Galactic plane, emission from unresolved faint dM stars are expected to contribute to the SXDB (Masui et al. 2009). The X-ray spectra of dM stars can be approximated with two-temperature thermal emission. The temperature of the lower-temperature component is about 0.2 keV and thus the emission contains OVII K. From

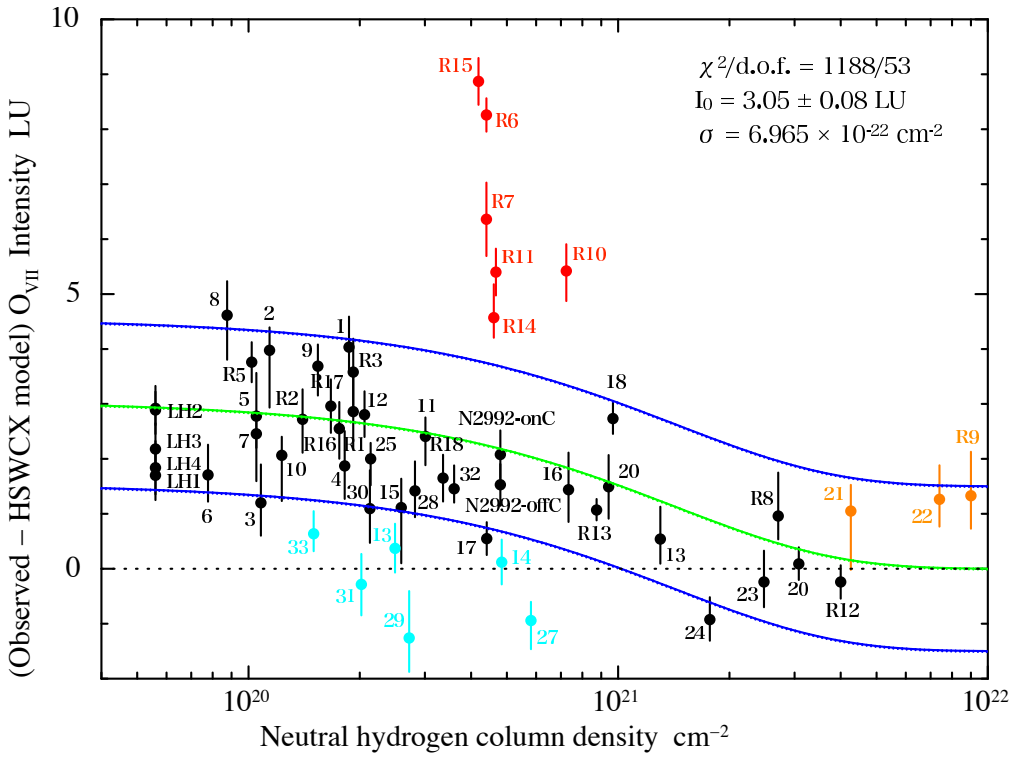

Figure 7.6 Anti-correlation between H-SWCX subtracted OVII emission and neutral hydrogen column density. Green curve shows the best fit model of Equation (7.1). Orange plots are not used for the fitting (see the text). Red (light blue) plots show the data whose intensities are larger (smaller) than the systematic uncertain ranges of the model.

Light green curve in Figure 7.6 shows the best fit model of Equation 7.1. The systematic uncertain ranges are drawn by blue curves in the figure. The 42 of 54 observations are consistent with the uniform absorbed model within the systematic uncertainties. Rest of data points are brighter (red) or fainter (sky blue) than the model. We show the directions of observations in Figure 7.8 again with bright and faint points distinguished (black points in Figure 7.6 are white in Figure 7.8).

It is found that the bright and faint data points are not distributed randomly but gathering in limited regions of the sky. Bright data points are found at $\ell \sim 90°$ and $\ell \sim 270°$. These regions actually show the brighter emission than the region in $120° < \ell < 240°$ in the ROSAT R45 map. Faint data points are mainly found southern high latitude area of $\ell = 150° - 180°$ and $b = -50°$ to $-70°$.

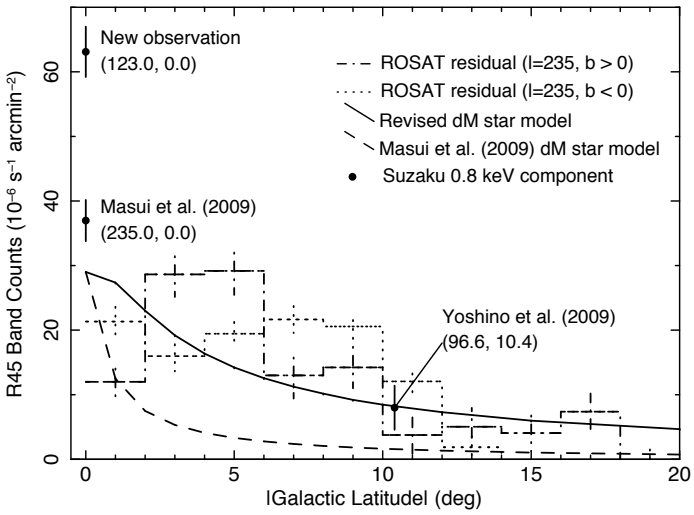

Figure 7.7 Residuals of R45 band surface brightness from the unabsorbed constant emission + CXB model (step functions), and expected X-ray fluxes from faint dM stars (solid curve) as functions of the galactic latitude (Kimura et al. 2009).

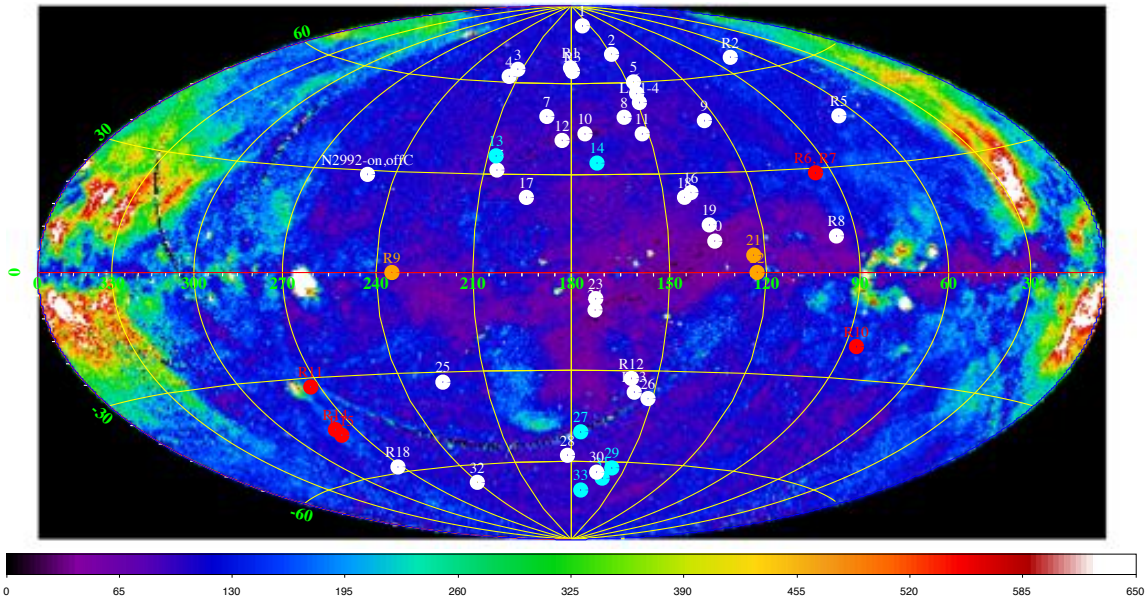

Figure 7.8 Suzaku observations on the ROSAT R45 band image. The image is centered at $(\ell, b) = (180°, 0°)$. Observations were classified by different colors whether the H-SWCX corrected OVII emission is larger or smaller than the emission model in Equation (7.1).

7.7 Discussion

7.7.1 Plane-parallel Model for Galactic Halo

From the systematic analysis in this chapter, we found that the observed OVII emission showed the anti-correlation with absolute Galactic latitude, and contribution of the emission absorbed with Galactic neutrals is suggested from the trend. Therefore, we applied the absorbed constant emission in Equation (7.1), and tried to fit the OVII emission that was subtracted the H-SWCX induced one predicted by the model. The intensities of OVII emission for 42 of 54 observations are included in the systematic uncertainties of the model caused by the differences of H-SWCX induced emission between model prediction and real observation. These observations can be explained by this simple emission model, while there are explicit bright or faint intensities to the model.

From the widely accepted picture of SXDB, the hot gas in the Galactic halo is thought as the origin of the absorbed constant emission (e.g. : recent studies are Yao et al. 2009, Yoshino et al. 2009, and Henly & Shelton 2010). The Galactic halo emission is often approximated as the "Plane Parallel Model". This model represents the shape of the halo gas as a thick disk parallel to the Galactic plane, and the halo emission for a given line of sight depends only on

$$I_{\rm halo}(b) = I_{\rm zenith} / \sin|b| \ , \tag{7.2}$$

where $I_{\rm zenith}$ is the intrinsic halo emission extending perpendicular to the galactic plane. We correct the H-SWCX subtracted OVII emission by multiplying $\sin|b|$, and check if this geometric effect have influences to the OVII bright and faint observations. The anti-correlation between H-SWCX subtracted and $\sin|b|$ corrected OVII and neutral column density is shown in Figure 7.9. The colors of the plots are same as Figure 7.6. The uncertain ranges are also same as §7.6 ($\pm$1.5 LU), because the H-SWCX induced emission does not relate with the plane parallel geometry. In this case, though the fluctuations among the observations are smaller than the results in previous section §7.6, there still remain the bright or faint directions.

7.7.2 Possible Origin of the Non-uniformity of Distant OVII Emission

The light and dark trend of distant OVII emission over the sky obtained in §7.6 still remains, even if the geometric $\sin|b|$ effect of the plane parallel emission source is corrected in §7.7.1. In addition, observations toward high Galactic latitude area in the northern hemisphere after the $\sin|b|$ correction are found to be relatively enhanced (ID 1, 2, 8, and R3 are significant in Figure 7.9). We discuss the possible origin of this spatial non-uniformity of distant OVII Emission.

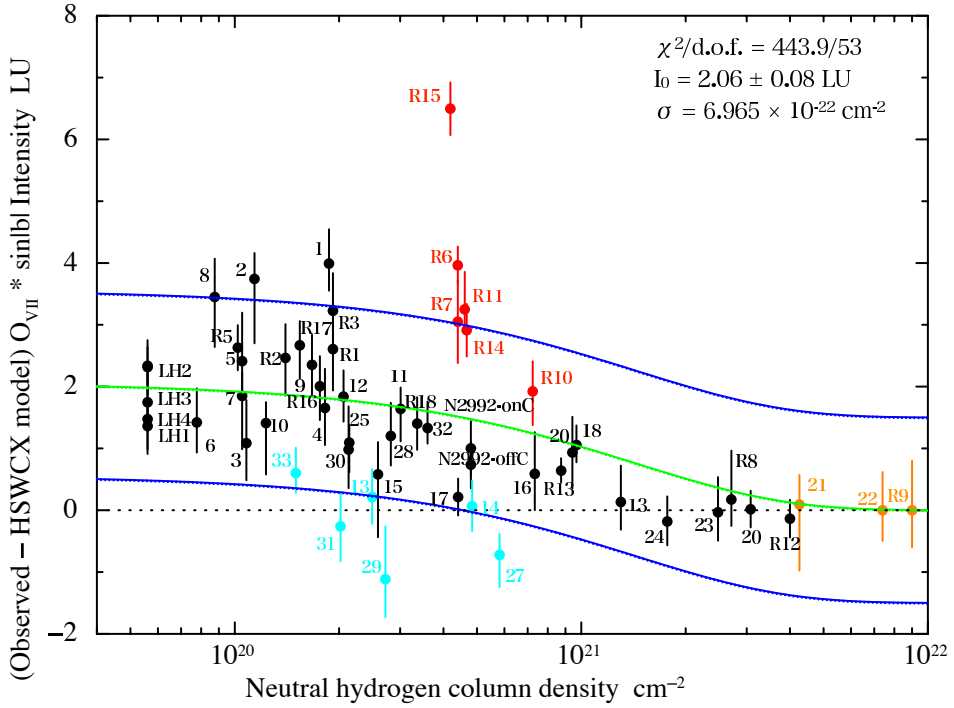

Figure 7.9 Anti-correlation between both H-SWCX subtracted and sin $|b|$ corrected OVII emission and neutral hydrogen column density. Colors are same as Figure 7.6.

As we described in the Review, possible origins of the heating mechanism in the Galactic halo are mainly considered as following three phenomena :

1. SN or stellar wind-driven outflows from the Galactic disk, so-called Galactic Fountain.
2. In situ heating by SNe above the plane. In this scenario, the observed hot gas is within isolated SNRs at a variety of heights above the disk and of a variety of ages.
3. Gravitational heating of in-falling intergalactic materials.

All three mechanisms heat up the ISM locally and could explain the non-uniformity of distant OVII emission. Here we focus on the 3rd mechanism, and compare the spatial distribution of expected in-falling materials. As a candidate of the in-falling materials that emit in soft X-ray energy band, contributions of high velocity clouds (HVCs) are often debated (Kerp et al. 1999, Shelton et al. 2010). HVCs, which are materials traveling with speeds > 90 km s^{-1} relative to the Local Standard of Rest (LSR), are distributed inhomogeneously across the sky. Instead, they form large complexes, some of which extend over tens of degrees.

In Figure 7.10, distributions of HVCs identified by the LAB survey (Kalberla et al. 2005) are represented in Galactic coordinate centered at AntiGalactic center. Colors of HVC complexes mean the relative velocity to the LSR. The Suzaku 57 observation points are also plotted in the figure. The regions where the OVII are enhanced are relatively consistent with the position of the HVC complexes (toward LMC and complex C). Furthermore, there are few HVCs toward the Suzaku observation points where OVII emission is faint (southern high latitude area of $\ell = 150^\circ - 180^\circ$ and

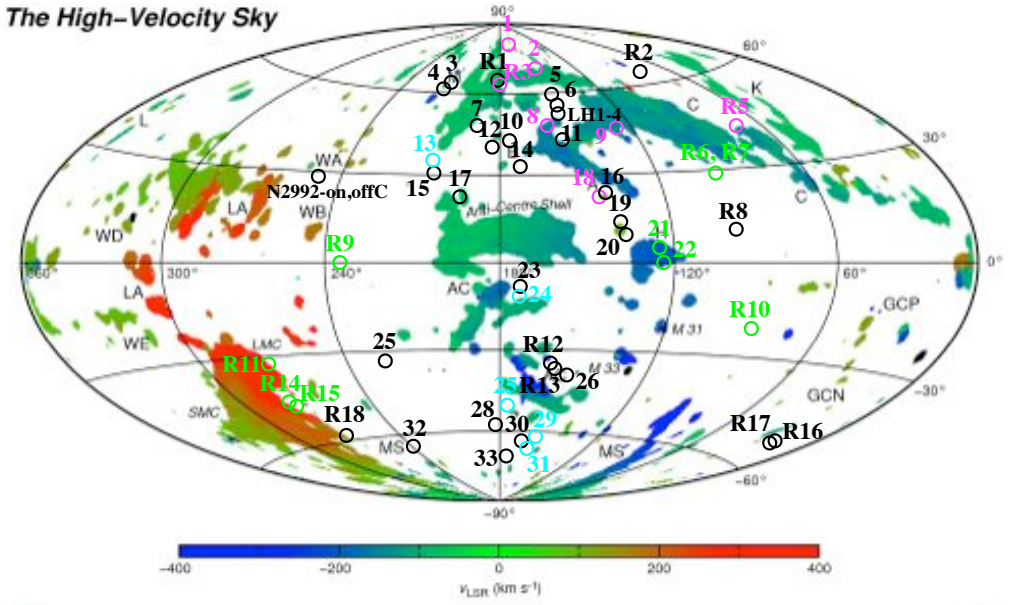

Figure 7.10 Suzaku observations overlaid on the HVC catalog with LAB survey. The image is centered at $(\ell, b) = (180°, 0°)$.

$b = -50°$ to $-70°$). Assuming that ideal gas is heated by the shock and emits X-rays, thin thermal plasma with temperature $kT = 0.1$ keV in collisional ionization equilibrium requires its velocity :

$$V_s = \sqrt{\frac{16}{3}\frac{kT}{m}} \sim 230 \left(\frac{kT \text{ keV}}{0.1}\right)^{1/2} \text{ km s}^{-1} . \tag{7.3}$$

This is actually comparative to the velocity of HVCs, and they move fast enough to heat up their materials to X-ray emission sources. Therefore, HVCs are thought to be the cause of non-uniformity of distant OVII emission obtained in this analysis.

8 Conclusions

We have investigated the time and spatial variabilities of soft X-ray diffuse background (SXDB), especially focusing on the OVII (0.57 keV) emission. Suzaku XIS1 (back illuminated CCD) achieves high sensitivity for spatially extended emission under 1 keV and OVII emissions are clearly detected. In the data reduction, we carefully removed the contributions of the solar-wind charge exchange induced X-ray emission from the Earth's geocorona (G-SWCX). We have obtained new insights on the variabilities of SXDB with Suzaku observations listed below.

8.1 Variability of Heliospheric SWCX induced OVII Emission

8.1.1 Long Term Variability related to the 11-year Solar Cycle

Long-term time variabilities of the OVII emission in the SXDB are studied by using six annual observations of blank sky towards Lockman Hole from 2006 to 2011.

1. Intensities of OVII emissions from 2006 to 2009 are 2.55 ± 0.74 (2006), 3.68 ± 0.72 (2007), 3.03 ± 0.77 (2008), 2.69 ± 0.80 (2009) LU (= photons s^{-1} cm^{-1} sr^{-1}), which are consistent within 90% statistical errors. However, the intensities in 2010 and 2011 are 6.06 ± 1.07 and 5.28 ± 1.60 LU, respectively. They are $2 - 3$ LU larger than the earlier four observations. Statistical significances of the OVII intensity variation of 2010 and 2011 with respect to an average of 2006 to 2009 ($= 2.99 \pm 0.38$ LU) are 4.5σ (2010) and 2.3σ (2011), respectively.

2. Since all the observations are made in the same season of a year, the variation cannot be due to the parallax of Heliospheric SWCX (H-SWCX) induced emission. We suggest that it is related to the variation of H-SWCX caused by the geometrical change of slow and fast solar wind structures associated with the 11-year solar activity.

8.1.2 Enhancement at the He Focusing Cone

We analyzed multiple observations of two blank sky fields towards the dense molecular cloud MBM 16 and vicinity of the Seyfert galaxy NGC 2992 with Suzaku in order to evaluate enhancement of the SWCX induced emission by the Helium Focusing Cone (HeFC). Suzaku observed each direction twice at different Earth orbital phases. The line of sight of one of the observations is through the HeFC, while that of the other not.

1. The intensity of OVII emission was estimated to be 3.9 ± 1.3 LU (MBM 16) and 4.6 ± 0.7 LU (NGC 2992) on the HeFC, while it was < 1.9 LU (MBM 16, 90 % upper limit) and 3.2 ± 0.6 LU (NGC 2992) off the HeFC, respectively. The chance probability of obtaining the observed intensity differences by the Poisson statistics is less than 0.3 % for both directions.

2. We compared the OVII differences between each HeFC on/off observations using the simulation of H-SWCX induced emission in Koutroumpa et al. (2006). The observed intensity differences are better reproduced by the simulation under the solar minimum condition than the maximum one in both MBM 16 and NGC 2992. Toward MBM 16, 90 % upper limit of the offset OVII intensity to reproduce observed OVII emission by the model is 0.1 (1.3) LU for solar minimum (maximum) simulation. Due to the strong interstellar absorption at MBM 16, emission from the Galactic halo is mostly blocked and this small offset means the contribution from LB to OVII emission.

3. Whichever the simulation was applied with solar minimum or maximum situations, simulated OVII emission requires ~ 2 LU offset intensity for the NGC 2992 field. This ~ 2 LU offset OVII emission is consistent with the model parameters of the spectral model component interpreted to be from the halo of our Galaxy.

8.2 Spatial Variability of OVII Emission over the Sky

We investigate the spatial variability of OVII emission over the sky, except toward Galactic center, local superbubbles, and SNRs. 57 observations are used for the systematic analysis.

1. The observed OVII emission anti-correlates with Galactic latitude in northern hemisphere. However there is no ecliptic latitude dependence if the H-SWCX induced emission has significant contribution to the SXDB. These results suggest the contribution of the emission absorbed with Galactic neutrals.

2. Most of the observed OVII emission are larger than the simulated H-SWCX induced one. For 45 of 57 observations, the relation between H-SWCX subtracted OVII emission by the model and neutral hydrogen column density can be expressed as the constant emission absorbed by the Galactic neutrals that is suggested by the contribution from the Galactic halo. There are relatively bright or faint directions of the OVII emission to the above model. These regions are comparatively grouped on the sky.

8.3 Picture of the SXDB Obtained through This Work

Figure 8.1 shows the schematic view of an expected picture of the SXDB through this work (similar to Figure 2.14). For the observations whose line of sight is limited within $\sim$ 100 pc from us due to the strong interstellar absorption by the dense molecular clouds, filaments, or cold ISM in the Galactic plane, intensities of observed OVII emission are consistent with the H-SWCX induced ones predicted by the model in Koutroumpa et al. (2006) (The results of MBM 16 in §6 and low Galactic latitude regions in §7). Therefore the local emission within $\sim$ 100 pc from us is thought to be originated in the H-SWCX, and OVII emission from the LB is so faint that it cannot contribute the SXDB. The OVII emission farther than $\sim$ 100 pc is well reproduced by the uniform emission absorbed by the Galactic neutrals (The results of the systematic analysis in §7). It suggests that the distant emission mainly exists beyond the Galactic plane. Though the origin of this distant emission is not revealed in this work, present picture of the X-ray emission form the Galactic halo is consistent with our results.

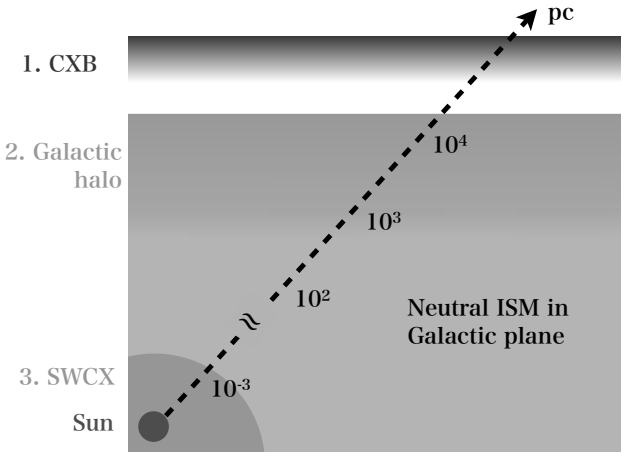

Figure 8.1 Schematic view of the expected picture of the SXDB through this work.

A Model of Solar-Wind Charge Exchange Induced Emission in the Heliosphere

In this appendix, we introduce the model of heliospheric solar-wind charge exchange (H-SWCX) induced line emissions developed in Koutroumpa et al. (2006).

A.1 Basic Reaction

We show the chemical process of SWCX phenomena. The solar wind ion X^{Q+} reacts with the neutral hydrogen or helium in the interplanetary field. Interstellar neutral flow is mainly composed of H ($\sim$ 0.1 cm^{-3} at 1 AU) and He ($\sim$ 0.015 cm^{-3} at 1 AU). Hereafter we consider the SWCX reaction with only these two elements. The chemical equation of the charge exchange between sola-wind ion X^{Q+} and neutral atoms is expressed as follows

$$\begin{aligned} X^{Q+} + [H, He] &\rightarrow X^{*(Q-1)+} + [H^+, He^+] \\ &\rightarrow X^{(Q-1)+} + [H^+, He^+] + [Y_{(h\nu,H)}, Y_{(h\nu,He)}] \ . \end{aligned} \tag{A.1}$$

In the first step of (A.1), $*$ shows the electron transferred from neutrals to solar-wind ion is bounded in the excited sate where the first quantum number $n > 1$. This electron moves to a ground state with emitting X-rays corresponding to the de-excitation energy. There are some transition paths from the excited state to the ground, and the photon yields $Y_{(h\nu,\ \mathrm{H\,and\,He})}$ of each spectral line $h\nu$ are added in second step of the equation.

A.2 Distribution of Solar-Wind Heavy Ion

Based on the Equation (A.1), we can calculate density distribution of solar-wind ion X^{Q+} consistent with the recombination loss of itself by CX. Before starting the calculation of this self-consistent ion distribution, we check simple distribution to the radial direction.

The divergence in the spherical coordinate is

$$\mathrm{div}\vec{A} = \frac{1}{r^2}\frac{\partial}{\partial r}(r^2 A_r) + \frac{1}{r\sin\theta}\frac{\partial}{\partial\theta}(A_\theta \sin\theta) + \frac{1}{r\sin\theta}\frac{\partial A_\phi}{\partial\theta} \ . \tag{A.2}$$

If (θ, ϕ) angular dependences of the CX process is negligible, a simple r^{-2}-dependent ion distribution

is expected :

$$\frac{1}{r^2}\frac{\partial}{\partial r}(r^2 A_r) = \frac{2}{r}A_r + \frac{dA_r}{dr} = 0 \ ,$$
$$A_r = \frac{\text{const.}}{r^2} \ . \tag{A.3}$$

If we also add the recombination by CX, transfer equation in the stationary state is written as

$$\frac{dN_{\mathrm{X}^{Q+}}}{dr} = - \ N_{\mathrm{X}^{Q+}} \left(\sigma_{(\mathrm{H},\mathrm{X}^{Q+})} n_{\mathrm{H}}(r) + \sigma_{(\mathrm{He},\mathrm{X}^{Q+})} n_{\mathrm{He}}(r) \ \right) - \frac{2}{r} N_{\mathrm{X}^{Q+}} \ . \tag{A.4}$$

The second term of the r.h.s. in Equation (A.4) indicates the distribution without CX reaction, same as Equation (A.3). Therefore, Equation (A.4) has a limit solution of $N_{\mathrm{X}^{Q+}}(r)$ to the CX cross section σ when

$$\lim_{\sigma \to 0} N_{\mathrm{X}^{Q+}}(r) = \frac{N_{\mathrm{X}^{Q+0}}}{r^2} \ . \tag{A.5}$$

Following this limitation, we obtain the radial distribution of solar-wind ion

$$N_{\mathrm{X}^{Q+}}(r) = \frac{N_{\mathrm{X}^{Q+0}}}{r^2} \exp\left[- \int_{r_\mathrm{o}}^{r} \left(\sigma_{(\mathrm{H},\mathrm{X}^{Q+})} n_{\mathrm{H}}(x) + \sigma_{(\mathrm{He},\mathrm{X}^{Q+})} n_{\mathrm{He}}(x) \ \right) dx \right] \ , \tag{A.6}$$

where r is the radius from the Sun. The boundary condition is given at 1 AU (i.e. $r_\mathrm{o} = 1$ AU), and $N_{\mathrm{X}^{Q+0}}$ is the ion density at 1 AU. In this mode,l solar wind ion density is referred from the observation data of SWICS/SWIM onboard ACE satellite orbiting at L1.

Koutroumpa et al. (2006) characterizes the two different states of the solar wind, respectively termed the slow solar wind and the fast solar wind. The slow solar wind has a velocity of about 400 km s^{-1}, a temperature of about 1×10^6 K and a ion composition close to the solar corona. On the other hand, the fast solar wind has a higher velocity of about 750 km s^{-1}, a lower temperature of about 8×10^5 K than the slow one, and it nearly matches the ion composition of the Sun's photosphere seen from the coronal hole. Parameters of the slow and fast solar wind used in this model are summarized in Table A.1. The selective and total cross sections of the CX collisions of the heavy solar wind ions have been constructed using relevant data from the laboratory measurements and theoretical calculations. At solar minimum, "slow" wind, which has a proton density of 6.5 cm^{-3}, velocity of 400 km s^{-1}, O/H number ratio of 1/1780, and O^{+7} fraction of 0.20 at 1AU, is assumed to extend below $|\beta| = 20°$. The "fast" wind above $|\beta| = 20°$ has a proton density of 3.2 cm^{-3}, velocity of 750 km s^{-1}, O/H number ratio of 1/1550, and O^{+7} fraction of 0.07 at 1AU. The cross sections of the O^{+7} charge exchange process are also different between two winds because of the difference of the velocity. They are taken at $3.40/3.70 \times 10^{-15}$ cm^2 with H, and $1.80/1.97 \times 10^{-15}$ cm^2 with He for the slow/fast wind that are also the same as the paper. On the other hand, the model assumes that the slow wind covers the solar surface entirely at solar maximum. Density of neutral interstellar atoms decreases due to the strong ionization loss via photoionization and charge exchange. Therefore, H-SWCX induced emission is expected to be enhanced at high ecliptic zone $|\beta| > 20°$, while it is reduced at low ecliptic zone $|\beta| < 20°$.

Table A.1 Slow and Fast solar wind parameters.

Solar wind type			Slow			Fast	
$V_{\rm SW}$ (km s^{-1})			400			750	
$[\frac{\rm O}{\rm H^+}]$			1/1780			1/1550	
$n_{\rm H^+}$ at 1 AU cm^{-3}			6.5			3.2	
	Spectral Lines (keV)		$\sigma_{(\rm H,X^{Q+})}$	$\sigma_{(\rm He,}X^{Q+})$		$\sigma_{(H,\rm X^{Q+})}$	$\sigma_{(\rm He,}X^{Q+})$
$\rm X^{Q+}$	produced by $\rm X^{*(Q-1)+}$	$[\frac{\rm X^{Q+}}{\rm O}]$	10^{-15} cm^2	10^{-15} cm^2	$[\frac{\rm X^{Q+}}{\rm O}]$	10^{-15} cm^2	10^{-15} cm^2
$\rm O^{7+}$	(f0.561, i0.569, r0.574)	0.200	3.40	1.80	0.030	3.70	1.97

A.3 Distribution of Neutral Atom in Heliosphere

The distributions of the neutral atoms are also necessary to solve Equation (A.6). Time dependent distribution function of a particle $f(\vec{r},\vec{v},t)$ is generally expressed by the Boltzmann equation :

$$\frac{\partial f}{\partial t}+\vec{v}\cdot\frac{\partial f}{\partial \vec{r}}+\frac{\vec{F}}{m}\cdot\frac{\partial f}{\partial \vec{v}}=\frac{df}{dt}\ , \tag{A.7}$$

where $\vec{F}$ a force acting on the particle. For the neutral atoms in the heliosphere, their motions are affected by both the Sun's gravity and the radiation pressure of solar UV photons and protons . These two forces have r^{-2} dependence from the Sun, and equation of motion of neutrals is simply described as follows :

$$\vec{F}=m\frac{d^2\vec{r}}{dt^2}=-\frac{GM_\odot(1-\mu)m}{r^2}\frac{\vec{r}}{r}\ . \tag{A.8}$$

Here we define the force ratio between the gravity and radiation pressure

$$\mu\equiv\frac{F_{\rm radiation}}{F_{\rm gravity}}\ . \tag{A.9}$$

This ratio determine whether the heliospheric potential energy works on the interstellar neutral flow attractively ($\mu<1$ penetrating into heliosphere) or repulsively ($\mu>1$ reflected from the heiosphere).

Neutral atoms are likely of being photo ionized by UV photons and charge exchanged with protons. These effects occur notably as the atoms approach to the Sun in on the significant more influent when the particles are near the Sun. We introduce the the rate of ionization losses β, and Equation (A.7) has a characteristic solution :

$$\frac{df}{dt}=-\beta f\ . \tag{A.10}$$

To calculate the distribution function $f(\vec{r},\vec{v},t)$, it is assumed in this model that :

1. The situation is stationary, i.e. $\partial f/\partial t=0$.
2. The neutral atoms approaching the Sun are subject to the stationary, spherically symmetric effective solar gravitational force, and $\mu=$ const. .

3. The neutral atoms approaching the Sun are subject to the stationary, spherically symmetric effective ionization.

The characteristic of Equation (A.10) coincides with the trajectories of the individual particles. Therefore, Equation (3.16) can be integrated over the particle trajectory s from $s = \infty$ ($t = -\infty$) to a present position $s = r$ ($t = t$).

$$f(\vec{r}, \vec{v}, t) = f(\vec{v}_\infty) \exp\left(-\int_{-\infty}^{r} \beta \frac{ds'}{v}\right) = f(\vec{v}_\infty) \exp\left(-\int_{-\infty}^{t} \beta \, dt\right) = f(\vec{v}_\infty)\, \nu \ , \qquad \text{(A.11)}$$

where ν is an extinction factor of the neutral atom by ionization losses, and $\vec{v}_\infty$ means the velocity at infinity of the particle that has velocity $\vec{v}$ at point ($\vec{r}$, t). From the assumption 3, ionization losses β can be expressed $\beta \equiv \beta_{\rm E} r_{\rm E}^2 / r^2$, where $\beta_{\rm E}$ is the rate of losses at the Earth' s orbit and $r_{\rm E}$ is 1 AU (from the Sun). Extinction factor can be rewritten as follows

$$\nu = \exp\left(-\int_s \beta_{\rm E} \frac{r_{\rm E}^2}{r^2} \frac{ds'}{v}\right) = \exp\left(-\beta_{\rm E} \int_0^t \frac{r_{\rm E}^2}{r^2} dt\right) \ . \qquad \text{(A.12)}$$

As a boundary condition, we assume that neutral atoms far from the heliosphere ($r = \infty$) are at the thermodynamical equilibrium and distribution function is obeyed to the Maxwellian : [*1]

$$\lim_{\vec{r} \to \infty} f(\vec{r}, \vec{v}, t) = n_\infty \left(\frac{m}{2\pi k_{\rm B} T}\right)^{3/2} \exp\left[-\frac{m}{2k_{\rm B}T}\left\{(v_x + V_0)^2 + v_y^2 + v_z^2\right\}\right] \ . \qquad \text{(A.13)}$$

This solution based on the presumption that the interstellar neutral atoms are at thermodynamic equilibrium is so-called "Classical Hot Model" (Lallement et al. 1985).

Then we can solve the distribution of interstellar neutrals $f(\vec{r}, \vec{v}, t)$ by numerical calculations using a Equations (A.12) and (A.13). The key parameter to determine how to solve Equation (A.7) is Knudsen number K_n that is a scale ratio between mean free path and representative physical length scale L. Assuming that the interstellar neutral atom can be regarded as an ideal gas, we obtain the K_n for H atom in the heliosphere is

$$K_n \sim 28.4 \left(\frac{n_{\rm H}}{0.1 \ {\rm cm}^{-3}}\right) \left(\frac{L}{100 \ {\rm AU}}\right)^{-1} \ , \qquad \text{(A.14)}$$

where $n_{\rm H}$ is the density. The collision frequency among H atoms is very low ($\sim 4\%$), and motion of each atom is independent to others. Thus we derive the distribution of the neutral atom using the particle tracking method of each atom.

Figure A.1 shows the distribution of neutral H and He atom distributions on the ecliptic plane within 20 AU from the Sun. The figure is centered at the Sun, and x and y axes are directed winter solstice and spring equinox directions, respectively. The contour is made by averaging the data included in z axis direction $-0.1 < z < 0.1$ AU. Table A.3 shows the parameters of interstellar H and He atoms used for the simulation.

[*1] In this case, we assume that the interstellar neutral flow comes from parallel to the $+x$ direction.

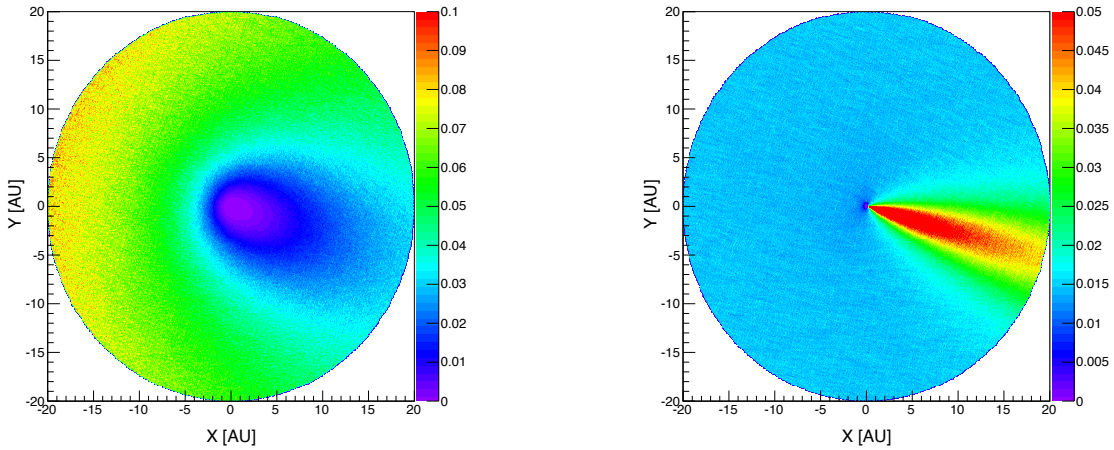

Hydrogen flow (cm^{-3}) Helium flow (cm^{-3})

Figure A.1 Intersterllar neutral atom flows in the heliosphere where the distance from the Sun is < 20 AU.

Table A.2 Interstellar hydrogen and helium parameters.

Parameters		H	He
Density n_∞ cm^{-3} at 100 AU		0.100	0.015
Temperature T K		13000	6300
Relative Velocity V_0 km s^{-1}		21.0	26.2
Upwind Direction $(\lambda, \beta)^*_{\rm HE}$		$(252°.3, 8°.5)$	$(254°.7, 5°.3)$
Ratio of radiation pressure to gravity μ		0.9	0.0
Ionization Rate $\beta_{\rm E}$ s^{-1} at 1AU	Min.	6.6×10^{-7} ($s^\dagger$) / 4.0×10^{-7} ($f^\dagger$)	7.1×10^{-8}
	Max.	$8.4 \times 10^{-7} \sim 6.7 \times 10^{-7}$	1.6×10^{-7}

* Coordinate is shown by helio-ecliptic longitude (λ) and lalitude (β).

† Values are different between slow and fast solar winds.

A.4 Calculating the Intensity of H-SWCX Induced Emission

Using the results of §A.2 and §A.3, charge exchange collision rate per volume of ion X^{Q+} is calculated

$$\begin{aligned} R_{X^{Q+}}(r) &= N_{X^{Q+}}(r) v_{\rm rel} \left(\sigma_{(H,X^{Q+})} n_H(r) + \sigma_{(He,X^{Q+})} n_{He}(r) \right) \\ &\equiv R_{(X^{Q+},H)}(r) + R_{(X^{Q+},He)}(r) \end{aligned} \tag{A.15}$$

where $\vec{v}_{\rm rel}$ is relative velocity between solar wind ion and interstellar neutral atom. Within the termination shock, solar wind ion moves at supersonic speed $V_{\rm SW} \sim 400$ km s^{-1}, while the interstellar neutral moves relatively slow $v_{\rm n} \sim 25$ km s^{-1}. Then the relative velocity between the solar wind ions and the interstellar neutrals is approximately $\vec{v}_{\rm rel} \sim \vec{V}_{\rm SW}$. Coupled with the photon yield of cascade transition, number of photons per second in unit volume $\epsilon_{h\nu}(r)$ is

$$\epsilon_{h\nu}(r) = Y_{(h\nu,H)} R_{(X^{Q+},H)}(r) + Y_{(h\nu,He)} R_{(X^{Q+},He)}(r) \ . \tag{A.16}$$

Finally, we calculate the intensity of H-SWCX induced emission by integrating the emissivity from the observer's site r_0 along the line of sight :

$$I_{h\nu} = \frac{1}{4\pi} \int_{r_0}^{\rm LOS} \epsilon_{h\nu}(r)\, ds \ . \tag{A.17}$$

Here we assume that the integration length is up to $r = 20$ AU from us.

For the H-SWCX induced emission reacted with He, the density distribution is quite uniform except gravitational focusing cone (HeFC). The emissivity roughly has r^{-2} dependence. Figure A.2 shows the cumulative H-SWCX induced OVII emission (0.57 keV) reacted with Hydrogen atom (Koutroumpa et al. 2006). The intensity is expressed as a function of distance from us r. The unit of line intensity is erg s^{-1} cm^{-2} sr^{-1}. Three color shows the intensity toward heliosheath upwind (red), crosswind (black), and the heliotail (blue). The dotted and dashed horizontal lines show the intensity at termination shock $r = 90$ AU and $r = 20$ AU, respectively. Toward each direction, OVII emission within $r = 20$ AU is responsible for 88 % (upwind), 78 % (crosswind), and 65 % (heliotail) of that within termination shock. The intensity differences between integrated to $r = 20$ AU and termination shock are 0.22 erg s^{-1} cm^{-2} sr^{-1} = 0.24 LU (upwind), 0.21 erg s^{-1} cm^{-2} sr^{-1} (crosswind), and 0.16 erg s^{-1} cm^{-2} sr^{-1} (heliotail). Though the fraction of the H-SWCX induced emission with H within 20 AU to that within termination shock toward heliotail is smaller than other direction, major parts of the emission occurs at HeFC. In any direction, about 80 % of the total H-SWCX induced emission within the termination shock is concentrated within 20 AU from us.

Figure A.3 shows the all sky intensity map of H-SWCX induced OVII emission in Galactic coordinate. The center of the Maps is located at $(\ell, b) = (0°, 0°)$, and a unit of the images is shown in LU (= photons s^{-1} cm^{-2} sr^{-1}). The differences among the maps are due to the observer's site. Maps are calculated when the Earth revolves at four equinoxes.

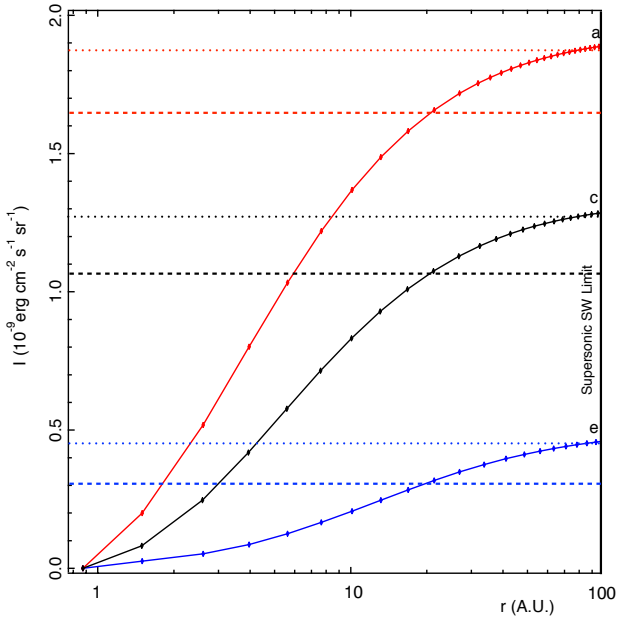

Figure A.2 Cumulative H-SWCX induced OVII emission reacted with Hydrogen atom (Koutroumpa et al. (2006)). Intensity is expressed by a function of distance to the Sun r. Three color shows the intensity toward heliosheath upwind (red), crosswind (black), and the heliotail (blue). The dotted and dashed horizontal lines show the intensity at termination shock and $r = 20$ AU, respectively.

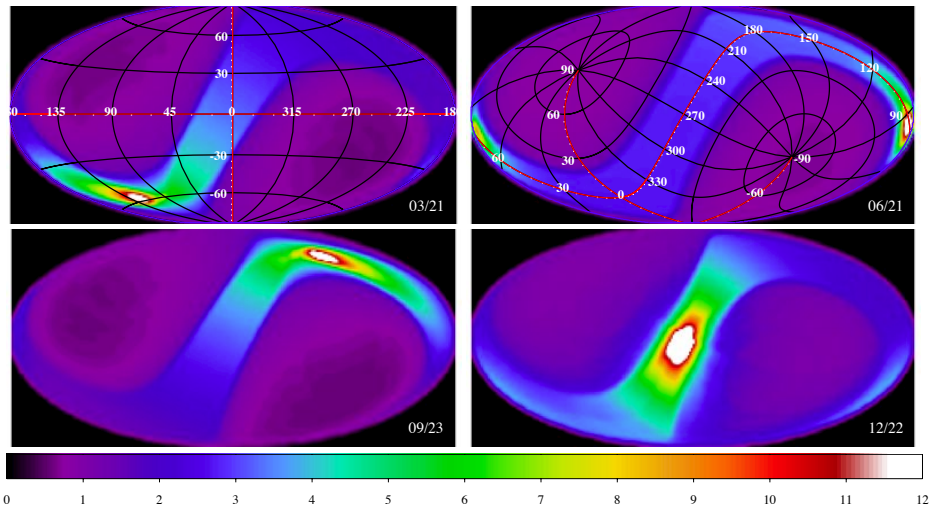

Figure A.3 All sky maps of the H-SWCX induced OVII line intensity seen form the different observer's site at 1 AU from the Sun (Hammer-Aitoff).

B Results of Systematic Analysis toward Anti-Center Region $120° < \ell < 240°$

B.1 Observation

Table shows the observation date, screened exposure, pointing direction in three coordinate system (galactic, equatorial, and ecliptic). The observations are sorted by their galactic latitude. Number ID is same as the Figure 7.1.

Table B.1 Log of Suzaku observations in Chapter 7.

ID. Suzaku Archive Name	Start / End Date	Exposure	Pointing		
	YYYYMMDD hh:mm:ss	ks	Galactic(ℓ, b)	Equatorial(α, δ)	Ecliptic(λ, β)
1. NGC4395	20070602 14:30:03 / 20070605 07:09:24	83.7	(162°.546, 81°.552)	(186°.411, 33°.488)	(170°.813, 32°.907)
2. VICINITYOFNGC4051	20091219 08:18:11 / 20091221 12:20:14	79.6	(150°.131, 70°.304)	(180°.469, 44°.114)	(159°.286, 39°.866)
3. IRAS10565+2448	20071106 15:10:48 / 20071107 11:13:15	37.6	(212°.342, 64°.728)	(164°.858, 24°.598)	(156°.398, 16°.704)
4. MRK417	20070518 15:49:27 / 20070519 13:45:12	38.6	(214°.838, 62°.114)	(162°.364, 22°.904)	(154°.919, 14°.245)
5. NGC3718	20091024 20:23:41 / 20091026 06:08:19	55.2	(146°.879, 60°.214)	(173°.233, 53°.111)	(147°.276, 44°.883)
6. NGC3556	20081125 23:24:06 / 20081127 21:20:11	78.2	(148°.299, 56°.246)	(167°.884, 55°.684)	(141°.585, 45°.293)
7. IC2497	20090418 16:34:31 / 20090420 13:19:19	63.4	(190°.268, 48°.816)	(145°.222, 34°.680)	(135°.807, 19°.600)
8. NGC3079	20080526 20:54:12 / 20080529 10:28:14	51.2	(157°.899, 48°.392)	(150°.498, 55°.613)	(130°.114, 40°.279)
9. RBS1124	20070414 22:53:29 / 20070416 13:53:19	78.9	(125°.396, 46°.317)	(187°.701, 70°.712)	(134°.350, 62°.079)
10. SWIFTJ0911.2+4533	20081025 04:27:32 / 20081027 05:03:14	93.9	(174°.709, 43°.112)	(137°.906, 45°.530)	(126°.030, 27°.901)
11. UGC5101	20060331 04:18:56 / 20060401 08:25:24	44.2	(152°.552, 42°.856)	(143°.841, 61°.318)	(122°.477, 43°.810)
12. IRAS08572+3915	20060414 02:10:04 / 20060415 18:36:19	72.6	(183°.473, 40°.967)	(135°.068, 39°.009)	(126°.118, 21°.051)
13. OJ287QUIESCENT	20070410 19:47:00 / 20070413 11:10:19	86.7	(206°.877, 35°.788)	(133°.690, 20°.048)	(130°.506, 2°.540)
14. J081618.99+482328.4	20090327 02:13:16 / 20090329 02:16:19	84.6	(171°.018, 33°.698)	(124°.077, 48°.384)	(114°.888, 27°.847)
15. HD72779	20091106 07:47:25 / 20091107 22:50:12	64.0	(205°.512, 31°.338)	(128°.831, 19°.592)	(126°.214, 0°.901)
16. 1RXSJ062518.2+73343	20080414 00:55:55 / 20080415 03:00:24	46.6	(140°.868, 24°.125)	(96°.330, 73°.567)	(92°.792, 50°.189)
17. SWIFTJ0746.3+2548	20051104 08:35:29 / 20051106 14:04:15	92.9	(194°.521, 22°.919)	(116°.616, 25°.879)	(113°.853, 4°.617)
18. MKN3	20051022 02:02:09 / 20051024 06:26:14	63.9	(143°.283, 22°.715)	(93°.881, 71°.048)	(91°.869, 47°.633)
19. SN2005KD	20080412 21:22:19 / 20080414 00:50:14	48.5	(136°.850, 14°.247)	(60°.855, 71°.716)	(76°.348, 49°.655)
20. SWIFTJ0318.7+6828	20070922 10:46:17 / 20070924 03:00:14	73.5	(135°.697, 9°.373)	(49°.433, 68°.539)	(69°.164, 48°.014)
21. GALACTICDISC3-1	20100118 20:02:08 / 20100120 00:32:24	51.7	(123°.854, 5°.120)	(15°.309, 67°.974)	(51°.795, 54°.207)
22. ANTICENTER2	20080801 00:17:23 / 20080802 20:11:19	75.8	(122°.990, 0°.040)	(12°.987, 62°.911)	(45°.277, 50°.907)
23. SUAUR	20070827 04:06:45 / 20070828 18:00:19	48.5	(172°.515, −7°.929)	(74°.000, 30°.570)	(76°.137, 7°.898)
24. SWIFTJ0444.1+2813	20080910 17:13:03 / 20080912 15:08:12	69.0	(172°.681, −11°.382)	(71°.028, 28°.279)	(73°.271, 5°.934)
25. SWIFTJ0505.7-2348	20060401 22:12:36 / 20060404 02:55:14	64.0	(225°.007, −33°.160)	(76°.427, −23°.908)	(71°.841, −46°.495)
26. RBS315	20060725 19:36:03 / 20060727 00:58:19	37.9	(151°.731, −38°.744)	(36°.250, 18°.840)	(40°.065, 4°.225)
27. SWIFTJ0255.2-0011	20070123 14:54:10 / 20070126 05:30:25	44.6	(175°.954, −49°.917)	(43°.816, −0°.240)	(41°.284, −16°.215)
28. NGC1052	20070716 10:21:12 / 20070718 21:05:24	81.9	(181°.911, −57°.928)	(40°.231, −8°.213)	(35°.030, −22°.665)
29. IGRJ01528	20090625 00:48:41 / 20090626 03:25:24	40.8	(157°.352, −62°.145)	(28°.202, −3°.447)	(24°.929, −14°.052)
30. NGC788	20080713 00:50:57 / 20080714 01:14:24	42.8	(165°.155, −63°.771)	(30°.262, −6°.762)	(25°.674, −17°.885)
31. IRASF01475-0740	20080714 01:19:09 / 20080715 07:15:19	52.5	(160°.699, −65°.861)	(27°.488, −7°.377)	(22°.749, −17°.451)
32. ARC_BACKGROUND	20081230 06:07:54 / 20090104 08:19:24	126.9	(240°.487, −66°.023)	(39°.206, −35°.728)	(20°.765, −47°.720)
33. NGC720	20051230 08:49:00 / 20060104 13:30:22	74.7	(173°.016, −70°.355)	(28°.253, −13°.736)	(20°.940, −23°.626)

Table B.2 Log of referred Suzaku observations in Chapter 7.

ID. Suzaku Archive Name	Start / End Date	Exposure	Pointing		
	YYYYMMDD hh:mm:ss	ks	Galactic(ℓ, b)	Equatorial(α, δ)	Ecliptic(λ, β)
R1. MRK_421_OFFSET	20091109 01:34:20 / 20091110 19:25:07	64.3	(180°.504, 65°.696)	(166°.803, 37°.734)	(152°.018, 29°.319)
R2. GRB060105	20060105 12:12:52 / 20060106 12:00:18	34.9	(75°.858, 64°.906)	(217°.588, 42°.067)	(194°.208, 52°.640)
R3. MRK_421_OFFSET	20091111 10:45:08 / 20091113 07:37:24	74.5	(179°.319, 64°.355)	(165°.384, 38°.630)	(150°.413, 29°.628)
R4. LOCKMANHOLE	20051114 05:41:37 / 20051115 19:55:18	61.7	(148°.982, 53°.146)	(163°.406, 57°.612)	(137°.147, 45°.553)
R5. HIGH_LAT._DIFFUSE_A	20060214 07:01:24 / 20060215 23:08:14	53.2	(68°.417, 44°.392)	(163°.406, 57°.611)	(228°.836, 63°.559)
R6. NEP	20050902 14:43:43 / 20050904 15:00:14	58.7	(95°.793, 28°.663)	(272°.823, 66°.017)	(335°.682, 88°.741)
R7. NEP	20060210 06:08:12 / 20060212 02:00:24	16.5	(95°.793, 28°.663)	(272°.823, 66°.017)	(335°.682, 88°.741)
R8. LOW_LATITUDE_97-10	20080415 03:10:45 / 20080416 21:20:14	40.8	(96°.614, 10°.409)	(311°.808, 60°.111)	(0°.704, 70°.596)
R9. ANTICENTER	20070422 20:39:20 / 20070425 10:04:24	53.0	(235°.000, 0°.004)	(113°.336, −19°.531)	(119°.458, −40°.613)
R10. LOW_LATITUDE_86-21	20070509 01:56:32 / 20070510 23:55:14	57.0	86°.004, −20°.790)	(332°.317, 30°.217)	(347°.608, 38°.421)
R11. VICINITY_OF_LMC X-3	20060317 14:25:12 / 20060319 22:00:12	56.1	(273°.387, −32°.642)	(83°.484, −63°.886)	(41°.413, −86°.181)
R12. MBM12	20060203 23:02:29 / 20060206 15:30:18	68.0	(159°.189, −34°.469)	(44°.004, 20°.048)	(47°.251, 2°.611)
R13. MBM12_OFF-CLOUD	20060206 15:33:59 / 20060208 14:50:19	51.0	(157°.339, −36°.818)	(41°.321, 18°.335)	(44°.483, 2°.252)
R14. SKY_53.3_-63.4	20060303 20:52:00 / 20060306 08:01:19	59.2	(278°.628, −45°.308)	(53°.240, −63°.455)	(354°.160, −74°.404)
R15. SKY_50.0_-62.4	20060301 16:56:01 / 20060302 22:29:14	59.6	(278°.676, −47°.081)	(50°.051, −62°.433)	(354°.787, −72°.639)
R16. VICINITY_OF_PKS_2155-1	20080429 18:32:39 / 20080502 08:30:08	51.1	(17°.169, −51°.867)	(329°.237, −30°.528)	(320°.679, −16°.905)
R17. VICINITY_OF_PKS_2155-2	20080502 08:31:41 / 20080504 17:30:19	56.3	(18°.229, −52°.620)	(330°.186, −29°.965)	(321°.689, −16°.674)
R18. HIGH_LAT._DIFFUSE_B	20060217 22:24:49 / 20060220 12:30:24	29.7	(272°.403, −58°.273)	(38°.747, −52°.277)	(4°.398, −61°.406)

B.2 Data Reduction

We use the XIS1 cleaned event files that are processed with standard data screening criteria. To avoid high energy particles penetration due to the low Earth's magnetic field, we extracted the data when Cut Off Rigidity (COR2) was larger than 6 GV c^{-1}.

B.2.1 Removal of Point Sources

Point sources are identified on the basis of the Chandra or XMM-Newton XAssist catalog (Ptak & Griffiths (2003)). The angular resolution of these satellites are much better than that of Suzaku : HPD is 0.5 arcsec (Chandra) and 15 arcsec (XMM), respectively. There are no X-ray source catalog toward the FOV of ID 21, 22 , and 32. Thus, we identify the point sources from these observations by eye. Figures show the images of XIS 1 in 0.4–5.0 keV band. Vignetting effect of the XRT is corrected by assuming a flat sky image with a monochromatic energy photon at 2.5 keV. Point sources were removed with circular regions centered at the source position. They are represented by the magenta circles in the figures. Radius of every circle is larger than $1'.5$ in which ~ 60 % of source photons are included according to the on-axis XRT-I1 PSF (see Figure 3.1.2).

B.2.2 Reduction of Geocoronal SWCX Induced Emission

We removed these observations for the spectral analysis when the value of solar wind proton flux obtained by the product of its density and bulk velocity was larger than 4.0×10^8 cm^{-2}s^{-1} (Yoshino et al. (2009)). This proton flux threshold is also used in §5 and §6.

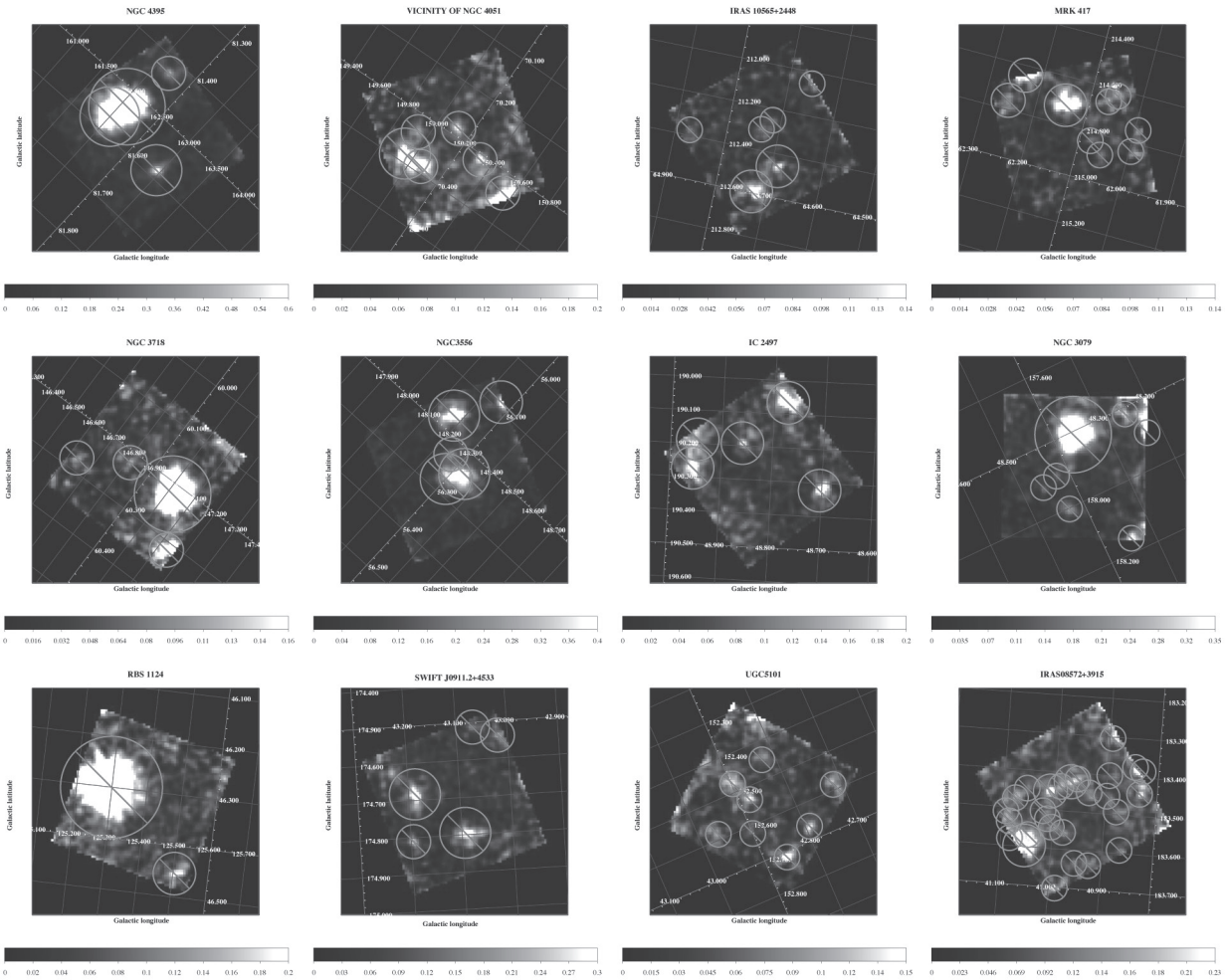

Figure B.1 XIS1 images toward various line of sights in 0.4–5.0 keV band [arbitrary unit]. Images are shown in Galactic coordinate.

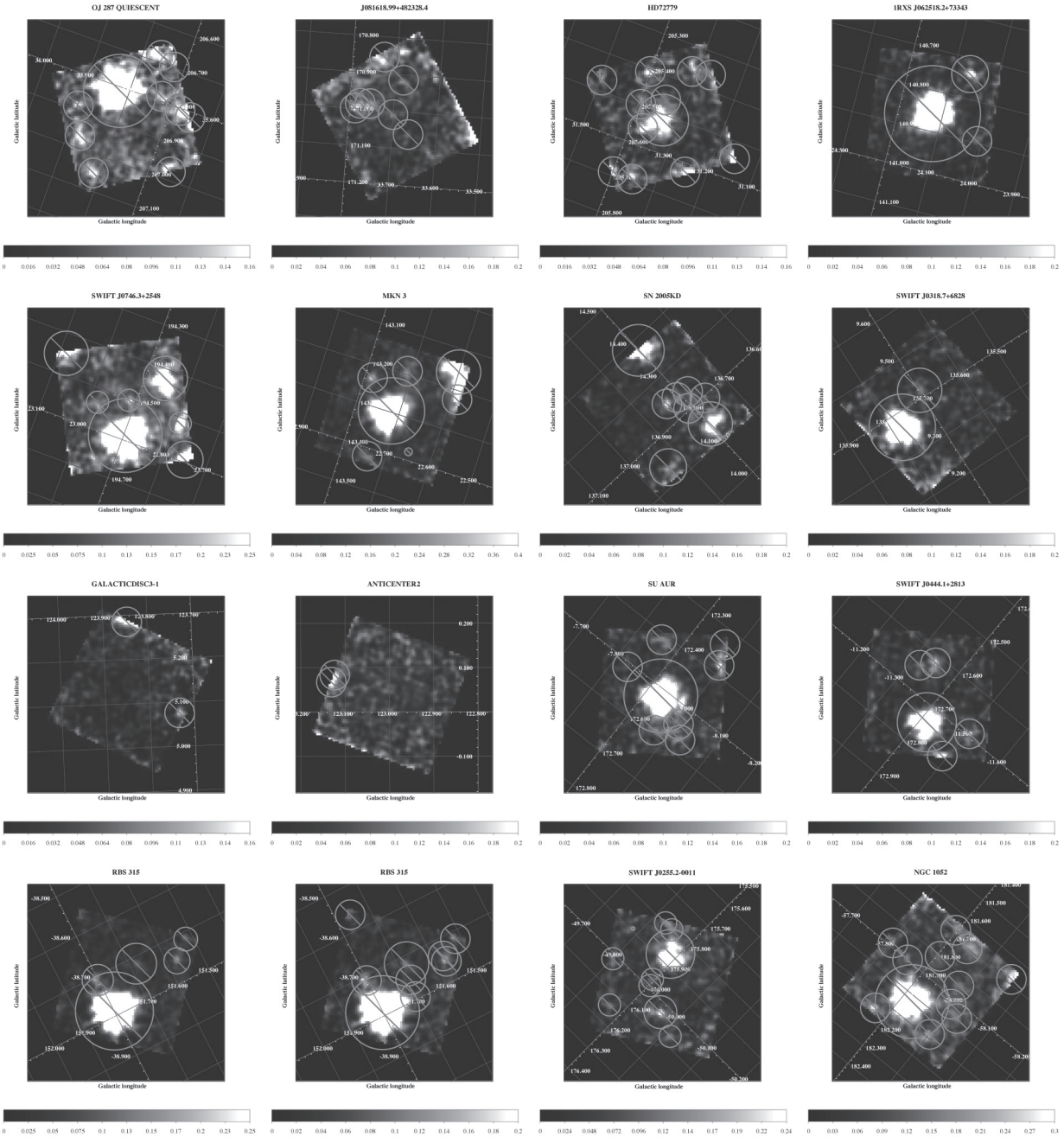

Figure B.2 (Continued)

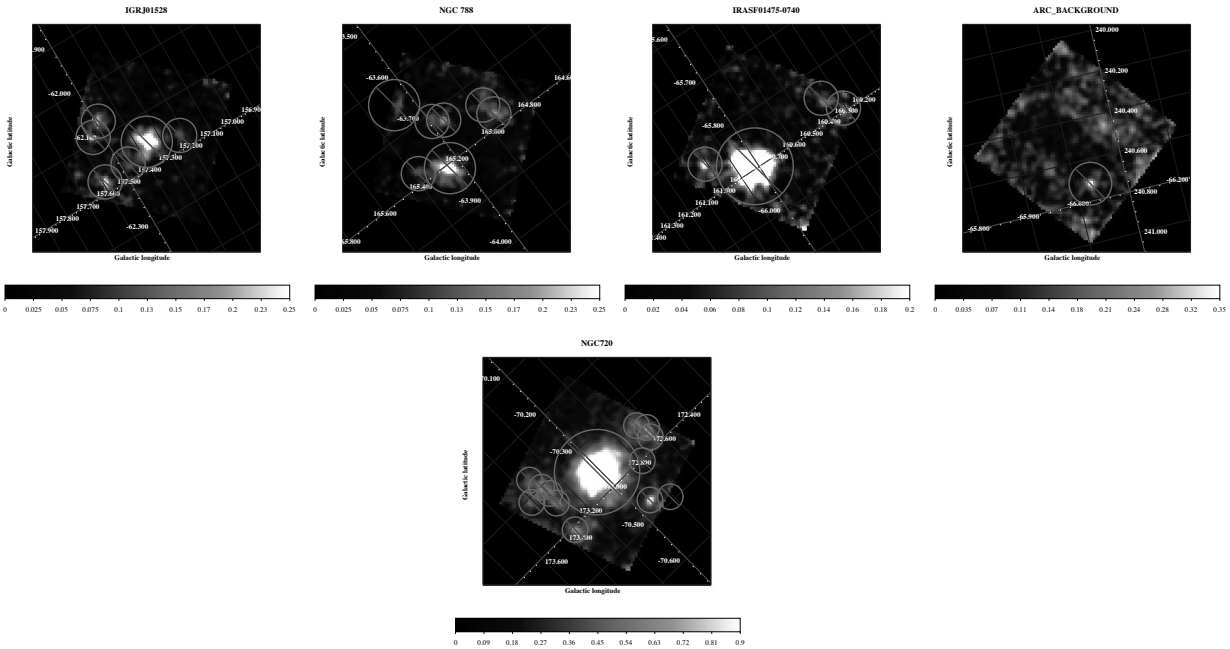

Figure B.3 (Continued)

B.3 Spectral Fitting

Method of spectral fitting same as previous sections. The neutral hydrogen column density $N_{\rm H}$ is fixed at the LAB survey (Kalberla et al. (2005)).

In the observations toward low galactic latitude direction $|b| < 10^\circ$ (ID 20, 21, 22, 23), emission from the Galactic halo is blocked by the strong photoelectric absorption by dense neutral gas. We omit the halo emission from the fitting model. However, we added the emission model of the superpositions of unresolved faint young dM stars instead of the halo. This component is first discovered from the observation toward Anti-Galactic center at $(\ell, b) = (235^\circ, 0^\circ)$ with Suzaku (Masui et al. (2009)). The emission from unresolved dM stars is expressed as the non-absorbed thin thermal plasma with temperature $kT \sim 0.8$ keV in CIE. In addition, two bright emission lines are confirmed from 1 to 2 keV in ID 22. One of the line is thought to be MgXIII emission at 1.34 keV and the other is the instrumental line of SiI at 1.74 keV from the CCD wafer. We insert two gaussians at these energies.

Table B.3 to B.3 are the results of spectral fitting with the above model and Figure to show the spectra with their best-fit models. The first row of each observation shows the results with Galactic halo + double broken power laws CXB + (LB+SWCX) models, and the second one shows the estimation of OVII and OVIII emissions by inserting two gaussians at these energies instead of the oxygen abundances of plasma component set to zero. The resultant χ^2 values were generally good (reduced χ^2 is 0.95 – 1.39 for 71 – 193 degrees of freedom).

In ID 1, 4, 9, 12, 16, 24, 26, and 31, the existence of the Galactic halo component is not significant, and it is difficult to determine the temperatures and normalization of it. We fix the temperature of the halo at $kT = 0.222$ (keV) which is derived from Yoshino et al. (2009).

In ID 3, 5, 15, 20, 27, and 30, the best-fit temperature of the Galactic halo is higher than its typical value of $kT \sim 0.2$ keV of other observations. These observations requires bright Fe-L emissions at $0.7 \sim 0.9$ keV, NeIX at 0.91 keV, and NeX at 1.02 keV to reproduce their spectra. Therefore the halo temperature is raised to emit these lines. These features are also confirmed in Yoshino et al. (2009).

Table B.3 Results of spectral fitting with Galactic halo or unresolved dM star + double broken power laws CXB + (LB+SWCX) models.

component	$N_{\rm H}^{*}$	Galactic Halo / dM Star		CXB	LB+SWCX	OVII	OVIII	χ^2/d.o.f
model		*phabs* (APEC) /APEC*		*phabs* (bknpwls)*[†]	*APEC*	*gaussian*[‡]	*gaussian*[‡]	
parameter		kT	norm.	norm.	norm.	norm.	norm.	
unit	$\rm cm^{-2}$	keV	[§]	[‖]	[‖]	[♯]	[♯]	
1[††]	1.87	0.222 (fixed)	< 1.3	$5.8^{+0.5}_{-0.5}$	$30.8^{+4.9}_{-4.9}$	–	–	124.3/112
			< 1.8	$5.9^{+0.5}_{-0.5}$	$29.2^{+9.1}_{-9.2}$	$5.13^{+0.91}_{-0.72}$	< 0.55	122.3/110
2	1.14	$0.273^{+0.068}_{-0.050}$	$2.2^{+1.2}_{-0.7}$	$4.9^{+0.4}_{-0.5}$	$29.7^{+5.8}_{-7.5}$	–	–	107.2/120
		0.273 (fixed)	$2.8^{+1.1}_{-0.9}$	$4.9^{+0.6}_{-0.6}$	$41.4^{+13.9}_{-14.2}$	$5.10^{+0.69}_{-1.71}$	$1.01^{+0.32}_{-0.91}$	107.9/119
3	1.08	$0.740^{+0.123}_{-0.169}$	$1.2^{+0.4}_{-0.4}$	$1.7^{+0.7}_{-0.7}$	$35.2^{+5.6}_{-5.6}$	–	–	89.7/82
		0.740 (fixed)	$1.3^{+0.3}_{-0.3}$	$1.7^{+0.5}_{-0.7}$	$36.1^{+13.5}_{-12.4}$	$5.11^{+1.15}_{-0.99}$	$0.84^{+0.55}_{-0.52}$	83.3/81
4[††]	1.82	0.222 (fixed)	$2.4^{+1.1}_{-1.1}$	$3.7^{+0.6}_{-0.6}$	$20.7^{+6.1}_{-6.1}$	–	–	60.9/82
			$2.3^{+2.4}_{-1.7}$	$3.8^{+0.6}_{-0.5}$	$19.6^{+8.2}_{-16.1}$	$4.62^{+1.04}_{-0.99}$	$0.77^{+0.53}_{-0.51}$	60.3/80
5	1.05	$0.507^{+0.279}_{-0.298}$	$0.6^{+1.3}_{-0.4}$	$4.4^{+0.6}_{-0.6}$	$25.5^{+5.9}_{-8.7}$	–	–	152.7/131
		0.507 (fixed)	$0.7^{+0.4}_{-0.4}$	$4.3^{+0.6}_{-0.6}$	$30.0^{+13.8}_{-13.5}$	$3.67^{+1.29}_{-0.95}$	< 0.88	152.5/130
6	0.78	$0.287^{+0.110}_{-0.065}$	$1.7^{+1.0}_{-0.7}$	$2.8^{+0.5}_{-0.5}$	$19.0^{+5.4}_{-6.6}$	–	–	103.0/106
		0.287 (fixed)	$2.1^{+0.8}_{-0.7}$	$2.8^{+0.5}_{-0.5}$	$22.4^{+10.0}_{-9.8}$	$3.15^{+0.90}_{-0.80}$	$0.38^{+0.57}_{-0.36}$	103.8/105
7	1.05	$0.296^{+0.382}_{-0.087}$	$1.5^{+1.3}_{-1.0}$	$5.1^{+0.5}_{-0.5}$	$27.3^{+7.5}_{-8.3}$	–	–	144.0/131
		0.296 (fixed)	$1.7^{+0.7}_{-0.8}$	$5.1^{+0.5}_{-0.5}$	$30.7^{+12.4}_{-11.6}$	$4.76^{+0.64}_{-1.42}$	$0.43^{+0.71}_{-0.33}$	144.8/130
8	0.88	$0.233^{+0.057}_{-0.043}$	$4.1^{+3.2}_{-1.7}$	$3.5^{+0.6}_{-0.6}$	$28.2^{+10.5}_{-14.4}$	–	–	111.4/98
		0.233 (fixed)	$5.1^{+1.9}_{-1.7}$	$3.5^{+0.6}_{-0.6}$	$42.9^{+14.9}_{-14.1}$	$5.53^{+1.02}_{-1.33}$	$1.76^{+0.46}_{-0.87}$	110.5/97
9[††]	1.54	0.222 (fixed)	$1.5^{+0.8}_{-0.8}$	$4.9^{+0.5}_{-0.5}$	$19.0^{+4.6}_{-4.6}$	–	–	173.3/135
			$3.3^{+1.7}_{-1.6}$	$4.9^{+0.5}_{-0.5}$	$11.2^{+8.4}_{-8.5}$	$4.39^{+0.65}_{-0.88}$	$0.01^{+0.48}_{-0.01}$	167.0/133
10	1.23	$0.259^{+0.071}_{-0.063}$	$2.0^{+1.8}_{-0.8}$	$4.4^{+0.4}_{-0.4}$	$16.1^{+5.5}_{-8.8}$	–	–	146.5/127
		0.259 (fixed)	$2.7^{+1.2}_{-0.9}$	$4.4^{+0.6}_{-0.5}$	$17.7^{+11.1}_{-11.1}$	$3.46^{+0.56}_{-1.37}$	$0.87^{+0.27}_{-0.80}$	149.8/126
11	3.01	$0.238^{+0.065}_{-0.057}$	$3.0^{+3.2}_{-1.2}$	$4.2^{+0.6}_{-0.6}$	$11.6^{+5.8}_{-11.4}$	–	–	100.5/118
		0.238 (fixed)	$4.4^{+1.7}_{-1.4}$	$4.2^{+0.7}_{-0.6}$	$8.8^{+8.6}_{-7.8}$	$3.13^{+0.57}_{-0.86}$	$0.97^{+0.25}_{-0.70}$	99.4/117
12[††]	2.06	0.222 (fixed)	< 1.3	$5.1^{+0.5}_{-0.5}$	$26.9^{+4.2}_{-4.2}$	–	–	104.3/96
			< 1.9	$5.1^{+0.5}_{-0.4}$	$26.8^{+6.1}_{-9.2}$	$4.57^{+0.70}_{-0.67}$	< 0.52	103.7/94

Table B.4 (Continued).

component	$N_{\rm H}^{*}$	Galactic Halo / dM Star		CXB	LB+SWCX	OVII	OVIII	χ^2/d.o.f
model		*phabs* (APEC) /APEC*		*phabs* (bknpwls)*†	*APEC*	*gaussian*‡	*gaussian*‡	
parameter		kT	norm.	norm.	norm.	norm.	norm.	
unit	cm^{-2}	keV	§	‖	‖	♯	♯	
13	2.49	$0.172^{+0.072}_{-0.051}$	$2.5^{+5.4}_{-2.2}$	$4.7^{+0.5}_{-0.5}$	$9.2^{+8.6}_{-9.2}$	–	–	82.6/85
		0.172 (fixed)	< 3.0	$4.7^{+0.4}_{-0.5}$	$17.8^{+9.9}_{-10.1}$	$2.50^{+0.74}_{-0.72}$	$0.80^{+0.41}_{-0.42}$	75.4/84
14	4.84	$0.272^{+0.045}_{-0.057}$	$2.3^{+1.5}_{-0.7}$	$5.2^{+0.4}_{-0.4}$	$9.7^{+3.8}_{-6.4}$	–	–	113.2/112
		0.272 (fixed)	$2.4^{+0.9}_{-0.9}$	$5.2^{+0.4}_{-0.4}$	$25.6^{+8.8}_{-8.8}$	$1.08^{+0.68}_{-0.66}$	$1.08^{+0.41}_{-0.39}$	100.3/111
15	2.59	$0.621^{+0.118}_{-0.173}$	$1.4^{+0.4}_{-0.4}$	$1.8^{+0.6}_{-0.6}$	$30.5^{+5.7}_{-5.7}$	–	–	91.1/78
		0.621 (fixed)	$1.4^{+0.4}_{-0.4}$	$1.8^{+0.7}_{-0.6}$	$37.9^{+14.3}_{-14.7}$	$4.58^{+0.86}_{-1.67}$	$0.70^{+0.50}_{-0.70}$	88.8/77
16††	7.34	0.222 (fixed)	< 2.6	$4.8^{+0.8}_{-0.8}$	$15.7^{+6.4}_{-6.4}$	–	–	70.2/74
			< 1.2	$4.8^{+0.8}_{-0.8}$	$26.4^{+14.3}_{-14.5}$	$2.16^{+1.11}_{-0.97}$	< 0.99	68.2/72
17	4.41	$0.227^{+0.036}_{-0.031}$	$3.9^{+1.8}_{-1.1}$	$4.4^{+0.5}_{-0.5}$	$16.0^{+4.4}_{-5.7}$	–	–	131.5/122
		0.227 (fixed)	$5.3^{+1.3}_{-1.5}$	$4.5^{+0.5}_{-0.5}$	$17.4^{+5.1}_{-5.3}$	$3.78^{+0.49}_{-0.49}$	$1.10^{+0.24}_{-0.39}$	131.3/121
18	9.68	$0.222^{+0.041}_{-0.039}$	$4.6^{+3.6}_{-1.5}$	$2.2^{+0.6}_{-0.6}$	$15.9^{+3.9}_{-6.5}$	–	–	112.4/112
		0.222 (fixed)	$6.4^{+1.8}_{-1.9}$	$2.2^{+0.6}_{-0.6}$	$16.4^{+4.8}_{-4.9}$	$3.47^{+0.52}_{-0.46}$	$0.81^{+0.32}_{-0.27}$	114.3/111
19	13.00	$0.399^{+0.388}_{-0.104}$	$1.3^{+0.7}_{-0.6}$	$4.2^{+0.6}_{-0.6}$	$9.8^{+4.7}_{-4.8}$	–	–	116.6/102
		0.399 (fixed)	$1.3^{+0.5}_{-0.3}$	$4.2^{+0.7}_{-0.6}$	$21.4^{+7.1}_{-16.6}$	$1.28^{+0.97}_{-0.73}$	< 0.76	116.1/101
20**	30.80	$0.646^{+0.153}_{-0.190}$	$0.7^{+0.2}_{-0.2}$	$5.4^{+0.6}_{-0.6}$	$4.7^{+2.5}_{-2.5}$	–	–	132.2/120
		0.646 (fixed)	$0.7^{+0.2}_{-0.2}$	$5.5^{+0.6}_{-0.7}$	$5.1^{+8.0}_{-5.1}$	$0.68^{+0.50}_{-0.48}$	$0.07^{+0.27}_{-0.07}$	132.1/119
21**	42.60	$0.913^{+0.095}_{-0.161}$	$1.2^{+0.3}_{-0.3}$	$5.4^{+0.7}_{-0.7}$	$16.1^{+3.6}_{-3.6}$	–	–	138.9/138
		0.913 (fixed)	$1.2^{+0.2}_{-0.2}$	$5.4^{+0.7}_{-0.6}$	$33.2^{+8.9}_{-10.5}$	$1.76^{+0.48}_{-1.07}$	$0.60^{+0.25}_{-0.50}$	126.6/137
22**	74.00	$0.940^{+0.027}_{-0.033}$	$4.4^{+0.3}_{-0.3}$	$4.6^{+0.6}_{-0.7}$	$9.9^{+3.1}_{-3.0}$	–	–	230.8/193
		0.940 (fixed)	$4.9^{+0.2}_{-0.2}$	$5.0^{+0.6}_{-0.6}$	$9.6^{+6.8}_{-6.8}$	$1.94^{+0.62}_{-0.50}$	$1.26^{+0.26}_{-0.37}$	250.4/195
23**	24.80	$0.996^{+0.074}_{-0.100}$	$2.2^{+0.6}_{-0.6}$	$6.6^{+1.0}_{-1.0}$	$15.3^{+4.2}_{-4.2}$	–	–	87.2/89
		0.996 (fixed)	$2.2^{+0.5}_{-0.4}$	$6.6^{+1.0}_{-0.8}$	$24.3^{+7.9}_{-16.0}$	$1.93^{+0.93}_{-0.76}$	$0.57^{+0.46}_{-0.45}$	84.8/88
24††	17.70	0.222 (fixed)	$0.0^{+0.8}_{-0.0}$	$3.4^{+0.5}_{-0.5}$	$6.6^{+3.3}_{-3.3}$	–	–	111.1/93
			< 1.0	$3.4^{+0.5}_{-0.5}$	$7.7^{+10.3}_{-7.7}$	$0.97^{+0.67}_{-0.63}$	< 0.46	110.3/91

Table B.5 (Continued).

component	$N_{\rm H}^{*}$	Galactic Halo / dM Star		CXB	LB+SWCX	OVII	OVIII	χ^2/d.o.f
model		*phabs* (APEC)*	*/APEC*	*phabs* (bknpwls)*†	*APEC*	*gaussian*‡	*gaussian*‡	
parameter		kT	norm.	norm.	norm.	norm.	norm.	
unit	$\rm cm^{-2}$	keV	§	‖	‖	♯	♯	
25	2.14	$0.281^{+0.088}_{-0.064}$	$1.8^{+1.1}_{-0.7}$	$4.0^{+0.6}_{-0.6}$	$13.3^{+4.2}_{-5.8}$	–	–	114.7/95
		0.281 (fixed)	$2.3^{+0.8}_{-0.9}$	$4.1^{+0.5}_{-0.6}$	$14.7^{+7.7}_{-7.8}$	$2.65^{+0.48}_{-0.79}$	$0.52^{+0.37}_{-0.38}$	115.0/94
26††	9.42	0.222 (fixed)	$0.8^{+1.7}_{-0.8}$	$7.1^{+0.9}_{-0.9}$	$19.1^{+5.7}_{-5.7}$	–	–	72.6/80
			$0.2^{+3.1}_{-0.2}$	$7.3^{+0.8}_{-0.9}$	< 26.1	$3.52^{+0.95}_{-0.96}$	< 0.76	70.2/78
27	5.81	$0.666^{+0.258}_{-0.430}$	$0.7^{+0.4}_{-0.4}$	$2.2^{+0.6}_{-0.7}$	$14.2^{+3.7}_{-3.7}$	–	–	50.4/71
		0.666 (fixed)	$0.7^{+0.4}_{-0.3}$	$2.2^{+0.7}_{-0.6}$	$17.6^{+8.9}_{-9.1}$	$2.21^{+0.56}_{-0.86}$	$0.14^{+0.50}_{-0.14}$	49.7/70
28	2.82	$0.262^{+0.107}_{-0.077}$	$2.1^{+2.7}_{-1.0}$	$5.9^{+0.7}_{-0.7}$	$12.9^{+5.8}_{-10.8}$	–	–	95.7/100
		0.262 (fixed)	$3.1^{+0.9}_{-1.8}$	$5.7^{+0.7}_{-0.6}$	$12.6^{+11.7}_{-10.1}$	$2.55^{+0.88}_{-0.79}$	$0.61^{+0.49}_{-0.47}$	95.8/99
29	2.72	$0.278^{+0.386}_{-0.088}$	$1.5^{+1.9}_{-1.1}$	$5.6^{+0.7}_{-0.7}$	$12.8^{+7.4}_{-9.2}$	–	–	64.7/76
		0.278 (fixed)	$1.7^{+1.3}_{-1.2}$	$5.6^{+0.7}_{-0.7}$	$32.5^{+15.8}_{-17.5}$	$1.25^{+1.41}_{-1.01}$	< 1.17	62.1/75
30	2.13	$0.426^{+0.251}_{-0.155}$	$1.1^{+1.0}_{-0.6}$	$5.4^{+0.7}_{-0.7}$	$26.5^{+5.9}_{-6.5}$	–	–	89.1/98
		0.426 (fixed)	$1.2^{+0.5}_{-0.5}$	$5.3^{+0.7}_{-0.7}$	$43.7^{+13.5}_{-13.4}$	$3.31^{+1.15}_{-1.02}$	< 0.99	84.1/97
31††	2.02	0.222 (fixed)	$0.4^{+1.0}_{-0.4}$	$3.8^{+0.5}_{-0.5}$	$15.5^{+5.6}_{-5.7}$	–	–	80.7/79
			< 1.7	$3.8^{+0.5}_{-0.5}$	$29.3^{+12.0}_{-12.1}$	$1.94^{+0.91}_{-0.92}$	$0.42^{+0.49}_{-0.42}$	75.7/77
32	3.60	$0.253^{+0.068}_{-0.059}$	$1.5^{+1.4}_{-0.6}$	$3.6^{+0.3}_{-0.3}$	$17.7^{+3.8}_{-5.8}$	–	–	130.3/125
		0.253 (fixed)	$1.9^{+0.7}_{-0.8}$	$3.6^{+0.3}_{-0.3}$	$24.3^{+7.3}_{-6.9}$	$2.73^{+0.70}_{-0.41}$	$0.59^{+0.26}_{-0.32}$	129.5/124
33	1.50	$0.330^{+0.037}_{-0.019}$	$7.0^{+0.7}_{-0.9}$	$4.8^{+0.6}_{-0.6}$	$17.4^{+4.4}_{-4.1}$	–	–	131.3/114
		0.330 (fixed)	$7.6^{+0.7}_{-0.7}$	$5.0^{+0.6}_{-0.6}$	$21.4^{+6.5}_{-7.2}$	$3.41^{+0.67}_{-0.52}$	$2.25^{+0.25}_{-0.71}$	138.5/113

* Nutral absorption column density is fixed at the LAB survey results (Kalberla et al. (2005)).

† See details in the text.

‡ See details in the text.

§ The emission measure integrated over the line of sight, i.e. $(1/4\pi)\int n_{\rm e} n_{\rm H} ds$ 10^{14} $\rm cm^{-5}$ $\rm sr^{-1}$.

‖ The unit of the normalization of a power-law component is photons $\rm s^{-1}cm^{-2}keV^{-1}sr^{-1}$@1keV.

♯ The normalization of gaussian component shows the surface brightness whose unit is defined as L.U. (Line Unit) = photons $\rm s^{-1}cm^{-2}sr^{-1}$.

** The contribution from unresolved dM stars are added to the model instead of the Galactic halo. This emission is represented by the unabsorbed thin thermal plasma (Masui et al. (2009)).

†† The existence of the Galactic halo component is not significant. The temperature of the halo is fixed at a typical value of $kT = 0.222$ keV from Yoshino et al. (2009)

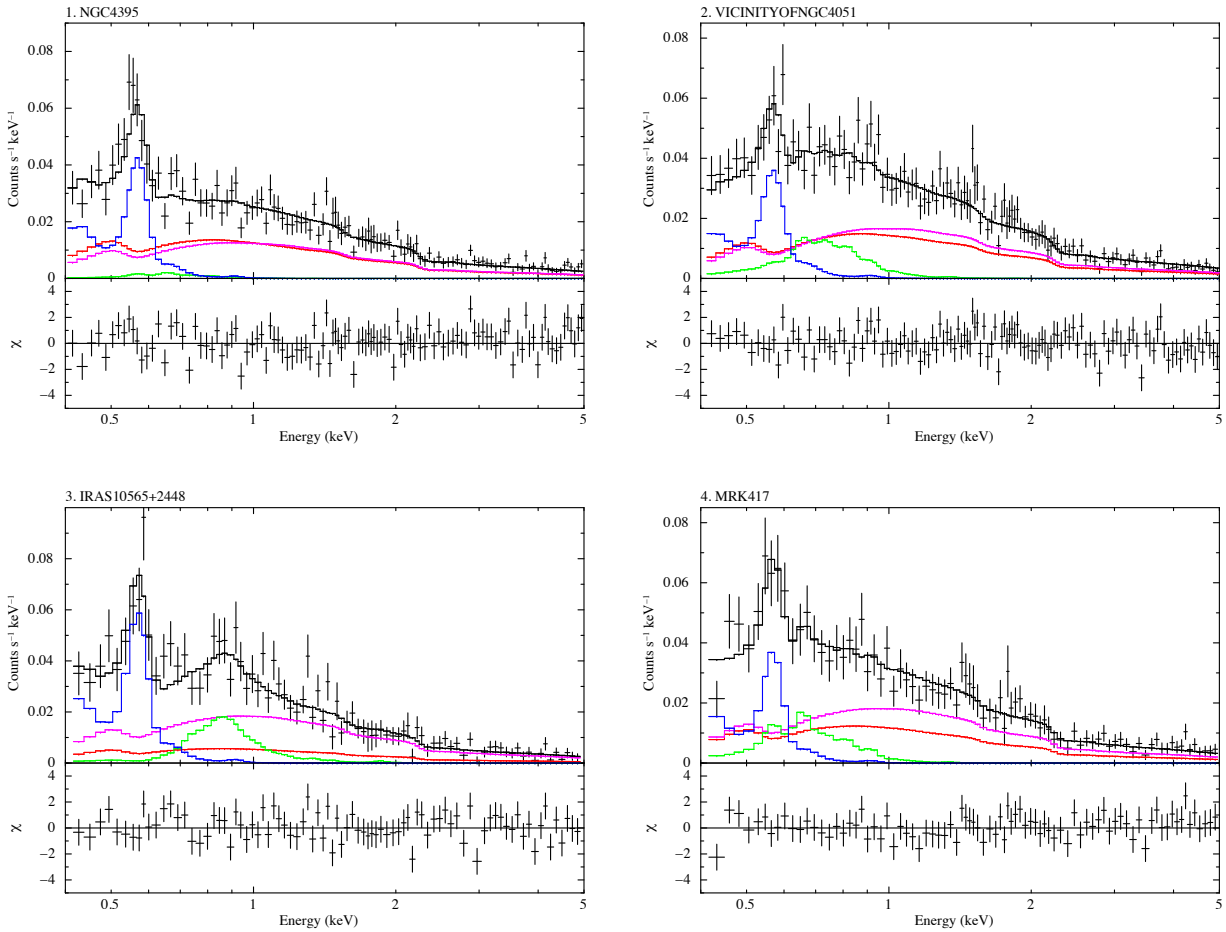

Figure B.4 0.4–5.0 keV Suzaku XIS1 (Back Illuminated CCD) spectra and best fit emission models of the blank fields convolved with the CCD and telescope response (top panel) and residual of the fit (bottom panel). Black crosses show the observed spectra. Step lines show the models with best fit values; total (black), TAE or dM star (green), LHB+SWCX (blue), CXB with $\Gamma = 1.54$ (magenta), and CXB with $\Gamma = 1.96$ (red), respectively.

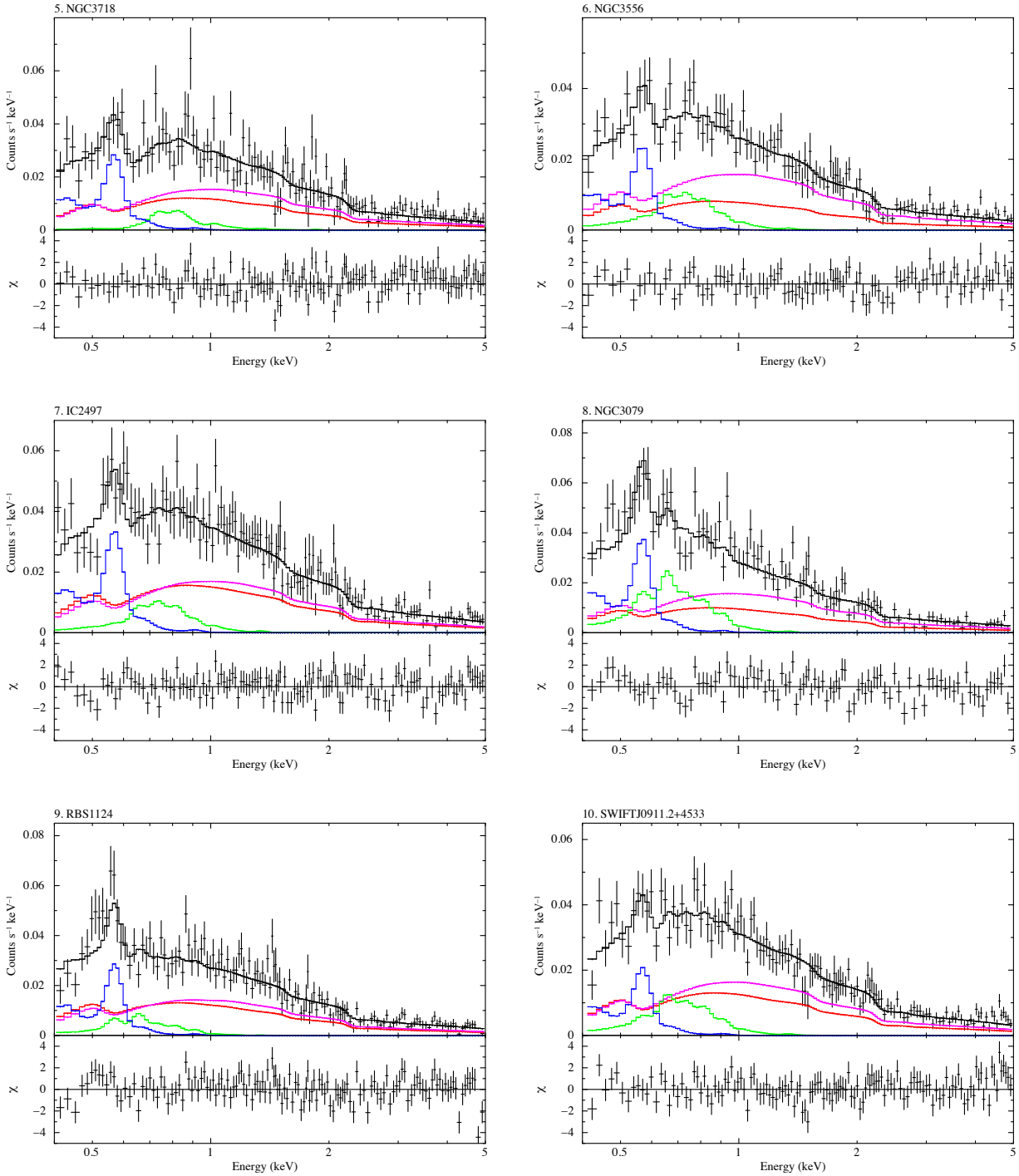

Figure B.5 (Continued)

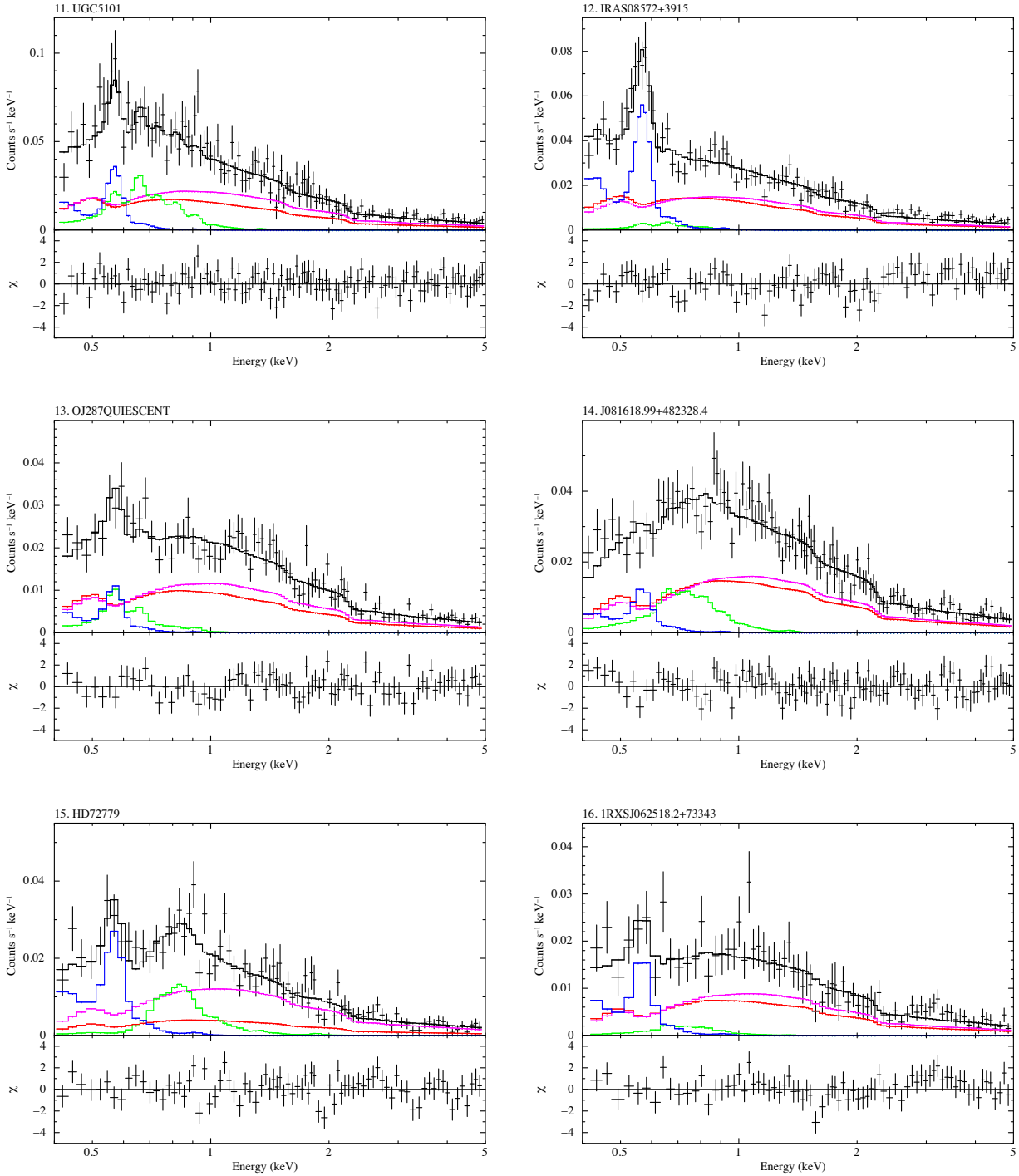

Figure B.6 (Continued)

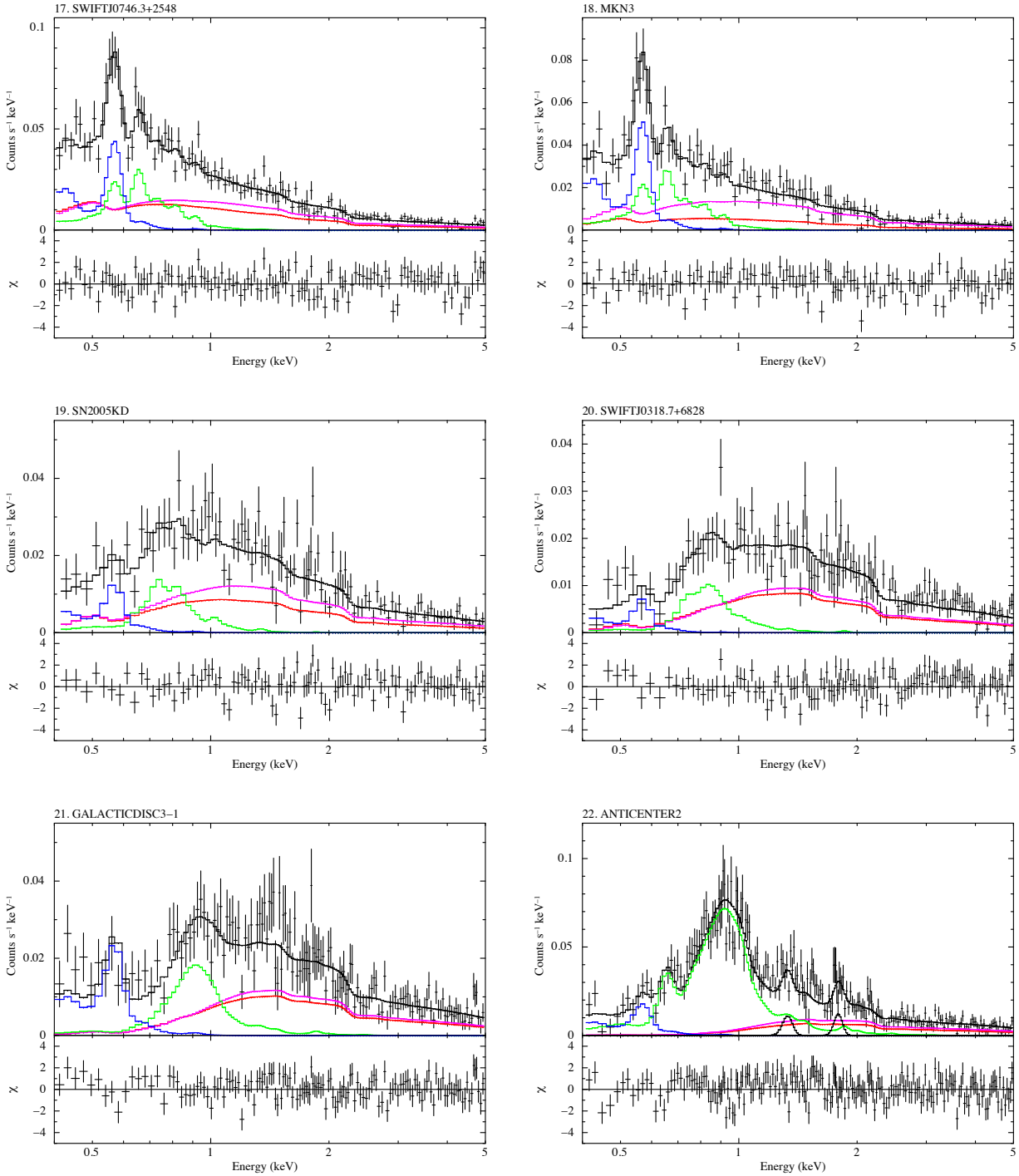

Figure B.7 (Continued)

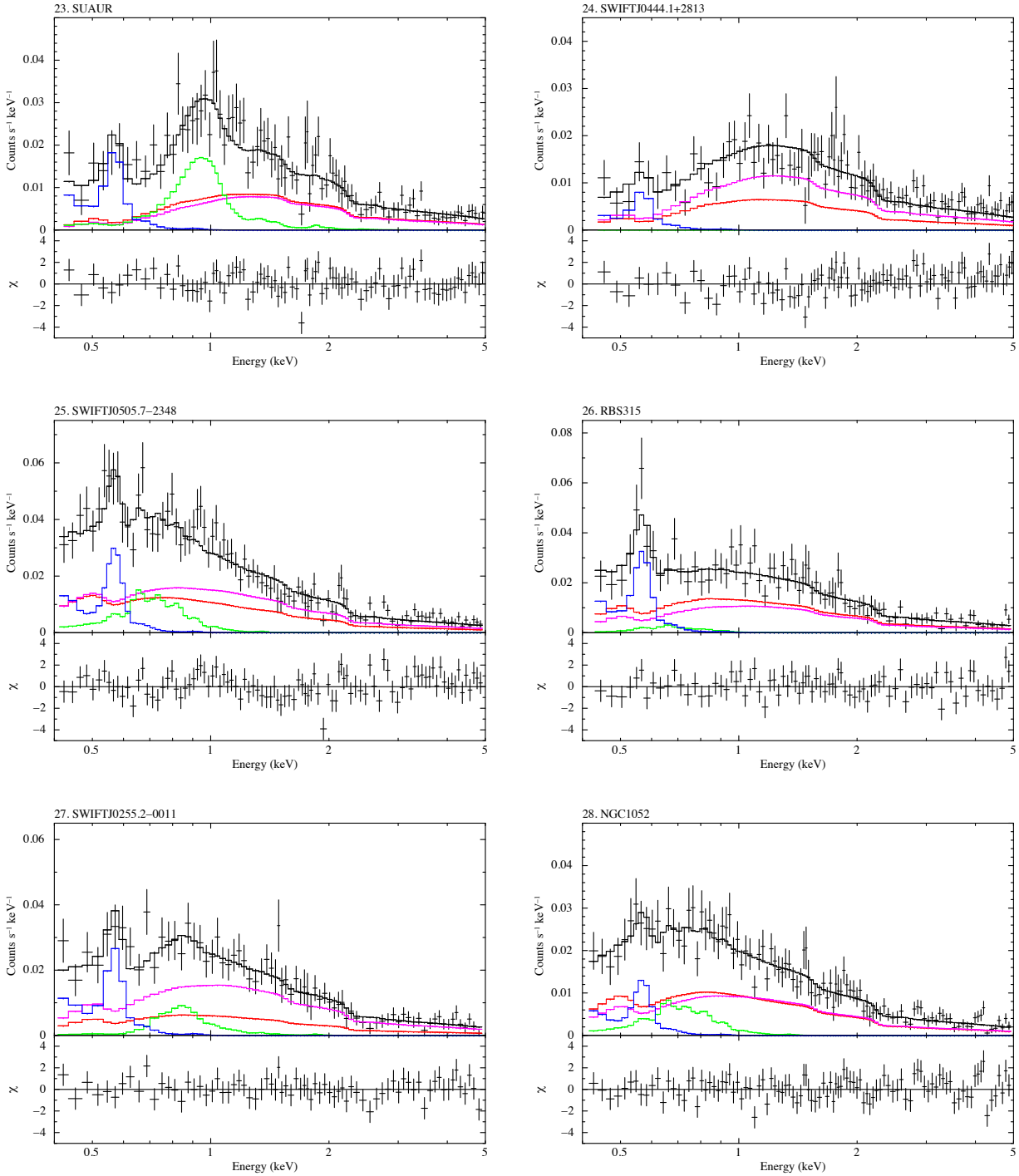

Figure B.8 (Continued)

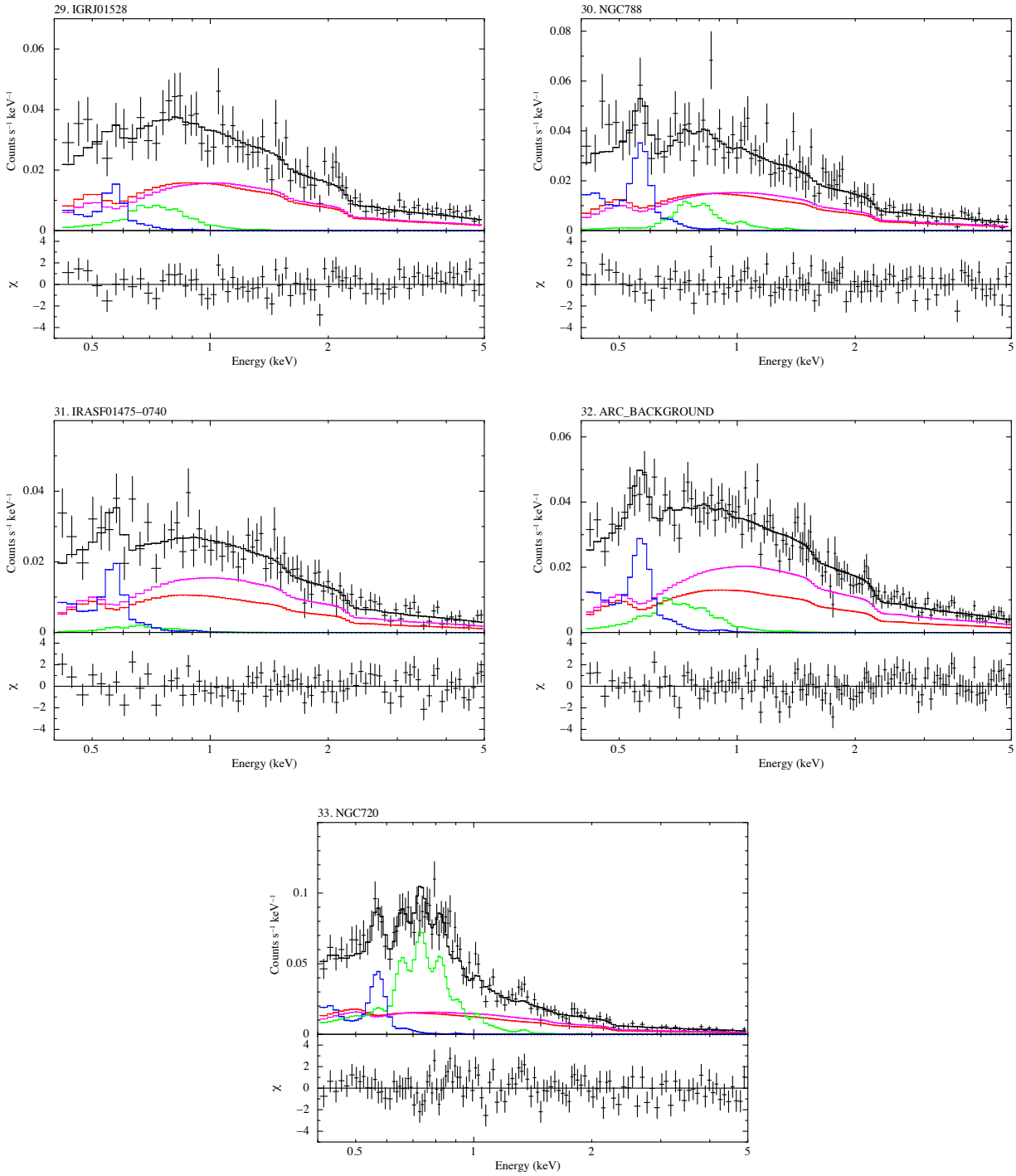

Figure B.9 (Continued)

We also summarize the intensities of OVII and OVIII emission in referred papers in Table B.6. Processes of the data reduction and spectral analysis of them are same as this thesis.

Table B.6 OVII and OVIII emissions observed with Suzaku from Yoshino et al. (2009), Hagihara et al. (2010), and Sakai et al. (in prep.).

ID	$N_{\rm H}$ 10^{20} cm^{-2}	OVII LU	OVIII LU
R1	1.92	4.6 ± 1.1	< 0.4
R2	1.40	$3.6^{+0.9}_{-1.0}$	0.7 ± 0.5
R3	1.92	5.3 ± 1.0	1.7 ± 0.5
R4	0.56	4.1 ± 0.5	0.5 ± 0.3
R5	1.02	4.5 ± 0.6	1.6 ± 0.4
R6	4.40	8.9 ± 0.5	2.8 ± 0.3
R7	4.40	7.0 ± 1.1	2.6 ± 0.7
R8	27.10	$1.7^{+1.3}_{-0.7}$	0.4 ± 0.3
R9	90.00	$2.1^{+0.8}_{-0.6}$	0.9 ± 0.3
R10	7.24	$6.4^{+0.8}_{-0.9}$	1.8 ± 0.5
R11	4.67	6.0 ± 0.7	1.8 ± 0.4
R12	40.00	2.9 ± 0.5	< 0.4
R13	8.74	4.4 ± 0.5	0.6 ± 0.3
R14	4.61	$5.2^{+1.0}_{-0.6}$	1.6 ± 0.3
R15	4.19	9.5 ± 0.7	2.5 ± 0.4
R16	1.76	$5.9^{+0.8}_{-0.9}$	1.3 ± 0.5
R17	1.67	6.3 ± 0.8	$2.5^{+0.4}_{-0.5}$
R18	3.36	2.3 ± 0.7	0.9 ± 0.4

References

Anders, E., & Grevesse, N., 1989, Geochem. Cosmochim. Acta, 53, 197.

Babcock, H. W., 1961, ApJ, 133, 572.

Balucinska-Church, M., & McCammon, D. 1992, ApJ, 400, 2, 699.

Brandt, W., N., & Hasinger, G., 2005, ARA&A, 43, 1, 827.

Breitschwerdt, D., & de Avillez, M. A., 2006, ApJ, 452, 1, 1.

Cox, D. P., & Anderson, P. R., 1982, ApJ, 253, 1, 268.

Cox, D. P., The Local Bubble and Beyond (Berlin: Springer), 1998, ed. Breitschwerdt, D., Freyberg, M. J., & Trumper, J., 121.

Cox, D. P., 2005, ARA&A, 43, 1, 337.

Cravens, T. E., 1997, Geophys. Res. Lett., 24, 105.

Dehnen, W., & Binney, J., 1998 MNRAS, 294, 429.

Dickey, J. M., & Lockman, F. J., 1990, ARA&A, 28, 215.

Dikpati, M. & Charbonneau, P., 1999, ApJ, 518, 1, 508.

Ezoe, Y., Ebisawa, K., Yamasaki, N. Y., Mitsuda, K., Yoshitake, H., Terada, N., Miyoshi, Y., & Fujimoto, R., 2010, PASJ, 62, 981.

Ferriére, K. M., 2001, Reviews of Modern Physics, 73, 4, 1031.

Fujimoto, R., Mitsuda, K., Mccammon, D., Takei, Y., Bauer, M., Ishisaki, Y., Porter, S. F., Yamaguchi, H., Hayashida, K., & Yamasaki, N. Y., 2007, PASJ, 59 SP1, S133.

Gendreau, K., C., et al., PASJ, 1995, 47, L5.

Gloeckler, G, et al., 2004, A&A, 426, 845.

Hagihara, T., Yao, Y., Yamasaki, N. Y., Mitsuda, K., Wang, Q. D., Takei, Y., Yoshino, T., & McCammon, D., 2010, PASJ, 62, 723.

Hasinger, G., Burg, R., Giacconi, R., Hartner, G., Schmidt, M., Trumper, J., & Zamorani, G., 1993, A&A, 275, 1.

Hedin, A. E. 1991, J. Geophys. Res., 96, 1159.

Henley, D, B., & Shelton, R, L., 2008, ApJ, 676, 1, 335.

Henley, D, B., & Shelton, R, L., 2010, ApJS, 187, 2, 388.

Hickox, R. C., & Markevitch, M. 2006., ApJ, 645, 1, 95.

Hodges, R. Richard, Jr., 1994, J. Geophys. Res., 99, A12, 23, 229.

Hurwitz, M., Sasseen, T. P., & Sirk, M. M., 2005, ApJ, 623, 2, 911.

Ishisaki, Y., et al., 2007, PASJ, 59 SP1, S113.

Kimura, S., Mitsuda, K., Yamasaki, Y. N., & Takei, Y, 2009, proceedings of Suzaku Conference.

Kalberla, P. M. W., Burton, W. B., Hartmann, Dap, Arnal, E. M., Bajaja, E., Morras, R., & Pöppel, W. G. L., 2005, A&A, 440, 775.

Kerp, J., Burton, W. B., Egger, R., Freyberg, M. J., Hartmann, D., Kalberla, P. M. W., Mebold, U., & Pietz, J., 1999, A&A, 342, 213.

Kharchenko, V., Rigazio, Matt, Dalgarno, A., & Krasnopolsky, V. A., 2003, ApJL, 585, 1, 73.

Koutroumpa, D., Lallement, R., Kharchenko, V., Dalgarno, A., Pepino, R., Izmodenov, V., & Quémerais, E., 2006, A&A, 460, 289.

Koutroumpa, D., Acero, F., Lallement, R., Ballet, J., & Kharchenko, V., 2007, A&A, 475, 90.

Koyama, K. et al., 2007, PASJ, 59 SP1, S23.

Kuntz, K. D., Snowden, S. L., & Verter, F., 1997, ApJ, 484, 245.

Koutroumpa, D., Lallement, R., Raymond, J. C., & Kharchenko, V., 2009, ApJ, 696, 2, 1517.

Koutroumpa, D., Collier, M. R., Kuntz, K. D., Lallement, R., & Snowden, S. L., 2009, ApJ, 697, 2, 1214.

Kuntz, K. D., & Snowden, S. L., 2000, ApJ, 543, 1, 195.

Lallement, R., Bertaux, J. L., & Dalaudier, F., 1985, A&A, 150, 1, 21.

Lallement, R., Welsh, B. Y., Vergely, J. L., Crifo, F., & Sfeir, D. 2003, A&A, 411, 447.

Lallement, R., 2004, A&A, 418, 143.

Lallement, R., Raymond, J. C., Bertaux, J. –L., Quémerais, E., Ko, Y. –K., Uzzo, M. McMullin, D. Rucinski, D., 2004, A&A, 426, 867.

Lallement, R., Quemerais, E., Bertaux, J. L., Ferron, S., Koutroumpa, D., & Pellinen, R., 2005, Science, 307, 1447.

Lallement, R., Quemerais, E., Lamy, P., Bertaux, J. L., Ferron, S., & Schmidt, W., 2009, Proceedings of the SOHO–23 conference.

Leighton, R. B., 1964, ApJ, 140, 1547.

Lisse, C. M., Dennerl, K., Englhauser, J., Harden, M., Marshall, F. E., Mumma, M. J., Petre, R., Pye, J. P., Ricketts, M. J., Schmitt, J., Trumper, J., & West, R. G., 1996 Science, 274, 5285, 205.

Magnani, L., Chastain, R. J., Kim, H. C., Hartmann, D., Truong, A. T., & Thaddeus, P, 2003, ApJ, 586, 2, 1111.

Marshall, F. E., Boldt, E. A., Holt, S. S., Miller, R. B., Mushotzky, R. F., Rose, L. A., Rothschild, R. E., & Serlemitsos, P. J., 1980, ApJ235, 1, 4.

Mather, J. C, et. al., 1994, ApJ, 420, 2, 439.

Masui, K., Mitsuda, K., Yamasaki, N. Y., Takei, Y., Kimura, S., Yoshino, T., & McCammon, D., 2009, PASJ, 61 SP1, 115.

McCammon, D, & Sanders, W. T., 1990, ARA&A, 657.

McCammon, D. et al., 2002, ApJ, 576, 1, 188.

McComas, D. J., Ebert, R. W., Elliott, H. A., Goldstein, B. E., Gosling, J. T., Schwadron, N. A., & Skoug, R. M., 2008, Geophys. Res. Lett., 35, 18, L18103.

Miller, E. D. et al., 2008, PASJ, 60 SP1, S95.

Mitsuda, K. et al., 2007, PASJ, 59 SP1, S1.

Moretti, A., Campana, S., Lazzati, D., & Tagliaferri, G., 2003, ApJ, 588, 2, 696.

Morrison, R., McCammon, D, 1983, ApJ, 270, 119.

Mushotzky, R. F., Cowie, L. L., Barger, A. J., & Arnaud, K. A., 2000, Nature, 404, 6777, 459.

Østgaard, N., Mende, S. B., Frey, H. U., Gladstone, G. R., & Lauche, H., 2003, J. Geophys. Res., 108, A7, 18–1.

Pepino, R., Kharchenko, V., Dalgarno, A., & Lallement, R., 2004, ApJ, 617, 1347.

Ptak, A., & Griffiths, R., 2003, ASP Conf., 295, 465P.

Robertson, I. P., & Cravens, T. E., 2003, J. Geophys. Res., 108, A10, LIS 6.

Revnivtsev, M., Gilfanov, M., Jahoda, K., Sunyaev, R., 2005, A&A, 444, 381.

Sakai, K., Mitsuda, K., Yamasaki, Y. N., & Takei, Y., in prep..

Savage, B. D., & Lehner, N., 2006, ApJS, 162, 1, 134.

Serlemitsos, P. J., et al., 2007, PASJ, 59 SP1, S9.

Sfeir, D. M., Lallement, R., Crifo, F., & Welsh, B. Y., 1999, A&A, 346, 785.

Shelton, R. L., 2009, Space Sci. Rev., 143, 1, 231.

Shelton, R. L., Henley, D. B., & Dixon, W. V. 2010, ApJ, 722, 1, 302.

Shiota, D., Tsuneta, S., Shimojo, M., Sako, N., Suarez, D. O., & Ishikawa, R., 2012, PASJ, submitted.

Smith, R. K., et al., 2007, PASJ, 59 SP1, S141.

Snowden, S. L., Cox, D. P., McCammon, D., & Sanders, W. T., 1990, ApJ, 354, 211.

Snowden, S. L., Egger, R., Freyberg, M. J., McCammon, D., Plucinsky, P. P., Sanders, W. T., Schmitt, J. H. M. M., Truemper, J., & Voges, W., 1997, ApJ, 485, 125.

Snowden, S. L., & Freyberg, M. J., 1993, ApJ, 404, 403.

Snowden, S. L., McCammon, D., Burrows, D. N., & Mendenhall, J. A., 1994, ApJ, 424, 2, 714.

Snowden, S. L., Freyberg, M. J., Plucinsky, P. P., Schmitt, J. H. M. M., Truemper, J., Voges, W., Edgar, R. J., McCammon, D., & Sanders, W. T., 1995, ApJ, 454, 654.

Snowden, S. L., Collier, M. R., & Kuntz, K. D., 2004, ApJ, 610, 2, 1182.

Snowden, S. L., 2009, Space Sci. Rev., 143, 253.

Tawa, N. et al., 2008, PASJ, 60 SP1, S11.

Tsyganenko, N. A., & Sitnov, M. I. 2005, J. Geophys. Res., 110, A03208, doi:10.1029/2004JA010798.

Wargelin, B. J., Markevitch, M., Juda, M., Kharchenko, V., Edgar, R., & Dalgarno, A., 2004, ApJ, 607, 1, 596.

Yan, M. & Sadeghpour, H. R., & Dalgarno, A., 1998., ApJ, 496, 1044.

Yang, Y.; Mushotzky, R. F.; Steffen, A. T.; Barger, A. J. & Cowie, L. L., 2004, ApJ, 128, 4, 1501.

Yao, Y., Wang, Q. D., Hagihara, T., Mitsuda, K., McCammon, D., & Yamasaki, N. Y., 2009, ApJ, 690, 1, 143.

Yaqoob, T. et al., 2007, PASJ, 59 SP1, S283.

Yoshino, T., 2009, Ph.D. thesis, University of Tokyo.

Yoshino, T., Mitsuda, K., Yamasaki, Y. N., Takei, Y., Hagihara, T., Masui, K., Bauer, M., McCammon, D., Fujimoto, R., Wang, Q. D., & Yao, Y., 2009, PASJ, 61 805.

Yoshitake, H., Mitsuda, K., Yamasaki, Y. N., & Takei, Y, 2011, PASJ, submitted.

Wilms, J., Allen, A., & McCray, R., 2000, ApJ, 542, 2, 914.

A note on simulation improvements made on the submitted paper

The simulation for the distributions of neutral atoms in Heliosphere described in Appendix A had the following problems, and they were improved in a submitted paper, Yoshitake et al. 2013, PASJ, 65, 32 (arXiv:1301.5174):

1. The simulation time of Hydrogen was too short.

   For Helium the bulk velocity is dominant comparing to the thermal velocity due to its weight, and the simulation time of Helium distribution can be therefore estimated from the world size and the bulk velocity. Meanwhile, the bulk velocity and the thermal velocity of hydrogen is comparable, so the simulation time of Hydrogen distribution needs to be considerably longer than the case of Helium as the total velocity could be nearly zero. In the simulation carried out in the Ph.D. thesis, since the maximum simulation time of Hydrogen distribution was set to the value estimated from the Hydrogen bulk velocity, the simulation time was too short for most of hydrogen particles.

   In the simulation carried out in the submitted paper, we removed the maximum simulation time and continued particle-tracking calculations until particles leave the simulation world.

2. The initial condition of Hydrogen distribution was too simplistic.

   The simulation world was a rectangular parallelepiped of 200 AU $\times$ 300 AU $\times$ 300 AU in the thesis. Neutral particles were initially placed at a +x yz-plane and tracked toward the other end. For Helium the bulk velocity is dominant and the initial condition of the simulation is rather acceptable, however, for Hydrogen it is too simplistic as significant number of neutral particles may enter the simulation world from other surfaces.

   The new simulation applied a cylindric world and neutral particles were initially placed at every surface.

3. The simulation step was too large.

   In the simulation carried out in the thesis, the simulation step size was fixed and large. This resulted in an error of more than 100% in conservations of energy and angular momentum before and after the simulation for particles flying nearby the Sun.

   The new simulation applied a variable step size, allowing the error to be less than 1% even for particles passing within a hairbreadth of the Sun.

4. Low statistics.

   As the simulation world was quite large, an enormous number of particles have to be simulated to gain meaningful results. Billions of particles were tracked in the simulation carried out in the thesis, still the sufficient statistics could not be obtained.

   The neutral particle should distribute circularly-symmetric along an axis toward the flow direction across the Sun, so we applied a cylindric world with cylindrical coordinates and averaged distribution circumferentially in the new simulation. As a result, we obtained far-better statistics with the smaller number of particles.